# Thermographic PIV for Turbulent Flux Measurement

Dem Fachbereich Maschinenbau
an der Technischen Universität Darmstadt
zur
Erlangung des Grades eines Doktor-Ingenieurs (Dr.-Ing.)
genehmigte

Dissertation

vorgelegt von

**Hyunchang Lee, M.Sc.**

aus Kwangju, Korea

| | |
|---|---|
| Berichterstatter: | Prof. Dr. rer. nat. habil. A. Dreizler |
| Mitberichterstatter: | Prof. Dr. rer. nat. habil. B. Atakan |
| Tag der Einreichung: | 19.4.2016 |
| Tag der mündlichen Prüfung: | 15.6.2016 |

Darmstadt 2016

D17

# Acknowledgement

I look back the stay at RSM at TU Darmstadt during last four years and would like to mention a few names to appreciate their support.

First of all, I would like to thank Prof. Andreas Dreizler for accepting me in his institute and spending time for me and this project. He guided me not to be lost in the forest of my PhD project. I also would like to appreciate Prof. Burak Atakan for being the coreference of my dissertation and interesting discussion during my disputation.

Many colleagues at the institute helped me to adapt myself to the experimenter in the laboratory and life in Germany. Among them, I would like to thank Silvan, especially, who shared the office with me while discussing about each others project. Not only the scientific discussions, but also small talks regarding anything smoothed my work and life. I also would like to mention Michael who succeeded phosphor gas thermometry and developes it further and applies to other applications at RSM. I will remember the moment we spent together in the laboratory and the talk in the way home by bike at late nights after measurements. I want to thank Mr. Farouk Chourou, a bachelor student involved in this project. He performed the most of spectra measurement in this study and supported me till late nights during the measurement in jet-with-coflow configuration.

As the last, but the most, I would like to thank my family. First, I thank my son to be born in this world and grow healthy. My daughter, Naram could not speak a single word in the beginning of this project, but she encouraged me by showing me how to learn walking and speaking, whenever I was tired of developing this measurement technique. She is now grown to be a girl going to kindergarden, as the measurement technique has been developed. Lastly, I thank my wife, Hana, for being always present in my side and listening to whatever I told her and react somehow,... whether it is practicing the 'Monday' seminar talk (which should be extremely boring to her) or all little details happened in the institute. Without my family, indeed, I could not finish my dissertation. If I am allowed to receive applause for the work present here, I would turn this to these two.

Hyunchang Lee　　Chungju, Korea, den July 16, 2016

to Naram

# Contents

# List of Tables

# List of Figures

# Nomenclature

## Uppercase Latin letters

| | |
|---|---|
| $E$ | Energy |
| $F_L$ | Laser fluence |
| $I_A$ | Signal in blue channel |
| $I_B$ | Signal in red channel |
| $K$ | Camera conversion factor counts/electron |
| $L_2$ | Lateral integral length scale |
| $N_{cam}$ | Camera readout error |
| $N_{ker}$ | Kernel size of spatial filter |
| $R$ | jet radius, d/2 |
| $R_sd$ | Seeding density ratio of jet and co-flow |
| $R_{uu,2}$ | Lateral two point spatial correlation of axial velocity |
| $T$ | Temperature |
| $U$ | Axial velocity |
| $V$ | Radial velocity |

## Lowercase Latin letters

| | |
|---|---|
| $d$ | jet diameter, 16 $mm$ |
| $f\#$ | f number |
| $f$ | focal length |
| $m$ | magnification |
| $r_{\frac{1}{2},\theta}$ | Jet half width based on mean scalar |
| $r_{\frac{1}{2}}$ | Jet half width based on mean axial velocity |
| $t$ | time |
| $u$ | axial velocity perturbation, $u = U - \langle U \rangle$ |
| $v$ | radial velocity perturbation, $v = V - \langle V \rangle$ |

## Uppercase Greek letters

| | |
|---|---|
| $\Gamma$ | Spectra of a phosphor |
| $\Sigma$ | Intensity of phosphorescence in blue or red channel |
| $\Theta$ | Normalized temperature, passive scalar in this study |

## Lowercase Greek letters

| | |
|---|---|
| $\alpha$ | Absorption coefficient |
| $\alpha$ | Heat diffusivity |
| $\alpha_t$ | Turbulent heat diffusity |
| $\eta_q$ | quantum efficiency of a phosphor |
| $\lambda$ | Wavelength |

| | |
|---|---|
| $\nu$ | Kinematic viscosity |
| $\nu_t$ | Turbulent viscosity |
| $\nu_{freq}$ | Frequency |
| $\sigma_A$ | Absorption cross-section |
| $\sigma$ | Standard deviation |
| $\tau$ | luminescence lifetime |
| $\tau_D$ | Dynamic relaxation time |
| $\tau_T$ | Thermal relaxation time T |
| $\theta$ | Scalar perturbation, $\theta = \Theta - \langle\Theta\rangle$ |
| $\xi$ | Transmittance of a filter |

## Operator

| | |
|---|---|
| $()'$ | $\langle()^2\rangle^{1/2}$, standard deviation or root mean square |
| $\langle()\rangle$ | Ensemble average |

## Dimensionless numbers

| | |
|---|---|
| $Bi$ | Biot number |
| $Pr_t$ | Turbulent Prandtl number |
| $Re$ | Reynolds number |

## Abbreviations

| | |
|---|---|
| $DNS$ | Direct Numerical Simulation |
| $FWHM$ | Full Width at Half Maximum |
| $HCCI$ | Homogeneous Charge Compression Ignition |
| $HWA$ | How Wire Anemometry |
| $IF$ | Interference Filter |
| $LDV$ | Laser Doppler Velocimetry |
| $LED$ | Light Emitting Diode |
| $LIF$ | Laser Induced Fluorescence |
| $PIV$ | Particle Image Velocimetry |
| $rms$ | Root mean square |
| $SLIPI$ | Structured Laser Illumination Planar Imaging |
| $TGP$ | Thermographic Phosphor |
| $UV$ | Ultraviolet |
| $YAG$ | Yttrium Aluminium Garnet |

# Chapter 1.

# Introduction

## 1.1. Motivation

**Turbulent flows** The flows encountered in most of the engineering systems, which facilitate our society, are turbulent, and the role of turbulence in the system is undoubtedly important. The thrust of a propeller of a ship or helicopter is dramatically improved by turbulence. Heat transfer including a flow, e.g., cooling or heating a system, would be inefficient without turbulence. Enhanced mixing by turbulence makes combustion systems, such as internal combustion engine, gas turbine combustor, or aircraft engine possible to be compactly designed. The level of mixedness, which is a very important factor in chemical yielding, is mainly controlled by turbulence. Therefore, understanding the turbulent flows and predicting their effects has been a very important subject for the last century.

Turbulent flows, however, are *unpredictable*: although the motion of the flow is governed by the Navier-Stokes equations, all details in a time and a position can not be determined exactly. For example, when one measures the velocity of a flow in a point, the measurement in a certain time duration does not assure to predict a velocity after a short instance. In the flow, inevitable small perturbations always exist e.g., an inhomogeneous smoothness of the surface in the boundary condition. The turbulent flow is very sensitive to these small perturbations because the nonlinear term in the Navier-Stokes equations can enormously amplify the small perturbations at high $Re$. This amplifying power of the Navier-Stokes equations is believed to cause turbulent flows to be unpredictable [7].

Although the instantaneous variables of the turbulent flow can not be determined, their statistical properties such as mean, variance, probability density function, or correlation between the variables, are predictable. Therefore, the instantaneous variables are decomposed to the mean and the fluctuation and substituted by them in the governing equations. The resulting mean momentum and scalar conservation equations include the Reynolds stress and the scalar flux, respectively. The terms represent the transport of momentum and scalar by turbulence. In the set of given equations, the number of unknowns is larger than the number of equations, thus, the Reynolds stress and the scalar flux should be closed by a suitable model. Various approaches have been attempted to model the terms. Closing the terms of the turbulent transport with a model means predicting the turbulent flows statistically, and the accuracy of the model determines the accuracy of the prediction. The model plays a central role in predicting the turbulent flow.

Another characteristic of the turbulent flow is *diffusivity*. One can use a knife to take and spread honey on a bread easily, but not water for their different viscosities; the large viscosity of honey makes it fall down slowly from the knife. The diffusivity of turbulence, however, is not a property of the fluid, but the flow. When a flow transits from laminar to turbulence at certain *Re* (this *Re* of transition differs one flow to another. For example, 2300 for the pipe), various scales exist in turbulence. Large eddies are responsible for engulfing surrounding fluid in the turbulent flow, the large structures break into intermediate sizes and the eddies in these sizes increase the interfacial surface. In the end, the eddies in even smaller size are dissipated by molecular diffusion [22]. This process of breakdown is so vigorous that the turbulent flow can diffuse momentum or scalar far more rapid than molecular diffusion alone can do. The enhanced diffusion of momentum and scalar appears as Reynolds stress and scalar flux, and the enhanced transport should be included adequately in the terms.

**Measurement of scalar flux** A reliable experiment is highly demanded for modelling the term appropriately, and especially for modelling the scalar flux, a simultaneous measurement of the velocity and the scalar is needed. For this purpose, a volume of experiments have been performed in simple configurations e.g., pipe, jet, homogeneous mixing layers. Relying on the experimental observations, the underlying physics of the turbulent transport has been conjectured for a model to be established. Furthermore, to evaluate the model when applied in more complex and practical cases, experimentally well-measured data in the condition are again needed to be compared with the model. Therefore, a reliable technique for measuring the velocity and the scalar simultaneously in a specific system is highly needed.

From the last few decades, laser diagnostics started to be applied to scalar flux measurements in turbulent flows. In contrast with measurement techniques using a probe, such as thermocouples, hot and cold wires, laser diagnostics is not invasive or semi-invasive that the phenomena are believed not to be affected or less affected by the measurement technique itself. Additionally, laser diagnostics has high spatial and temporal resolutions, thus, are expected to make the details of the turbulent flows to be observed. The PIV and LDV using seeded particles have been widely applied for measuring velocity fields. The LIF using naturally occurred or intentionally seeded tracers were used together with PIV or LDV for scalar flux measurements. The examples of some studies having used different laser diagnostics to measure scalar flux will be introduced soon.

The phosphor thermometry, one of the laser diagnostics, uses the dependence of phosphorescence on temperature following UV excitation, such as lifetime, or change of the spectrum. The technique has been successfully applied to the surface temperature measurement for the last half century and extended its application first to the droplet and the spray measurements. Shortly after that, an idea of using the same tracer particles for measuring velocity and temperature, which is also called *thermographic PIV*, has been proposed and developed for about last ten years[2, 29, 65]. The PIV is a well-established and robust technique to measure velocity fields, which needs tracer particles. By using micrometer-sized phosphor particles as PIV tracers, the same particle can serve for velocimetry and thermometry at the same time. This can make the experimental setup simpler compared to LIF, which needs additional seeding appliances used with PIV. As PIV assumes the same velocity between the flow and particles, the similar assumption could be applied to the temperature. In addition, the phosphor materials are generally made of ceramic and expected to stand the flame temperature. The application of the technique to two-dimensional gas temperature measurements, preferably also in combustion environment, was tempting.

## 1.2. State of art measurements

**Laser diagnostics** Sakakibara et al. [77] investigated the role of the counter-rotating vortex in heat transfer enhancement of an impinging plane water jet to a heated wall. The velocity and temperature were measured by PIV and LIF with a dye, Rhodamin B. The measured scalar flux (here, turbulent heat flux) amounted to about 20 % of the total heat transfer from the wall. Additionally, through weighted PDF of the scalar flux, they showed that the heat transfer by hot water from the wall to the fluid contributed more than by cold water from the fluid to the wall. To show the relation between the counter-rotating vortex and the scalar flux, they investigated closely the correlation between them and concluded that the turbulent heat transport generated by counter-rotating vortex account for around 40% of total turbulent heat transport.

Most et al. [61] demonstrated the feasibility of simultaneous filtered Rayleigh scattering thermometry and PIV in premixed flame. The signal of Rayleigh scattering depends on number density of scattering molecules and the Rayleigh scattering cross section of gas mixture. Therefore, if the local species concentration is known or could be assumed somehow, the temperature is deduced from the measured number density based on the ideal gas law. The seeded particles for PIV, however, emit strong Mie-scattering and prevent the measurement of Rayleigh scattering. In the filtered Rayleigh scattering, the strong Mie-scattering is blocked by a narrow atomic or a molecular filter, while the broadened Rayleigh scattering can be measured. In [61], they studied the interaction of turbulence and flame by comparing the results from wire stabilized flame and bluff body stabilized flame. The measured scalar flux showed gradient or counter gradient diffusion according to its configuration.

Nauert & Dreizler [63] applied the simultaneous OH-LIF and LDV in a swirl flame to understand the interaction of turbulence and flame. In modelling the scalar flux in the flame, gradient diffusion occurs when the effect of turbulence prevails while counter-gradient diffusion occurs when the effect of flame dominates. They used OH-LIF image to distinguish the burned and unburned regions and could obtain the conditioned velocities from the velocities measured by LDV. In addition, the mean progress variable could be acquired by averaging the OH-LIF image. By using conditioned velocities and mean progress variables as the last step, the scalar fluxes in different axial positions were attained and gradient and counter-gradient diffusion were examined. In some downstream position, counter-gradient diffusion occurred only in the axial flux and the other were gradient diffusion.

**Thermographic phosphor** The first application, to the author's knowledge, is a study on the structure of a flame kernel in ignition of HCCI engine by Hasegawa et al. [35, 36]. They measured instantaneous two-dimensional temperature fields by using 1.8 $\mu m$ sized YAG:Dy particles with the two-color ratio method to temperatures upto 1100 $K$. The size of the flame kernel based on the instantaneous temperature fields could be measured.

However, subsequent studies [44, 52] reported weak signal intensity, and in [52], even with greater particle size (10.2 $\mu m$), meaningful single shot measurement was not able to be obtained in a temperature range of 850 $K$. Considering experimental difficulties in a confined environment such as background from deposited particles at wall, the successful result of [35, 36] leaves some questions. After that, Omrane et al. [65] performed a feasibility study by using MFG:Mn particles as a tracer. The intensity of the phosphor was unfortunately not strong enough, and only the averaged temperature field around 750 $K$ was obtained. Rothamer & Jordan [75] obtained single-shot temperature fields with upconversion phosphor YAG:Yb,Er to 480 $K$, however, the particle size was around 8 $\mu m$, which is rather large to assume reasonable traceability of the particles to the gas phase. Fond et al. [29] demonstrated the velocity and temperature, simultaneously and instantaneously by using 2 $\mu m$ sized BAM particles with a detailed explanation of the thermometry setup. In the following year, a couple of successful studies have been reported. Jordan & Rothamer used the YAG:Pr and measured temperature to 750 $K$ with comparable performance with BAM. Lawrence et al. [52] studied the spectra of YAG:Dy and BAM particles and demonstrated the instantaneous temperature field to 850 $K$ with BAM. Van Lipzig et al. [88] applied the BAM particles to the temperature measurement in the high-pressure cell. They seeded the particles with the fuel while pressurizing the cell (gas density 10,15 and 20 [$kg/m^3$]) and measured the temperature field after the combustion. They could measure temperature fields only to about 650 $K$ because the signal at high temperature was too weak to be measured. Abram et al. [2] demonstrated 3 kHz measurement of velocity and temperature with BAM in the wake of heated cylinder. They took an advantage of the high quantum efficiency of BAM and could obtain enough signal to measure the temperature with low pulse energy (1.3 mJ) of a high-speed laser. Jovicic et al. [45] compared the YAG:Dy and the YAG:DyEr applied to the gas temperature measurement. Although they showed improved measurement with 'tuned' phosphor YAG:DyEr, the overall performance appeared worse compared with other studies.

At the same time when the general concept was being realized, specific issues in the phosphor thermometry has been investigated. First the effect of laser fluence has been dealt with. In the feasibility test by using MFG:Mn [65], relatively weak signal from dilute particle number density compared to the surface application was acknowledged, which result in the failure in acquiring a single-shot temperature field. Increasing the laser fluence was a possible solution without considerable effort. Accordingly, to investigate a potential laser heating effect with increased excitation, Linden et al. [54] adjusted the laser fluence from 0.08 to 1.5 $J/cm^2$ and compared the spectra of the phosphorescence from aerosolized BAM particles in the room temperature. They concluded an independence of BAM spectra on the laser fluence. The independence were confirmed by [29, 52] later, but this issue in BAM were revisited by the same author in [29], and the dependence of intensity ratio on the laser fluence in room temperature was demonstrated [28]. The similar trend in ZnO has been found by [1] and they proposed to use a flat field image, which was averaged intensity ratio image at room temperature, to compensate this effect. In addition to the relation between the laser fluence and the intensity ratio, as a slight different point of view, the relation between the laser fluence and the intensity, or the luminescence saturation[1]

---

[1] nonlinearity of the emission intensity with increasing excitation

of BAM, was studied in [28]. Their aim was to extend the luminescence saturation range by understanding the phenomenon. Among three possible mechanisms of luminescence saturation, they presumed the depletion of Eu ion in the ground state as the reason of the luminescence saturation. They attempted to increase the emission intensity by applying different excitation wavelength(266, 355$nm$), and bandwidths (1, 200 $cm^{-1}$), but unfortunately obtained little increase.

The effect of seeding density on the measurement technique has been also addressed. Van Lipzig et al. [88] pointed out the multiple scattering effect in dense seeding density; they observed phosphorescence signal in the outside of excitation and attributed this to scattering of the excitation. They warned that the dense seeding causes thickening of the laser sheet and also worsening of the spatial resolution. Fond et al. [27, 28] investigated the effect of seeding density on the intensity ratio. They observed slightly decreasing intensity ratio with increasing seeding density. The preferential absorption of BAM was proposed, but for the uncertainty in the camera linearity, they could not conclude the exact reason for this.

In the same studies [27, 28], the effect of surrounding gas on the intensity ratio were examined, and the relation between the intensity ratio and temperature was similar in the nitrogen and the air ambient. The survivability of phosphor particles in a flame, which was one of the issues in applying the technique to the combustion environment, was investigated by Yu et al. [96]. They seeded the YAG:Dy (melting point 2213 $\pm 7$ $K$) particles to a lean methane-air premixed flame (calculated adiabatic temperature, 2000 $K$) and collected the particles after the flame by an impactor. By measuring the spectra of collected particles in an oven to 1300 $K$ and calculating the intensity ratio, they argued that the characteristic of the phosphorescence of YAG:Dy was not changed after experiencing the flame. The survivability of BAM has been indirectly demonstrated in [88] by measuring the temperature after the combustion.

Not only the simple flows, but the measurement technique has been also applied to more technically relevant system such as an engine [64, 85]. However, those results are still close to the feasibility studies. The lifetime method has been also applied to the gas temperature measurement by Someya et al. [81–83] to simplify the experimental setup. However, the precision and the accuracy were worse than the intensity ratio method. While the intensity ratio method typically needs a beam splitter and two detectors, the lifetime method needs one high-speed camera.

## 1.3. Aim and scope of this study

The aim of this study is to develop the thermographic PIV further and validate the technique by performing measurements in a canonical configuration. For this purpose, the subsequent chapters will be comprised as following.

Chapter 2 deals with the fundamental theory of phosphorescence and its dependence on temperature. The basic theory of imaging particles will be additionally explained. In Chapter 3, the experimental setups, which were required to measure spectra of various phosphors and the scalar flux, will be introduced. The procedure of measuring spectra in the oven and its data reduction are explained, and the same for scalar flux measurement is presented. In addition, the filter optimization process for thermometry will be explained together.

Investigation of various phosphors are summarized in Chapter 4. The phosphor thermometry needs new phosphors in various temperature ranges of potential applications, such as natural convection, forced convection, and combustion. Especially, weak phosphorescence in high temperature for thermal quenching hinders the application of the technique to flames, which were the original aim of the phosphor gas thermometry. Only a few phosphors have been applied to the gas thermometry ($Y_2O_3S$:Er,Yb [75], BAM [2, 27–29, 52, 78, 85, 88], YAG:Pr [44, 64], YAG:Dy [35, 36, 45, 52, 96], YAG:Dy,Er [45], $Y_2O_3$:Eu [95] and ZnO[1]), and as explained, the maximum temperature measurement with a meaningful precision at the moment is limited to 850 $K$ in the free jet measurement by BAM [52]. It is evident that more phosphor candidates from the vast inventory should be evaluated and characterized according to the criteria for the gas thermometry. To find promising phosphors in various temperature ranges, a methodology of investigating and evaluating phosphors by using spectra in an oven was developed in this study. Eight phosphors from the list of the thermographic phosphors and the lamp phosphors were tested according to the methodology and the results will be presented in Chapter 4.

Based on the previous investigations on potential errors, sources of uncertainty will be analysed systematically in Chapter 5. Although the effects, such as, multiple scattering and preferential absorption, have been mentioned as potential errors or factors deteriorating the measurement technique, their effects are still ambiguous. Furthermore, the effect of seeding density will be more severe in a large volume of particles, which one will definitely confront in technically more relevant systems, such as automobile engines, gas turbine combustors. Therefore, the issue of laser heating effect, multiple scattering effect, and preferential absorption will be investigated and the results will be presented.

In Chapter 6 *the scalar flux measurement* by using thermographic PIV will be presented. Although the previous reports on the temperature measurement by phosphor particles showed comparable precision and accuracy to other planar thermometry, e.g., LIF, the scalar flux measurement has not been reported yet. Therefore, the scalar flux measurement will be demonstrated in the near- and transition field of heated round jet, where one can take advantage of the large temperature gradient. Comparison with the widely accepted previous results will be followed for the validation of the measurement technique.

The dissertation will be closed with conclusion and outlook in Chapter 7. The most important conclusions of this study will be summarized, and required future work will be proposed. Additionally, preliminary results of a jet in crossflow configuration, attempted in this study, but not finished, will also be briefly presented.

# Chapter 2.

# Theoretical background: principle of phosphor gas thermometry

In this chapter, theories on which this study stands will be introduced. A general phosphorescence procedure, which includes absorption, radiative and non-radiative emission, will be described after providing some concepts required to understand the procedure. After that, the major two characteristics of phosphorescence depending on temperature, which are change of lifetime and spectrum, will be presented. Especially, the changing spectrum will be dealt in more detail with examples because the phosphor gas thermometry used this characteristic. In the end, the way on how the phosphorescence from a particle is imaged will be depicted.

## 2.1. Phosphorescence and its use as thermometry

**Thermomgraphic phosphor** The term, phosphor originates in the Greek word, phosphorous which means 'light bearer'. It was used for the first time in 1602 by Vincenzo Cascariolo to describe the material emitting purple-blue light at night that is also known as 'Bolognian Stone' [19]. Similar materials synthesized in Europe after this discovery of light-emitting stone have been called phosphor [94]. Phosphors are synthesized by adding a small amount (doping) of a transition metal or a rare earth intentionally to a ceramic host. These materials have been extensively applied in the display and lamp industries during the last century. The degradation of the luminescence in high temperatures caused the characterisation of the thermal behaviour of this material to optimize its industrial use. On the other hand, exploiting this behaviour as thermometry has been followed [4]. Phosphor thermometry has been applied to the surface temperature measurement and expanded its application enormously during the last decades. Phosphor surface thermometry is reported to measure the temperature range from slightly above absolute zero to 1970 K [16]. Recently, the technique has expanded its application to gas temperature measurement.

### 2.1.1. Phosphorescence

**Basic concepts to understand phosphorescence** Concepts of the energy level of the free activator ion and interaction between activator and the lattice are the basis to understanding the phosphorescence procedure. A concept of energy level based on quantum mechanics is given here, and the interaction between the activator and the lattice will be explained with the help of configurational coordinate model.

**Specification of orbitals and term symbols** The wave-like behaviour of an electron in an atom could be expressed mathematically as orbital. Each orbital is specified with the following quantum numbers in table 2.1 and the readers are referred to [6] for a detailed description.

**Table 2.1.:** Quantum numbers explaining electronic energy level

| *Notation* | *Name* | *Expression* | *Meaning* |
|---|---|---|---|
| $n$ | principal | $1, 2, 3, \ldots$<br>or $K, L, M, N, \ldots$ | Occupying electron shell<br>a different energy level |
| $l$ | angular momentum | $0, 1, 2, 3, \ldots, (n-1)$<br>or $s, p, d, f, g, h, \ldots$ | the occupying subshell |
| $m_l$ | magnetic | -$l$, -($l$-1),. . . ,($l$-1),$l$ | the particular orbitals in a subshell(direction of orbital) |
| $m_s$ | spin projection | 1/2 or -1/2 | the spin of the electron |

The electrons occupy the orbitals specified by aforementioned quantum numbers in the order of increasing energy level dictated by the construction principle. The state of the occupied orbitals in certain atoms or ions is called configuration. In a particular configuration, when there is more than one electron, the interactions between electrons rise and split the energy level. The term symbols, $^{2S+1}L_J$ can describe the energy level of an atom in given configurations succinctly. All the electronic transitions could be expressed as a transition between states represented by term symbols. An explanation on angular momentum quantum numbers comprising term symbols is found in table 2.2.

**Table 2.2.:** Angular momentum quantum numbers comprising term symbols

| *Notation* | *Name* | *Expression* | *Meaning* |
|---|---|---|---|
| $L$ | total orbital | $0, 1, 2, 3, \ldots$or $S, P, D, F, \ldots$<br>$L = l_1 + l_2, l_1 + l_2 - 1, \ldots, \lvert l_1 - l_2 \rvert$ | coupling the angular momenta of orbitals that the electrons occupy |
| $S$ | total spin | $S = s_1 + s_2, s_1 + s_2 - 1, \ldots, \lvert s_1 - s_2 \rvert$ | coupling individual spin number of electrons |
| $J$ | total | $L + S$ | interaction between the electron and the orbital |

**Configurational coordinate model** The interaction between the activator and the lattice is represented with a configurational coordinate model [11].

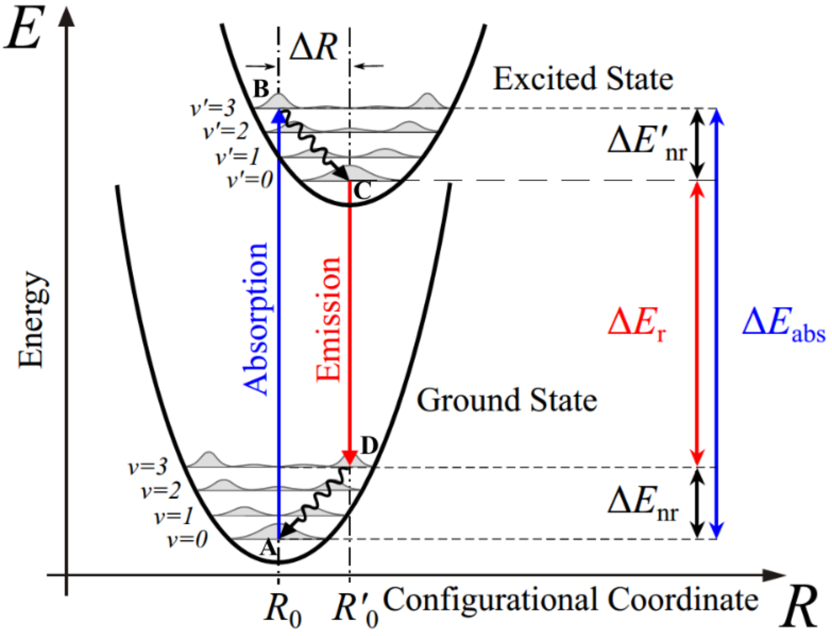

**Figure 2.1.:** configurational coordinate model reproduced from [50]

The configurational coordinate model expresses the potential energy of the ion as a function of the distance between activator and the ligand of the lattice. This model is based on the so-called symmetric stretching (breathing), which assumes that surrounding ligands vibrate around the activator in phase. After considering harmonic vibration, the energy could be expressed in the second order polynomial of the displacement as below. $E = \frac{1}{2}k(R - R_0)^2$ where $k$ is the force constant and $R$ is the distance between ion and ligand. the Schrödinger equation for the above equation represents quantized vibrational states. $E_v = (v + \frac{1}{2})h\nu_{freq}$ where $v$=0,1,2, . . . and $\nu_{freq}$ is the frequency of the oscillator. These energy levels appear as parallel lines in figure 2.1. The wave equations for individual vibrational states are also known. It is important to bear in mind that when $v = 0$, the electrons are likely to be found in equilibrium distance $R_0$, whereas $v > 0$, in the edge of the parabola as also shown in figure 2.1. Similarly with ground state, the excited state is represented as a parabola with force constant $k'$ and equilibrium distance, $R_0'$. When the electronic transition occurs among shielded orbitals by filled outer shell (e.g., $4f^n$ in the rare earth), the electronic transition is not coupled with vibration of centre and $\Delta R$ has small value. In contrast, when the transition happens in the outer shell (e.g., $4f^n \rightarrow 5d$ in the rare earth), it is more strongly coupled with lattice vibration and has a large value of $\Delta R$.

**Phosphorescence process** Phosphorescence is a kind of luminescence that is described as emitting radiation after absorbing energy. Luminescence includes both fluorescence and phosphorescence. Usually in inorganic materials, emission during excitation is called fluorescence, and persisting light after cessation of excitation is called phosphorescence [94]. While fluorescence arises from allowed transition, phosphorescence arises from forbidden transition. Two selection-rules that allow and prohibit a transition exist; spin-selection and parity-selection rule. The latter prohibits the transition between the same subshells, e.g., $(4f \rightarrow 4f)$ in trivalent rare earth ions. The former prohibits the transitions between different multiplicities, e.g. (triplet → singlet) states. When the spins of all electrons are paired, the state is singlet and parallel, triplet. The rate of forbidden transition is relatively slow. For example, the emission in BAM:Eu is spin forbidden, but parity allowed and the lifetime at room temperature is order of $\mu s$. As contrast, the emission in YAG:Dy is both spin and parity forbidden, thus the lifetime is order of ms.

**Absorption** In the ground state, electrons are likely to be found in the equilibrium distance, $R_0$(point $A$ in figure 2.1). After absorbing external energy, the electrons are promoted to the excited state. Here the transition is believed to arise vertically($A \rightarrow B$) according to the Franck-Condon principle. It states classically that the nuclei is much heavier than the electron so that it is not able to respond to the electronic transition. Therefore, electronic transitions (absorption and emission) proceed in constant displacement. Meanwhile, quantum mechanically, it means the greater the transition intensity between two electronic-vibrational states, the more significant the overlap of the wave function of each state.

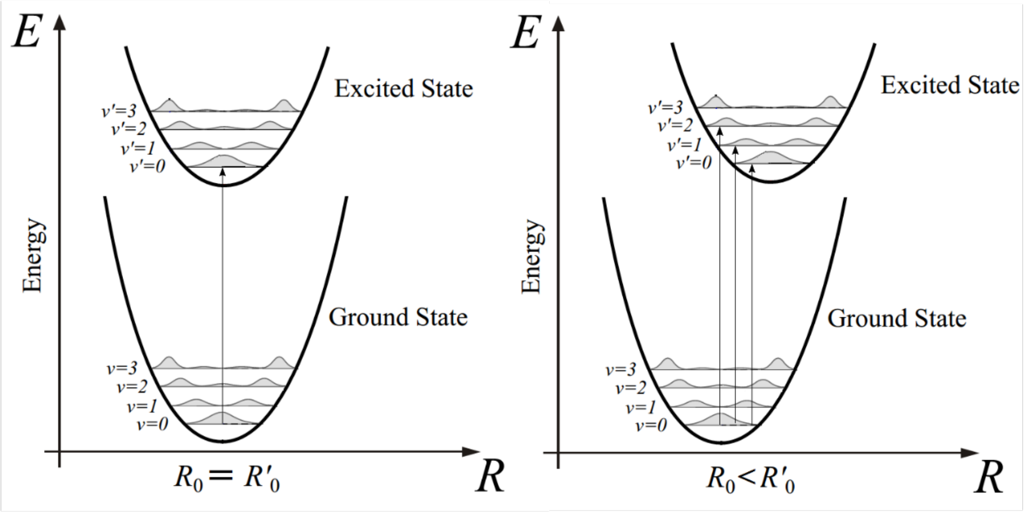

**Figure 2.2.:** Broadening of absorption spectra according to different $\Delta R$. When $\Delta R = 0$ (left), the most of electronic transitions occur between $v = 0$ and $v' = 0$ states and the absorption spectra is narrow. However, when $\Delta R > 0$ (right), the transition can happen to $v' > 0$ from $v = 0$ state and the absorption spectra widen. Reproduced from [50]

.

The larger $\Delta R$, the broader absorption spectra become. When $\Delta R$ is small, most of the transition occur between $v = 0$ and $v' = 0$ states, as shown on the left of figure 2.2. On the contrary, when $\Delta R$ is large, the transitions to other $v' > 0$ states are possible and bring the broadening of spectra. Not only large $\Delta R$ but also high temperature produce the broadening of spectra by pumping electrons to $v > 0$ and $v' > 0$ states. These broadening mechanisms apply in the same way to the emission.

**Emission** After absorption, the electrons cascade to $v' = 0$ state ($B \rightarrow C$ in figure 2.1) releasing the energy to the surroundings without radiative emission because the vibrational rate is much faster than the emission rate [11]. This process is called relaxation. Subsequently, the electrons move from the excited state to the ground state according to the Franck-Condon principle and emit photons corresponding to energy differences between two states($C \rightarrow D$ in figure 2.1). This procedure is emission. Again the relaxation from $v > 0$ state to $v = 0$ state($D \rightarrow A$ in figure 2.1) takes place and the energy difference is absorbed by the surrounding lattice. Therefore, absorbed energy is greater than emitted energy, and this difference is called Stokes shift.

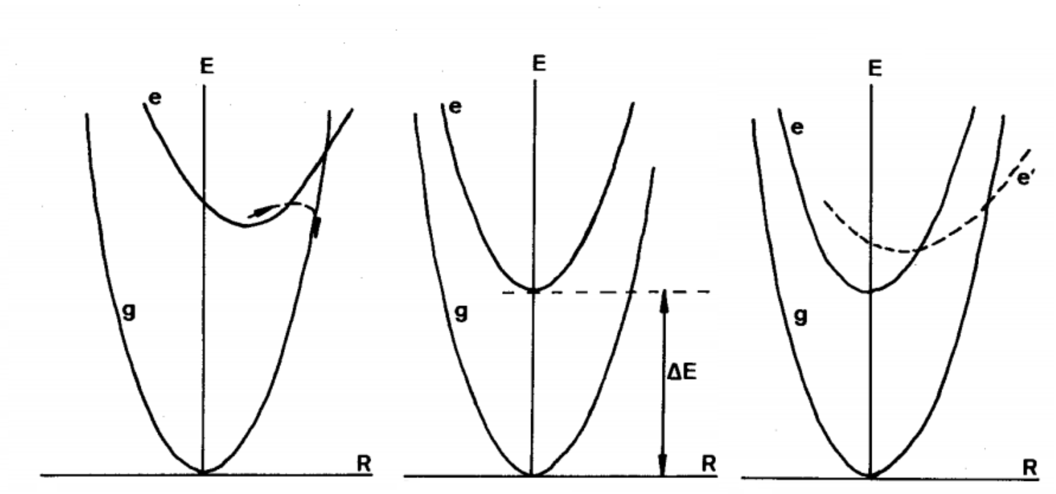

**Figure 2.3.:** Illustration of different ways of non-radiative emission. The g denotes ground state, and e denotes excited state. Each figure explains (left) thermal quenching (middle) multi-phonon emission (right) feeding e state by e' state. Reused from [11]

**Non-radiative emission** The emission is not inevitable in the return from the excited state to the ground state. Three different ways of non-radiative emissions are illustrated in figure 2.3 as examples.

First, the left of figure 2.3 represents the thermal quenching of luminescence. The ground and excited states can intersect, when $\Delta R$ is large. If the wave function of $v' = 0$ state and nearby $v >> 1$ state overlap each other substantially, the transition can take place without radiative emission. Remember that when $v = 0$ or $v' = 0$, the electrons are likely to be in the centre, whereas when $v > 0$ or $v' > 0$, they are likely to be on the edge of the parabola. Therefore, the larger $\Delta R$, the more overlap between ground and excited state and the thermal quenching is more likely to happen. At higher temperatures, the electrons are more likely to be relaxed in the higher vibrational state ($v' > 0$) and have more chance to overlap with the higher vibrational state ($v >> 1$) of ground state and non-radiative emission rate increases in higher temperatures. All optically absorbed energy is transformed in heat by the lattice.

Second, when $\Delta R$ is small, there is less chance for thermal quenching to occur as seen in the middle of figure 2.3. Here, when $\Delta E$ is the same with or less than 4 or 5 times the highest vibrational frequency of surroundings, the transition can happen without radiation. This procedure is called multi-phonon emission. Both thermal quenching and multi-phonon emission are highly temperature sensitive.

Lastly, there are two excited states, $e$ and $e'$, where forbidden and allowed transition from ground state $g$ occur respectively. Here, the transition to allowed $e'$ state feeds the forbidden $e$ state non-radiatively, and the emission occurs from the $e$ state. This process is represented in the right of figure 2.3.

### 2.1.2. Different approaches for using phosphorescence as thermometry

Phosphorescence is temperature-dependent in several ways, as explained in a couple of review papers [3, 4, 16]. Only the lifetime method and the intensity ratio method among them will be introduced, since these two methods have been exploited most frequently. After that, the reason for which the intensity ratio method is preferred to the lifetime method in gas temperature measurement will be given.

**Luminescence lifetime method** The decay of luminescence intensity $I(t)$ may be assumed to be the mono-exponential function of elapsed time after cessation of excitation $t = 0$.

$$I(t) = I_0\, exp(-t/\tau)$$

Where $I_0$ is the luminescence intensity when $t = 0$ and $\tau$ is the lifetime when the luminescence intensity reduces to $I_0/e$. After denoting number of excited activators in a volume by $n^*$, the rate equation for $n^*$ is,

$$\frac{dn^*}{dt} = (W_r + W_{nr})n^*$$

Here $W_r$ is the radiative emission rate, and $W_{nr}$ is non-radiative emission one. The solution of the equation above is

$$n^*(t) = n_0^*\, exp[-(W_r + W_{nr})t]$$

Because luminescence intensity is proportional to $n^*$,

$$\tau = 1/(W_r + W_{nr})$$

Here the non-radiative emission rate $W_{nr}$ depends on the temperature, and so does the lifetime $\tau$.

**Luminescence intensity ratio method** According to [34], phosphorescence spectra can be affected by temperature in several mechanisms. First, with increasing temperature, the crystal field fluctuates more from enhanced lattice vibration and brings widening of spectra. Second, the distance between activators and lattice ligands may elongate in thermal expansion. This expansion causes the crystal field to be weakened and the emission frequency to be shifted. Third, the non-radiative relaxation rate increases with increasing temperature and quenches the upper state first. Fourth, however, populating the upper state at high temperature is also possible, since the upper states are more populated in high temperature according to the Boltzmann distribution. These mechanisms will be explained with selected examples from phosphors used for surface temperature measurement with intensity ratio method (e.g. phosphors summarized in Table 5 of [16]).

**Line-emission phosphors** To explain the variation of spectra in line-emission phosphors, two conflicting mechanisms, identified as third and fourth in previous section, should be introduced in the context of distance between the energy levels. Let there be closely distributed energy levels over the large energy gap that is likely to be overcome only by radiative emission. In the case of a relatively large energy gap ( $\sim 4000\ cm^{-1}$), thermal pumping is difficult to happen, but the multi-phonon emission and cross over relaxation are not. Therefore, emissions from the higher energy state are quenched first. In the case of a small energy gap ($\sim 1000\ cm^{-1}$), by contrast, the upper state could be more populated at higher temperatures by thermal pumping.

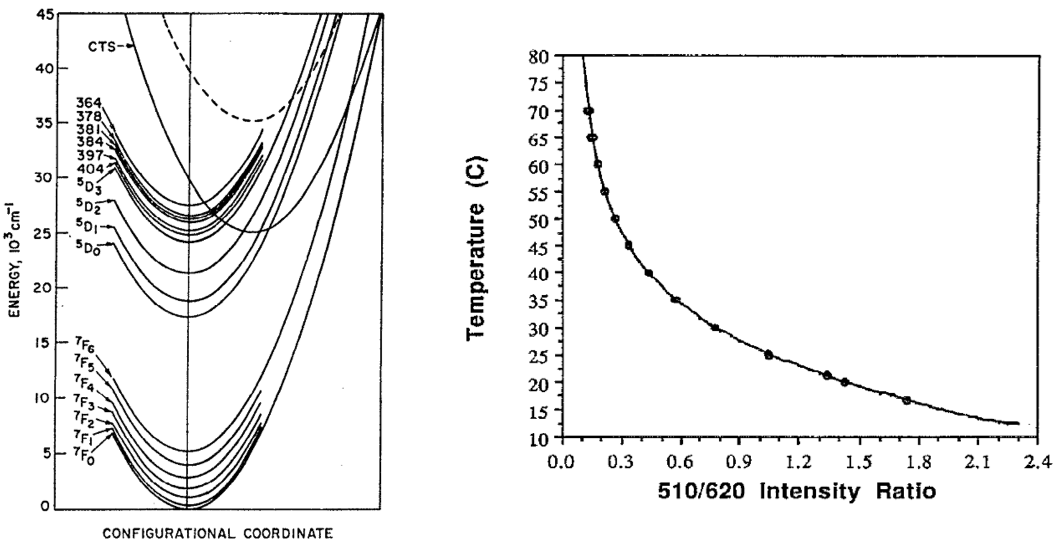

**Figure 2.4.:** Left: Configurational diagram of $La_2O_2S : Eu^{3+}$, Right: Intensity ratio-temperature of $La_2O_2S : Eu^{3+}$. Reused from [10].

A useful example of the first mechanism is $La_2O_2S : Eu^{3+}$. According to [10], the gaps of energy levels $^5D_J$ in $La_2O_2S : Eu^{3+}$ are quite large to be populated with thermal pumping. As a result, non-radiative emission prevails, and emissions from upper states are quenched first with increasing temperature. Therefore, the intensity ratio of shorter wave length to longer one decreases with temperature as shown in figure 2.4. The thermal quenching in $La_2O_2S : Eu^{3+}$ stems from two-step charge transfer state (CTS) energy transfer process, whereas the multi-phonon emission is common in other phosphors [10].

As examples to explain the other mechanism, there are $Dy^{3+}$ and $Sm^{3+}$ [34][24].

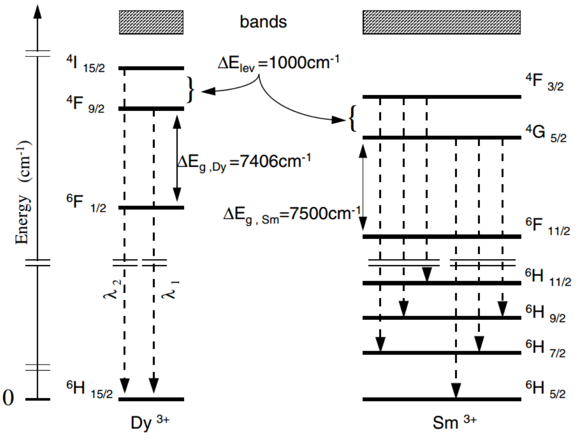

**Figure 2.5.:** Left: Schmatic energy level diagram for free ions of $Dy^{3+}$ and $Sm^{3+}$. Reused from [24].

In free $Dy^{3+}$ ion, ${}^4I_{15/2}$ state and ${}^4F_{9/2}$ state are closely distributed in the energy gap of 1000 $cm^{-1}$, whereas the next lower energy level ${}^6F_{1/2}$ stands 7400 $cm^{-1}$ apart. Here, the emission from both ${}^4I_{15/2}$ and ${}^4F_{9/2}$ states happens. At room temperature, because of non-radiative multi-phonon emission, the lower ${}^4F_{9/2}$ state is more populated than the upper ${}^4I_{15/2}$ state. With increasing temperature, in contrast, ${}^4I_{15/2}$ state is more populated by thermal pumping. Similarly, in $Sm^{3+}$, ${}^4F_{3/2}$ state and ${}^4G_{5/2}$ state are neighbouring in 1000 $cm^{-1}$ and the next ${}^6F_{11/2}$ energy level exists 7500 $cm^{-1}$ apart. The same mechanism happens in $Sm^{3+}$. Another example in this category is $Mn^{4+}$ [48].

The last example is $Pr^{3+}$, in which one of conflicting mechanisms overwhelms the other in different temperature ranges.

In $Pr^{3+}$, the state ${}^1D_2$ stays 4000 $cm^{-1}$ under the ${}^3P_J$ states. The next level ${}^1G_4$ state locates 7000 $cm^{-1}$ below it. Up to 1100 $K$, the non-radiative multi-phonon emission from ${}^3P_J$ states to ${}^1D_2$ state is stronger than thermal pumping acting in the opposite direction. Therefore, the intensity ratio of 610 $nm$ emission to 480 $nm$ emission increases gradually with increasing temperature. This is because an energy gap of 4000 $cm^{-1}$ between ${}^1D_2$ and ${}^3P_J$ states is relatively large to overcome in moderate temperature through thermal pumping. However, after 1100 $K$, thermal pumping is prevalent and the intensity ratio decreases with increasing temperature.

**Broadband emission phosphors** In $Eu^{2+}$, emission arises from the $(5d \rightarrow 4f)$ transition. The energy levels should degenerate, since only one electron occupies the $5d$ orbital. However, the $5d$ orbital is involved deeply in chemical bonding, thus the crystal field caused by interaction between the activator and the lattice can split the energy levels in several positions. The decreased crystal field stemming from thermal expansion results in increased emission state and shift of emission band in the direction to UV regime. (See

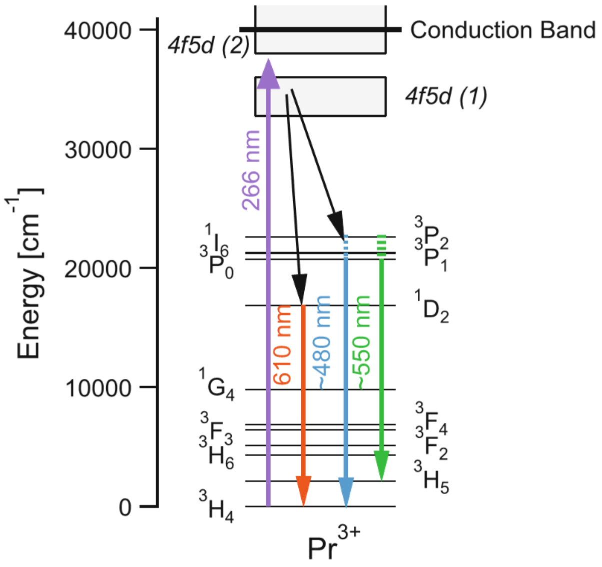

**Figure 2.6.:** Dieke diagram showing YAG:$Pr^{3+}$ energy levels for transitions between 4f states and locations of 4f5d bands. Reused from [44].

figure 2.7). On the other hand, the UV emission around 390 $nm$ in ZnO redshifts with increasing temperature. The reason for this is the decrease of band gap with increasing temperature [74].

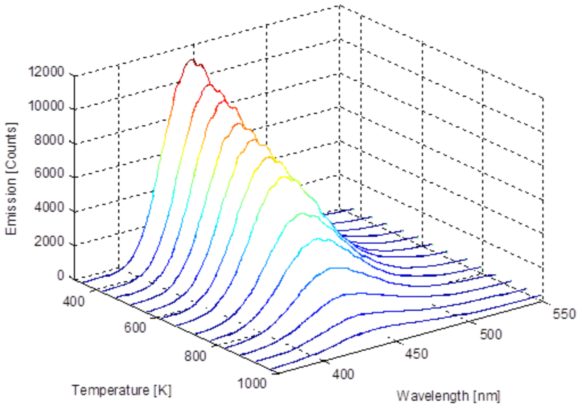

**Figure 2.7.:** Spectra of BAM:$Eu^{2+}$ at different temperatures.

**Selection of method for the gas thermometry** The lifetime method has been preferred to intensity ratio method in the application of the surface temperature measurement (Compare Table 3 with 5 in [16]). The lifetime method has superior accuracy and precision, since it has greater temperature sensitivity than the intensity ratio method of most of the phosphors [16, 31, 78]. Additionally, in the intensity ratio method, spectral transfer function reacts so sensitively to an optical alignment that in-situ calibration is necessary. In spite of these disadvantages, implementation of the intensity ratio method predominates in gas temperature measurement for the following reasons.

First, the turbulence should be resolved, which means the necessity of high temporal resolution. Furthermore, most fluids move faster than solids, and it is known that the intensity ratio method is more suitable when the objects move fast [16][31]. The object's displacement during a given measurement time should be limited to an order of magnitude smaller than the spatial resolution of the detection system. For example, if the spatial resolution of the detection system is 0.5 $mm$ and the gas velocity is 10 $m/s$, the exposure time should be the order of magnitude smaller than 50 $\mu s$ to freeze the object. Therefore, the requirement of short measurement time in gas thermometry is significant, and this is more critical to the lifetime method than the intensity ratio method. In the lifetime method, the frame rate of the detector should be fast enough to resolve the lifetime $\tau$ of selected phosphor. Considering that the available maximum sensor size of a CMOS camera, which is widely implemented for the lifetime method in 2 dimensional temperature measurements, decreases rapidly with increasing frame rate, it is clear that the lifetime method is constrained in gas temperature measurement for the limitation of the detector. In contrast, the intensity ratio method does not resolve the light in a given exposure but integrates it and it is relatively free from the constraints of fast phosphor.

Second, the gas thermometry suffers from the weak signal resulting from thinner particle number density than surface thermometry. Dividing the signal into small portions as in the lifetime method exacerbates this problem. Therefore, the intensity ratio method predominates in gas temperature measurements and has been used in this study. The specific experimental setup will be followed in section 3.2.

## 2.2. Imaging phosphorescence from particles in flow

**Absorption and scattering by a particle** Incident light on a particle suspended in a gas attenuates by the absorption in the particle and the scattering to all directions. This attenuation of light, i.e. scattering and absorption, is called extinction. In this study, the PIV used the scattering of 532 $nm$ light, while the thermometry is related to the absorption of 355 $nm$ UV light and the subsequent phosphorescence.

When a particle is illuminated by light, incident electromagnetic wave induces dipole moment in each subdivision in the particle. The oscillating dipoles emit radiation in all direction as shown in figure 2.8 and resultant superimposed light of wavelets is called scattered light [14].

Scattered light can be categorized according to size parameter $x_{sp} \equiv \pi d_p/\lambda$, here, $d_p$ denotes diameter of particle, $\lambda$ wavelength of exciting radiation. When $x_{sp} \ll 1$, or the size of the particle is much smaller than the wavelength of exciting radiation, Rayleigh scattering applies. In this regime, all the secondary wavelets are almost in phase and scattering does not vary in different direction. Rayleigh scattering intensity depends $2\pi/\lambda^4$ and also square of the volume of the particle, thus it is intense with excitation of short wavelength and large particle size. When $x_{sp} \geq 1$, Lorentz-Mie Theory (LMT) applies. In this regime, the wavelets interact each other and enhancement and cancellation of light occur, thus, peaks and valleys are observed in scattering pattern. LMT was developed for spherical particle, but has been extended its application to cylindrical and inhomogeneous

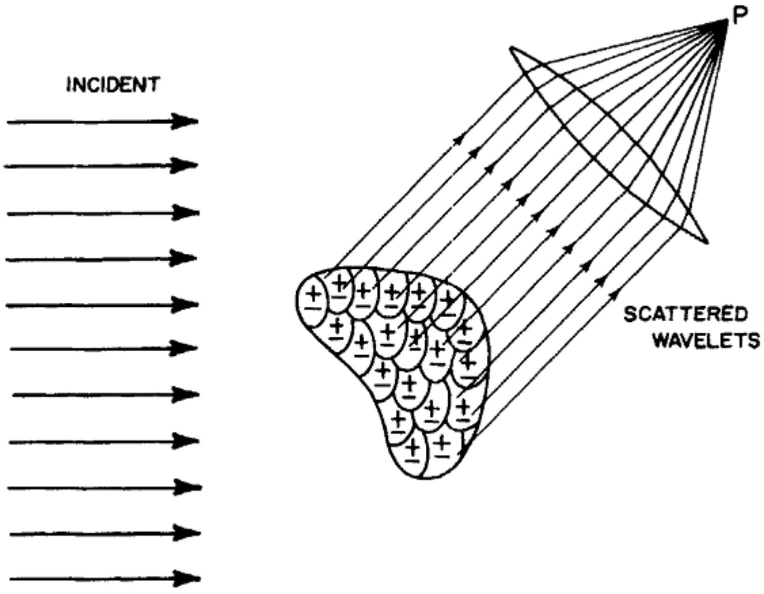

**Figure 2.8.:** Schematic of scattering. Reused from [14]

particles. As the last, when $x_{sp} \gg 1$, or the particle is much bigger than the wavelength of exciting radiation, the geometrical optics applies. Here, each ray reflects and refracts according to refractive index variation. The diffraction phenomena can not be considered by this method.

When the excited particle by illuminating light transforms energy into another form, e.g, heat, the absorption occurs. The total amount of absorbed energy in the particle is represented by the total incident energy with the definition of the absorption cross-section, $\sigma_A \equiv E_{abs}/E_i$, which is usually unknown. Here, $E_i$ means incident energy, and $E_{abs}$ absorbed energy.

**Irradiance distribution of particles in object plane** One can represent luminescence from micrometer-size particle distributed in the gas phase as point light source because the magnification in a typical imaging system is smaller than one. Let some particles with respective diameters be located at points, $\vec{x_p} = (x_p, y_p)$ in space and the laser fluence of $F_L$ excite the particles as shown in figure 2.9.

The ensemble of the particles could be defined by $\Gamma = \{\vec{x_p} | \vec{x_p} \text{ is location of the particles}\}$[1] and the diameter of each particle is defined by function of particle position, such as

$$d_p = \begin{cases} d_p & \text{if } \vec{x} \in \Gamma \\ 0 & \text{if } \vec{x} \notin \Gamma \end{cases}$$

With the previously introduced absorption cross-section, $\sigma_A$, Planck's constant, $h$, the frequency of exciting photon, $\nu_{freq}$, the total number of absorbed photons in a particle is

---

[1] Similarly with page 61 of [73]

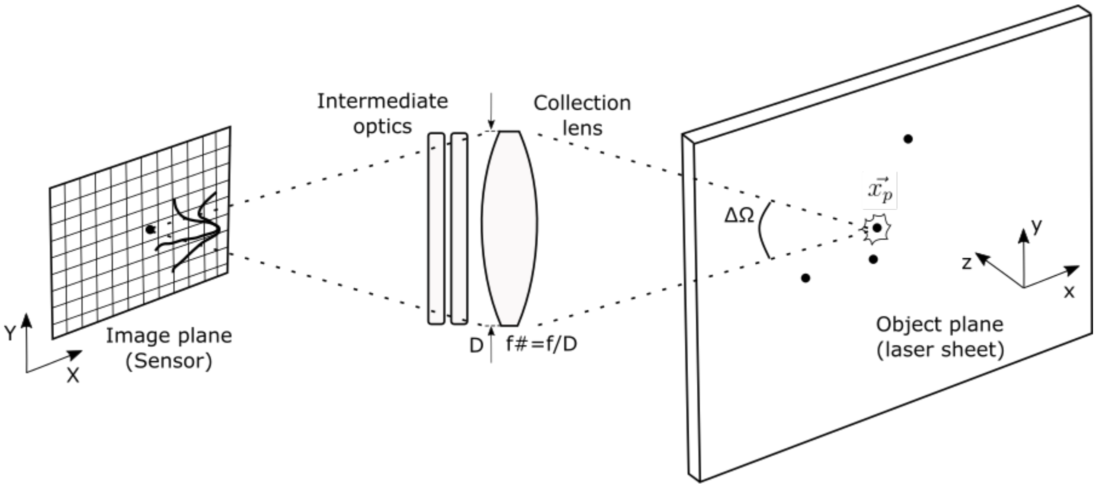

**Figure 2.9.:** Schematic of general planar imaging system of phosphor gas thermometry.

expressed as

$$\frac{F_L}{h\nu_{freq}}\frac{\pi}{4}d_p^2\sigma_A$$

Then, the number of emitted photons among absorbed one is expressed with the quantum efficiency, $\eta_q$,

$$\frac{F_L}{h\nu_{freq}}\frac{\pi}{4}d_p^2\sigma_A\eta_q$$

where, the quantum efficiency is defined as the ratio between the number of emitted and absorbed photons by the particle. Mostly, the absorption cross-section, $\sigma_A$ and the quantum efficiency[2], $\eta_q$ are unknown.

The emitted photons from a particle, the phosphorescence in this study, are collected by a lens and the solid angle subtending the lens[3], $\Delta\Omega$, determines the total amount of photons collected among the emission from the particle. The collected photons in the system pass through the optics, such as beam splitter, band pass filter, etc. Accordingly, the number of photons decreases according to the transmittance of optics. Finally, the total number of photons that arrive on the detector, $n_{ph,d}$, is obtained by integrating the multiplication of transmittance of intermediate optics[4] and the number of collected photons at different wavelengths.

---

[2] The quantum efficiency depends on the temperature and the laser fluence. The former make thermographic phosphor to be used for thermometry, but latter brings systematic error with varying laser fluence. This will be dealt in detail in Section 5.2.2.

[3] The solid angle is specified according to the particular imaging system.

$$\Delta\Omega = \frac{\pi}{4}\frac{m^2}{(f\#)^2(m+1)^2}$$

here, the $m$ denotes magnification, and $f\#$ is the f number, where $f\# = f/D$, $f$ is focal length, $D$ is size of the aperture [18].

[4] The transmittance of intermediate optics $\eta_o$ could be a function of incident angle on the optics, which means position of a particle, $\vec{x_p}$.

$$n_{ph,d} = \int_{-\infty}^{\infty} \frac{F_L}{h\nu_{freq}} \frac{\pi}{4} d_p^2 \sigma_A \eta_q \Delta\Omega \xi_o \mathrm{d}\lambda \tag{2.1}$$

where, $\xi_o$ is transmittance of intermediate optics. Then, the irradiance distribution of object plane $I_o$ is expressed as point light sources having different intensities. This could be expressed with equation (2.1) and the Dirac function $\delta$.

$$I_o(x, y) = \iint_{-\infty}^{\infty} n_{ph,d}(x, y)\delta(x - \chi, y - \psi)\mathrm{d}\chi\mathrm{d}\psi$$

**Point spread function and image forming** As mentioned previously, the particles in the object plane are point light sources with different intensities. This is represented 1-dimensionally in figure 2.10 (a). When the particles are imaged, however, they are not points, but somewhat blurred spots as shown 1-dimensionally in figure 2.10 (c). The blur stems from the diffraction of the light and the possible aberration of the optics. This blurring is expressed mathematically by a point spread function[5][6], and the corresponding

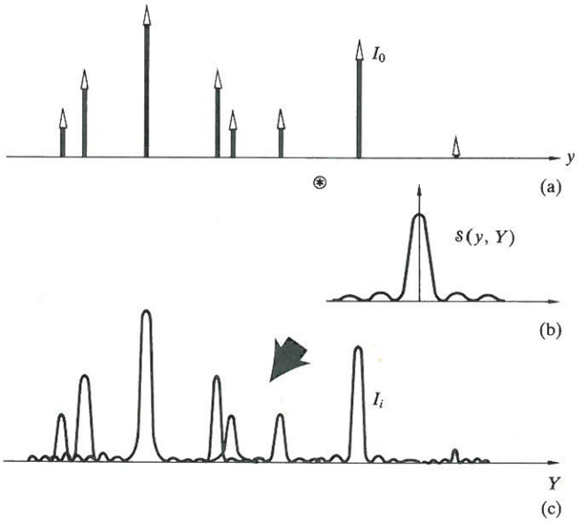

**Figure 2.10.:** Illustration of 1-dimensional image formation procedure. The object (a) is convoluted with the point spread function (b) and (c) represents the corresponding image as the result. Reused from [37]

---

[5] After assuming the imaging system as linear, the output of the system or the image could be represented in terms of the response to certain elementary input, which is called impulse response in general and point spread function in the imaging system. For the definition of impulse response, refer page 18 of [33].

[6] In the diffraction limited system, the point spread function is airy function. In the presence of lens aberration, analysis on the modulation transfer function helps to measure the point spread function. See page 38-46 of [73]

irradiance distribution of image $I_i$ to the object is the convolution of the point spread function and the object.(See page 483-486 of [37])

$$I_i(X,Y) = \iint_{-\infty}^{\infty} n_{ph,d}(x,y) H(x,y;X,Y) \mathrm{d}x \mathrm{d}y \tag{2.2}$$

here, $H(x,y;X,Y)$ denotes the point spread function.

**Conversion of photons to counts on a CCD chip** The photons impinged on a pixel of a CCD array are converted to electrons by the photoelectric effect according to the quantum efficiency of the sensor. The quantum efficiency of the sensor has a spectral dependence and usually provided by the manufacturer. Accumulated charges on a pixel migrate to the charge (or on-chip) amplifier through shift register and are converted to voltage and finally to a gray value, counts by an analog-digital converter.

# Chapter 3.

# Measurement system

Experimental set-up and data reduction algorithms used in the present study are described in this chapter. The system for spectra measurement from packed powder in an oven, of which results are presented in chapter 4, will be explained first. The one for the simultaneous measurement of the velocity and the temperature by aerosolized particles, which chapter 5 and 6 deal with, will follow. In each section, an environment of a phosphor particle, optical set-up, and reduction algorithms from the raw data to corresponding scalars will be explained in detail.

## 3.1. Spectra measurement

To measure the spectra of phosphorescence at different temperatures, the packed powder of a phosphor was prepared and placed in an optically accessible oven. The phosphor was excited with a laser, and the spectrum was resolved with a spectrometer and imaged on a camera sensor. The images were converted to spectra by an algorithm.

### 3.1.1. Sample preparation and oven

As a measurement sample to be positioned in the oven, the phosphor powder was squeezed moderately by a thin metal rod in a hole of a stainless steel plate. The plate had 8 holes and different phosphors could be filled in the holes at the same time. Both the diameter and the depth of each hole were 3 $mm$. The inner diameter of the oven (Carbolite, CTF 12/100/900) was 105 $mm$ and the length was 900 $mm$. The maximum temperature in this set-up was 1200 $K$. An N-type thermocouple contacted the backside of the metal plate, and this temperature was regarded as the reference temperature of the phosphor sample. The oven was on a translation stage such that it can be shifted precisely in the direction of $x_s$ axis in figure 3.1. Accordingly, the other light sources, such as integrating sphere, calibration lamp or beam profiling camera could be placed in the position of focal point of the achromatic lens.

### 3.1.2. Optical system

The sample was excited by the third or fourth harmonic of a single-pulse, Q-switched 10Hz Nd:YAG laser (Quanta Ray, Indi Series) at 355 $nm$ or 266 $nm$ according to the absorption of the phosphor. The Pellin-Broca prism separated the light spatially into different wavelengths that light with the wavelengths out of the interest could be blocked.

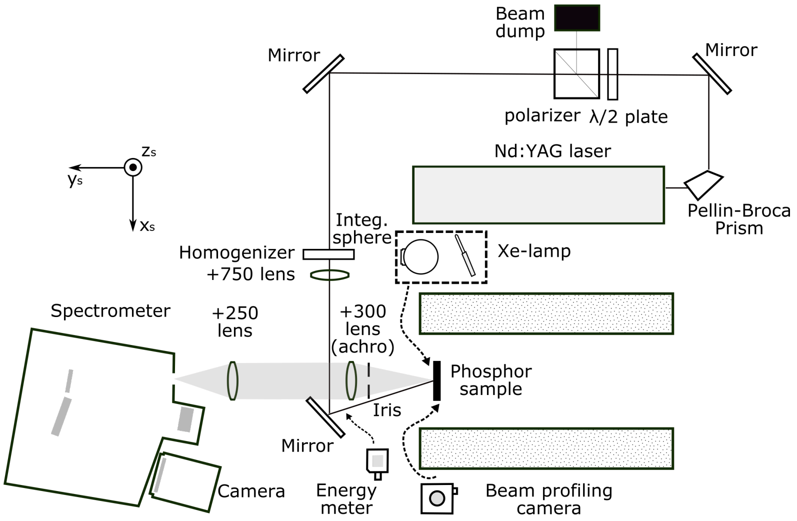

**Figure 3.1.:** Experimental setup for spectra measurement.

The laser was operated at full power to minimize the drift in time and attenuated by a combination of $\lambda/2$ plate and Glan polarizer. The beam was homogenized by a beam homogenizer (Holo Or, HM-210-UYA), and the focal length of the lens after the beam homogenizer determined the size of the beam and the working distance[1] where the phosphor sample was placed. The profile of the beam was measured with a beam profiling camera (Data Ray Inc., WinCamD series) at the working distance. The laser energy was monitored by an energy meter (Gentec, QE25-SP) after the last mirror. The laser fluence was calculated by using the size and the energy of the beam from above measurements.

The emitted phosphorescence was collected with an achromatic lens placed at focal point from the probed phosphor to parallelize the emitted light, while minimizing the effect of chromatic aberration. The parallelized light was focused at the slit of the spectrometer (HORIBA Jobin Yvon, 270M(Spex)) by a spherical lens. The light was collimated with a concave mirror inside the spectrometer and diffracted by the grating with a groove density of 600 grooves/mm. The spectrum was focused on the imaging sensor of an sCMOS camera by a concave mirror (f = 270 mm). An sCMOS camera (Lavision, Imager sCMOS, 2560 × 2160 pixel, 6.5 × 6.5 $\mu m^2$ pixels size) was used to detect the spectrum. The exposure time of the camera was determined according to the life time of the phosphor in measurement as summarized in table 4.1. To synchronize the camera and the laser, a pulse generator (Quantum composer, 9520) was used. The slit width of the spectrometer was fixed at 100 $\mu m$ and the resolution of detection system was around 0.9 $nm$ based on the fwhm of 467.1 $nm$ peak of a Xe lamp[2] (LOT-Oriel, LSP033), used for the wavelength calibration. Around 200 nm wavelength range could be imaged at once. An iris was placed in front of the achromatic collecting lens to position the light sources (phosphor samples, Xe lamp, integrating sphere) at the same position. With the iris almost closed, the position of the light sources were adjusted by translation stage in $x_s$ direction until the signal in the detector was maximized.

---

[1] Here, the working distance means the position where the beam is homogenised.

[2] Emission of the lamp has narrow and discrete line spectrum.

### 3.1.3. Data reduction algorithm

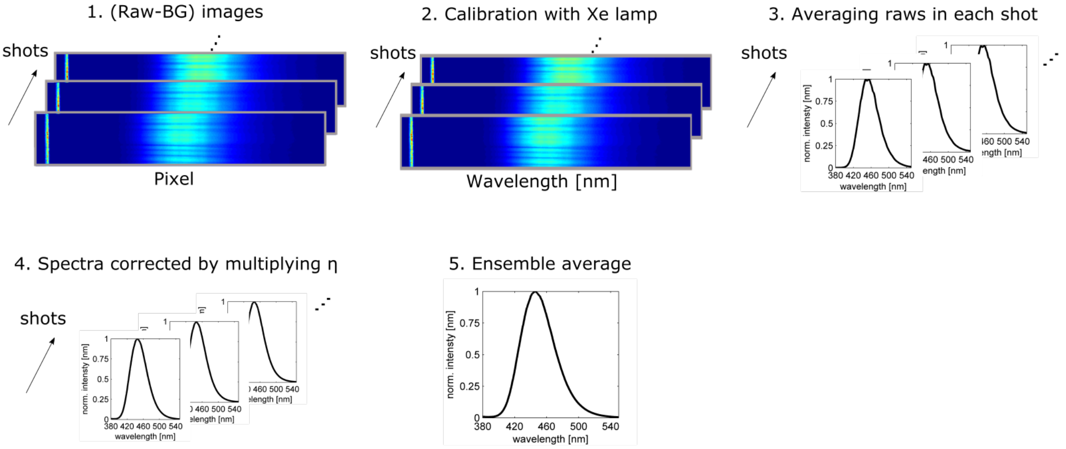

**Figure 3.2.:** Schematic of data reduction algorithm for a spectrum.

The recorded images were converted to spectra by an algorithm, which is schematically depicted in figure 3.2. In each case, 137 shots were imaged and each image was subtracted later with the background image. The background image was obtained by recording the images with the laser blocked in the same configuration and averaging them. The examples of background subtracted raw images are shown in figure 3.2.

After subtracting the background, the image was linearly interpolated according to the wavelength corresponding to the pixel position based on the wavelength calibration. For the wavelength calibration of the spectrometer, the oven was shifted by using a translation stage and the aforementioned low pressure discharge Xe lamp was positioned at the same position and imaged on the sensor. From the image, locations of the peaks as pixel number were identified and correlated with the corresponding wavelengths of the peaks. The line spectrum of the lamp were provided by the manufacturer. By fitting the points with a curve, the wavelength calibration of the spectrometer was achieved. The spectrum of the Xe lamp after the wavelength calibration is drawn in figure 3.3.

After the wavelength calibration, every row in each shot was averaged as shown in figure 3.2 denoted by step 3. The 2-dim spectra images reduced to 1-dim spectra profiles.

However, these spectra profiles are different from the ‘true’ spectra, since the transfer function of the detection system, $\phi$ depends on the wavelength. The transfer function means how the components such as lenses, grating, and sensor affect the spectrum. A reference light of integrating sphere (Gigaherz-Optik, UMBB-300) illuminated by 100 $W$ tungsten-halogen lamp was placed at the position of the phosphor sample and imaged by the detection system. The transfer function, $\phi$ could be measured by dividing the measured spectrum, $M$, with the reference, $R$, provided by the manufacturer and normalizing it, $\phi = (M/R)/max(M/R)$. The curves are drawn in figure 3.4. The spectra in step 3 in figure 3.3 was corrected by dividing the transfer function and drawn in step 4. Lastly, the ensemble average of spectra from single shots were regarded as spectrum in a certain case.

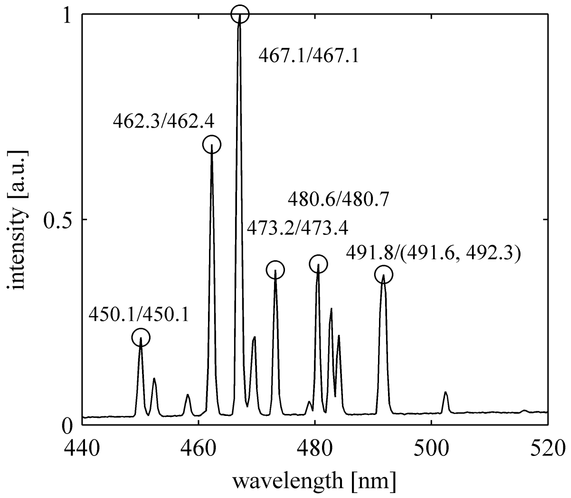

**Figure 3.3.:** Measured spectrum of the Xe lamp for the wavelength calibration of the spectrometer. The notation, A/B, denotes a measured peak wavelength [nm], A, and a peak wavelength [nm] provided by the manufacturer, B.

## 3.2. Temperature and velocity measurement

To measure the velocity and temperature of an air flow with phosphor particles, the air was seeded with the particles and heated to high temperature. The particles suspended in the laser, and subsequent Mie scattering and phosphorescence were imaged onto a detection system. The temperature was deduced from the recorded images by an algorithm introduced here, and the velocity by a commercial software (Lavision, Davis 8.2).

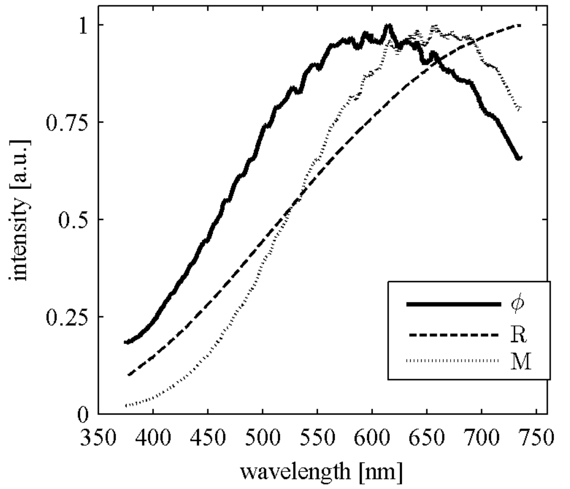

**Figure 3.4.:** The transfer function of the detection system. Measured and given spectra of the integrating sphere are denoted as M and R. The transfer function is denoted by $\phi$.

### 3.2.1. High temperature seeded jet with co-flow

The configuration to realize the air flow is sketched in figure 3.5. First, phosphor particles were dried for a few hours at 400 $K$ before being aerosolized. Then, the particles were entrained into the air by an in-house fluidized bed aerosol generator. An orifice at the outlet of the seeder was attempted to separate aggregated particles by strong shear force. The seeded air was heated by an electric heater (denoted by an orange arrow in figure 3.5) and mixed with another unseeded air flow (denoted by a red arrow in figure 3.5) heated by 3.5 $kW$ inline heater (Sylvania, Hot Air Tools). By adjusting the portion of seeded and unseeded air, the seeding density could be adjusted. The two flows were mixed well in counterflow configuration, which was also designed for the mixed air not to reach the inline heater. The mixed air passed through the nozzle shape introduced in [60] minimizing air separation. The inner diameter of the tube, $d$, was 16 $mm$ and the length of the straight part of the tube was long enough (500 $mm > 31d$) to assume fully developed turbulent pipe flow at the jet exit. Insulation helped to preserve the heat energy. The jet was mounted concentrically with the outlet of wind tunnel [60] to realize a co-flow, which was designed to prevent the surrounding unseeded air in the lab being entrained to the flow. The co-flow was seeded with the BAM particles by the aforementioned same type seeder , but was not heated. The diameter of the co-flow was 140 $mm$ at the outlet. The whole set-up could be translated in the $x$ direction in figure 3.5. This coordinate was applied to all analysis in Chapter 5 and 6. By lowering the whole set-up while keeping the optical set-up, such as laser sheet and the cameras, the jet at different axial positions ($x = 1, 4, 8, 15d$) could be investigated. By increasing the flow rate, two jet $Re$ were measured. More details on measurement conditions are summarized

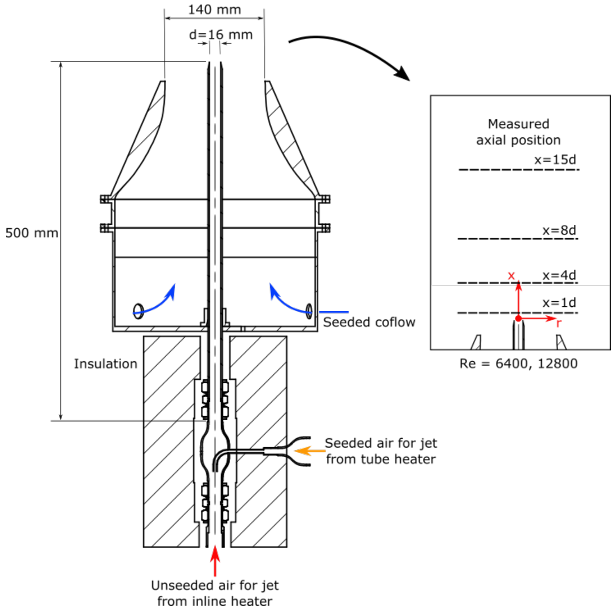

**Figure 3.5.:** Nozzle shape.

in Table 3.1.

**Table 3.1.:** Experimental conditions.

| | Jet exit temperature | Coflow temperature | Jet bulk velocity | Coflow bulk velocity | Jet maximum velocity |
|---|---|---|---|---|---|
| Re 6400 | 614 K | 315 K | 21.13 m/s | 0.16 - 0.24 m/s | 36.4 m/s |
| Re 12800 | 618 K | 310 K | 42.26 m/s | | 73.4 m/s |

Temperatures were measured by thermocouple.

### 3.2.2. Optical system

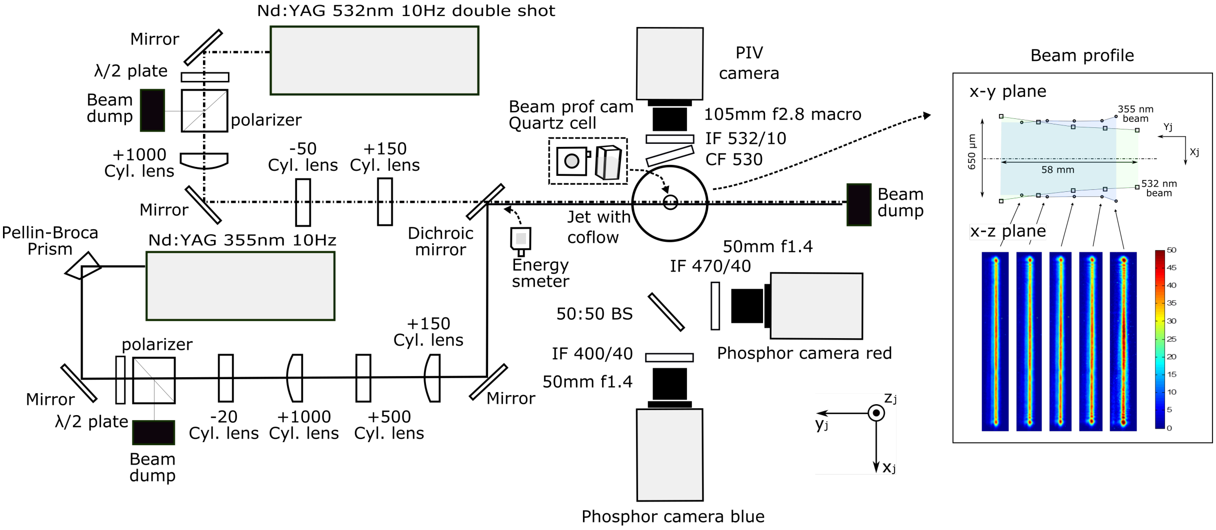

**Figure 3.6.:** The schematic of optical system for the simultaneous measurement of velocity and temperature.

**Velocity measurement** The particles suspended in air were excited by 532 *nm* light at 10 Hz by the second harmonic of double shot Q-switched Nd:YAG laser (New Wave Research, Gemini PIV 200-15) to produce Mie scattering for the velocimetry. The time delay between the shots from the two cavities were 5 $\mu s$. The energy of the beam was adjusted by a combination of a $\lambda/2$ plate and a Glan polariser as shown in figure 3.6. A sheet optics comprised of three cylindrical lenses shaped the beam to have the thickness ranging from 0.45 to 0.7 *mm* at the measurement area. The 532 *nm* beams were well aligned with UV beam for phosphor excitation. The beam profile were measured with the beam profiling camera (DataRay Inc., WinCamD series) and drawn in the insert of figure 3.6 as green with 355 *nm* profile in blue.

The Mie scattering was imaged with an sCMOS camera (Lavision, Imager sCMOS, 2560 × 2160 pixel, 6.5 × 6.5 $\mu m^2$ pixels size) mounted with Nikkor 105 *mm* macro lens stopped at f#=8. The magnification was around 0.29 and imaged area was 57 × 48 $mm^2$. A 532 *nm* band pass filter was placed in front of the camera objective, and the additional color filter (Schott, GG530) was put ahead of the 532 *nm* filter to prevent reflected phosphorescence by the 532 *nm* filter being imaged on the phosphor camera. The color filter was tilted that the reflected Mie-scattering by phosphorescence filters was not imaged in the PIV camera.

**Temperature measurement** The same particles used for velocity measurement were excited by 355 *nm* light at 10 Hz, which was generated by the third harmonic of a single-pulse, q-switched Nd:YAG laser (Quanta Ray, Indi Series) to produce phosphorescence for the thermometry. The laser was operated at full power, and the energy was adjusted by a $\lambda/2$ plate and a Glan polariser. The 355 *nm* laser was triggered 1 $\mu s$ before the first shot of 532 *nm* light. A laser sheet was formed with combination of four cylindrical lenses and superimposed with the 532 *nm* laser sheet by a long pass dichroic mirror. As will be discussed in Section 5.2.2, using a homogeneous beam was important to avoid systematic error. Therefore, the beam was expanded vertically with a $f$ =-20 *mm* focal length cylindrical lens, and a nearly top-hat beam profile was obtained by using only the center part of the beam (only 10 % of the total energy) while blocking the rest. Telescopes were implemented to have a parallel beam in both vertical and horizontal directions. The height and thickness of the beam were measured by imaging the fluorescence from dilute solution of a dye (Radiant Dyes Laser, Coumarin 307) contained in quartz cell at different radial positions. The measured height and thickness of the beam were 15 *mm* and 0.65 *mm* at measurement area, respectively and are shown in the insert of figure 3.6.

The emission following the excitation was imaged by a carefully designed detection system. The phosphorescence was divided into two optical paths by a 75 mm×75 mm, 50:50 beam splitter with an anti-reflective coating on the backside (Edmund, #46-462). Instead of 50:50 beam splitter, one can use a dichroic beam splitter to maximize the amount of split light. In this case, however, angular dependency of transmittance of the dichroic beam splitter, from which the 50:50 beam splitter is free, will be an issue. An additional achromatic lens can help to solve this issue by parallelizing the emission while increasing the solid angle at the same time.

To design filter sets placed after the beam splitter, the band of each channel should be decided. However, as will be shown, with narrower filter bands, more sensible intensity ratio to temperature could be obtained at cost of signal loss, and with broader bands, vice versa: the temperature sensitivity and the amount of signal conflict each other. For the optimization of filter sets to achieve high temperature precision, a mathematical model was developed.

First, the effect of camera noise on the precision of temperature could be modelled theoretically [27]. The camera noise, one of the significant factors in precision, is comprised of shot and read noise[3]. When photons impinge on a pixel, the photoelectric effect converts the photons to electrons. The number of accumulated electrons, $n_e$, is changed to counts, $\Sigma$, with the factor (counts/$e$), $K$. The relation of generated photoelectron with the number of impinged photon follows Poisson distribution; therefore, the variance of generated electrons is the same as its mean, $\Sigma/K$ and the variance of counts is expressed as $K\Sigma$ according to the error propagation. This uncertainty is called the shot noise. Another uncertainty in camera noise is incurred during the conversion of the accumulated charge to the counts, which is called read noise [18]. One can obtain the read noise experimen-

---

[3] Here, the noise is represented by one standard deviation

tally by measuring the standard deviation of counts of each pixel while the camera lens is covered by a cap. Although, the fluctuation of the dark current is also included here, its portion is generally regarded minimal in a cooled CCD array. The average of standard deviations of the pixels could be interpreted as the read noise of the camera. The variance of signal in each pixel, which is comprised of shot and read noise, might be obtained by adding the variances of two noises on the assumption of no correlation between them. Therefore, the standard deviation of the signal is

$$\sigma_{\Sigma_i} = \sqrt{K\Sigma_i + N_{cam}^2}$$

here, $\Sigma_{i=A,B}$ denotes counts in blue and red channel, respectively, $N_{cam}$ denotes the read noise of a camera.

The influence of data reduction on temperature precision should be considered (a detail explanation on the data reduction will follow soon). The images from blue and red channels are registered[4], then divided to produce the ratio image, $r = \Sigma_A/\Sigma_B$. After assuming no correlation between the error of blue and red channels, the standard deviation of intensity ratio, $\sigma_r$ is expressed according to the error propagation as

$$\frac{\sigma_r}{r} = \sqrt{\left(\frac{\sigma_{\Sigma_A}}{\Sigma_A}\right)^2 + \left(\frac{\sigma_{\Sigma_B}}{\Sigma_B}\right)^2}$$

Typically a smoothing filter (e.g. median filter, moving average filter) is applied to decrease the noise after the division, and averaging $N_{ker}$ samples decreases the standard deviation with the factor of $1/\sqrt{N_{ker}}$. After smoothing, the ratio is converted to the temperature by a calibration curve, $T = f(r)$. Then, the standard deviation of temperature could be expressed as

$$\sigma_T = \frac{dT}{dr} r \sqrt{\frac{1}{N_{ker}}\left[\left(\frac{\sigma_{\Sigma_A}}{\Sigma_A}\right)^2 + \left(\frac{\sigma_{\Sigma_B}}{\Sigma_B}\right)^2\right]} \tag{3.1}$$

As shown in the equation 3.1, the precision improves with high temperature sensitivity $(1/\frac{dT}{dr})$, strong signal $(\Sigma_A, \Sigma_B)$, and small intensity ratio, $r$. To predict the temperature precision with given filter sets by equation 3.1, the information of $1/\frac{dT}{dr}$ and $\Sigma_A, \Sigma_B$ are needed.

First, the temperature sensibility $(1/\frac{dT}{dr})$ could be calculated by differentiating the virtual calibration curve. Here, the virtual calibration curve is obtained by using the measured spectra in the oven at each temperature, $\Gamma(\lambda, T)$, (the experimental setup was introduced in Section 3.1 and the results will be presented in Chapter 4) and the transmittance, $\xi$ of the filters. The virtual intensity ratio at each temperature, $r(T)$ is obtained by dividing the virtual signals, which are integration of the convolution of the measured spectra of BAM in an oven, $\Gamma(\lambda, T)$, and filter sets, $\xi$.

$$r(T) = \frac{\Sigma_A}{\Sigma_B} = \frac{\int_0^\infty \Gamma(\lambda, T)\xi_A(\lambda)d\lambda}{\int_0^\infty \Gamma(\lambda, T)\xi_B(\lambda)d\lambda} \tag{3.2}$$

---

[4] Remaining misalignment from the imperfect image registration will result in additional noise. This effect is not included in the model due to the difficulties in quantification.

Second, the signal, $\Sigma_A$ (or $\Sigma_B$) is possible to be roughly estimated from the spectra with a reference signal measured from seeded particles as also proposed in [27]. They suggested following equation to evaluate expected signal intensity of BAM with different filter sets at a temperature from spectra measurement in an oven.

$$\Sigma_A = \Sigma_{A,ref} \times \frac{N_p}{N_{p,ref}} \times \frac{\int_0^\infty \Gamma(\lambda,T)\xi_A(\lambda)d\lambda}{\int_0^\infty \Gamma(\lambda,T)d\lambda} \times \frac{\int_0^\infty \Gamma(\lambda,T_{ref})d\lambda}{\int_0^\infty \Gamma(\lambda,T_{ref})\xi_{A,ref}(\lambda)d\lambda} \times \frac{Q(T)}{Q(T_{ref})} \times \frac{S(F_L)}{S(F_{L,ref})} \tag{3.3}$$

here, $N_p$ is the particle number density, $Q$ is a function reflecting relative signal intensity at various temperatures measured from seeded particles in the air, and $S$ is a function accounting for the total emission intensity according to the laser fluence. $ref$ state denotes the condition, such as seeding density, temperature, laser fluence, in which the reference signal intensity from seeded particles in the air, $\Sigma_{A,ref}$ was measured. The equation 3.3 could be simplified further with following assumptions.

The seeding density, $N_p$ is assumed to be a constant. Seeding density of $1.2 \times 10^{11}/m^3$ is plausible because it is typical one for PIV, which means 15 particles per interrogation window size of $(500\mu m)^3$. Although the seeding density fluctuates in actual measurements, seeding density was set to fixed value because the purpose of the model is roughly estimating the temperature precisions with given filter sets. By set the $N_{ref}$ same, the term, $\frac{N_p}{N_{p,ref}}$ vanished. The laser fluence was assumed to be same with the one in the reference measurement, and then the term $\frac{S(F_L)}{S(F_{L,ref})}$ also vanished. The function Q was cancelled after assuming same thermal attenuation of the signal in seeded particles and packed powder in oven, therefore $\frac{\int_0^\infty \Gamma(\lambda,T_{ref})d\lambda}{\int_0^\infty \Gamma(\lambda,T)d\lambda} \times \frac{Q(T)}{Q(T_{ref})} = 1$. It is required to pay particular attention to this assumption because multiple scattering dominates optical properties in packed powder and physical damage by heat and the laser excitation is possible in the oven measurement. This issue should be investigated in near future. After assuming above, the equation is simplified as

$$\Sigma_A(T) = \Sigma_{A,ref} \times \frac{\int_0^\infty \Gamma(\lambda,T)\xi_A(\lambda)d\lambda}{\int_0^\infty \Gamma(\lambda,T_{ref})\xi_{A,ref}(\lambda)d\lambda} \tag{3.4}$$

To optimize the filter bands, the transmissions of bench-marked filter sets were selected from previous studies [29, 52] and summarized in figure 3.7 (a) with normalized spectra of BAM at different temperatures. The expected signal (figure 3.7 (b)) and the virtual calibration curve (figure 3.7 (c)) were calculated by the equation (equation 3.1 and 3.4) and the precision of temperature were predicted as shown in figure 3.7 (d). The filter set 1, which produced the best precision, was chosen (Chroma Technology, ET 400/40x and ET 470/40x).

It was difficult for phosphor thermometry to obtain reasonable SNR with the lens having high f # such that Nikkor 50 mm lenses stopped at f#=1.4 with 8 $mm$ extension rings were used for both cameras in this study. The phosphor thermometry suffers from low signal as PLIF or Rayleigh scattering. It is required to use a camera lens having higher f# than 1.2 for PLIF or Rayleigh scattering [18]. For imaging phoshorescence, interline transfer CCD cameras (PCO, sensicam qe, 1376×1040 pixel, 6.45×6.45 $\mu m^2$ pixel size) were used for both 'blue' and 'red' channels. Both cameras opened 2 $\mu s$ before the UV laser shot, and the exposure time was set to 5 $\mu s$, acquiring full phosphorescence. The life time of the BAM phosphorescence is around 2 $\mu s$ at room temperature [52]. All cameras and lasers were synchronized by a pulse generator (Quantum composer, 9520). Although the 532 $nm$ illumination presented during the exposure of phosphor camera, the optical density of the phosphorescence filters (ET400/40x: 7.39, ET470/40x:8.00 given from manufacturer) were high enough to suppress them. This suppression was confirmed

(a) Spectra and filter sets

(b) Signal prediction

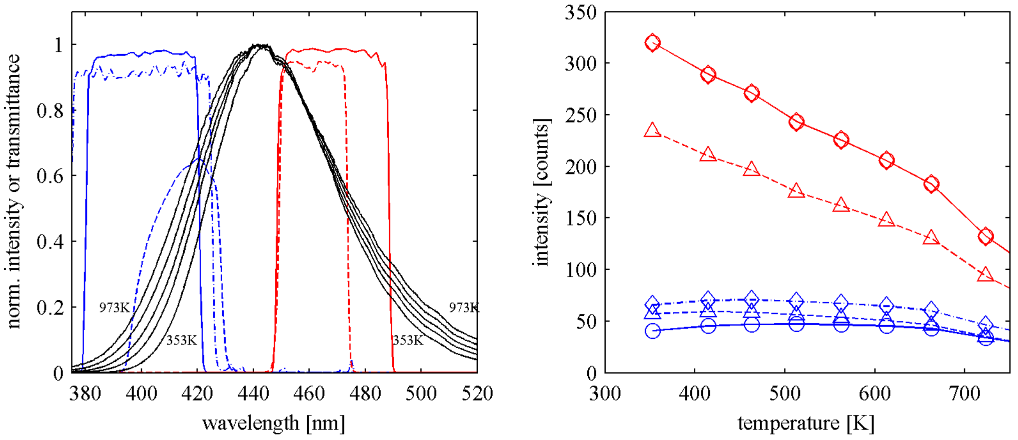

(c) Virtual calibration curve

(d) Prediction of temperature precision

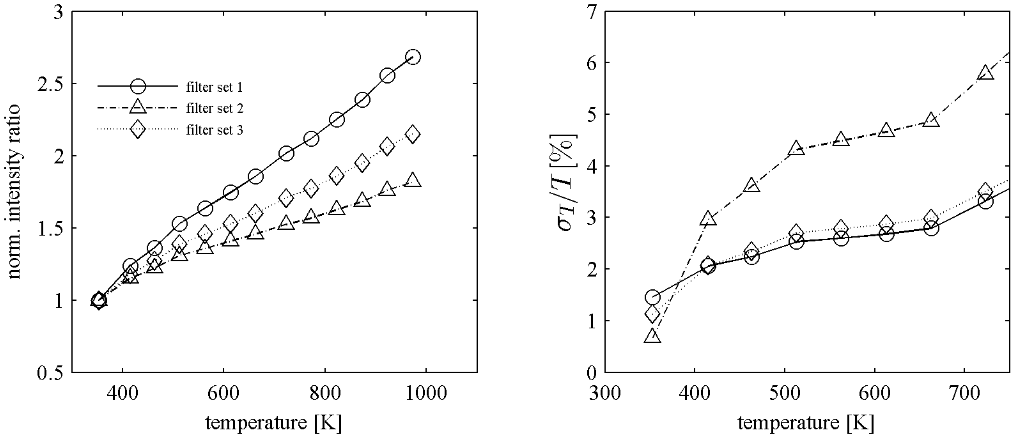

**Figure 3.7.:** Predicting the precision of temperature with given filter sets for filter optimization.(a) notation (blue;cwl-fwhm/red;cwl-fwhm): solid line, filter set 1(400-40/470-40); dashed line, filter set 2 (415-30/460-14) used in [29]; dash-dot line, filter set 3 (400-50/460-14) used in [52]; (b) blue symbols denote signal of blue channel, red symbols red channel: circle, filter set 1; triangle, filter set 2; diamond, filter set 3; (c) and (d) have same legend.

by recording images without UV illumination but only with 532 *nm* illumination. The magnification was around 0.15 and a 4 by 4 hardware binning was applied to reduce read-out noise, resulting in a corresponding area of 170×170 $\mu m^2$ at the object plane.

### 3.2.3. Data reduction algorithm

**Velocity measurement** As already mentioned, the velocity field was deduced from Mie-scattering image by the commercial cross-correlation algorithm implemented in Davis 8.2. Multi-pass iterative procedure in decreasing window size (1 pass at 64 × 64 pixels, 3 passes at 24 × 24 pixels with 50 % overlap) was applied. The spurious vectors were removed by a median filter. The resultant interrogation window size was 480 $\mu m$ and the velocity fields were linearly interpolated to the grid of the temperature field.

**Temperature measurement** The raw images from both 'blue' and 'red' channels were subtracted with background images, which were recorded without laser excitation. After the subtraction, both images were mapped each other with the image registration algorithm implemented in Davis 8.2. This algorithm used images of a dot mark plate (Lavision, type 7) taken by both cameras in the same set-up. After the image registration with Davis 8.2 algorithm, residual mismatching could exist possibly from the misalignment between the dot mark plate and the laser sheet. An intensity based automated image registration algorithm implemented in Matlab [56] was attempted to solve the remaining disparity, when required.

After image registration, the 'blue' image was divided pixel by pixel by the 'red' image producing the intensity ratio image. To compensate for the different light collecting efficiency stemming from the effects, such as vignetting and inhomogeneous sensitivity of CCD sensor, a flat field correction was applied by dividing each ratio image by ensemble averaged intensity ratio image at room temperature. After that, a 3 by 3 median filter was applied to the intensity ratio image for denoising.

A calibration curve for converting the intensity ratio image to temperature was attained by measuring intensity ratio of area with known temperature. Here, controlling the laser fluence and the seeding density as same with the actual measurement was important because these factors also affected the intensity ratio and brought systematic errors as will be explained in Section 5.2.2 and 5.2.3. Therefore, the laser fluence was maintained as 55.4 $mJ/cm^2$ for the calibration and the actual measurement. Furthermore, only the images satisfying the criteria of seeding densities explained in Section 5.2.3 were selected for calibration and actual measurements for data reduction. The seeding density was extracted from the Mie image by a particle locating algorithm, which will be explained soon. A part of the jet core ($1.7 \times 1.7 mm^2$, 10×10pixels, at $x/d = 0.7$), where the jet is not yet mixed with surrounding air, thus, the temperature was homogeneous, was exploited for the calibration curve measurement. The reference temperature was obtained by using 0.5 *mm* K-type thermocouple at the position after the jet reached the steady state. At each temperature, 300 shots were measured and only the images satisfying the suitable seeding density criteria were used for the calibration. The number of selected images with suitable seeding densities in each temperature is stated in table 3.2. The averaged intensity ratios at jet core were related with the reference temperature. The attained calibration curve is shown in figure 3.8.

**Table 3.2.:** The number of images at each temperature case used for the calibration curve measurement. Temperatures were sampled from 100 pixels in each image.

| Temperature $[K]$ | 293 | 345 | 418 | 497 | 616 |
|---|---|---|---|---|---|
| # of samples | 88 | 198 | 47 | 3 | 47 |

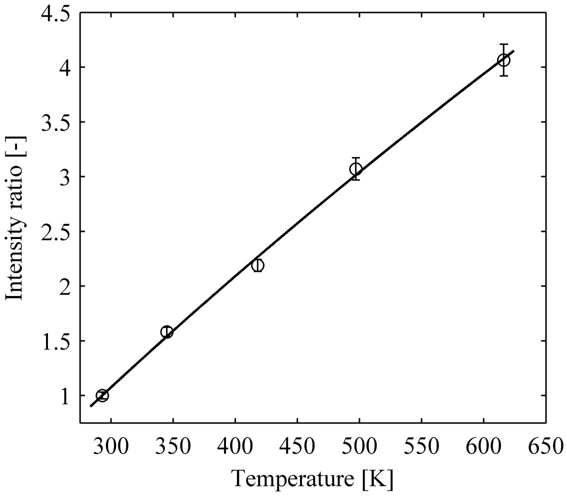

**Figure 3.8.:** Calibration curve. The circle denotes ensemble averaged intensity ratio and bar one standard deviation.

**Table 3.3.:** Selected number of shots in turbulent flux measurement.

| | Re 6400 | Re 12800 |
|---|---|---|
| $x = 1d$ | 311 | 157 |
| $x = 4d$ | 859 | 618 |
| $x = 8d$ | 1354 | 867 |
| $x = 15d$ | 854 | 675 |

With the calibration curve, the intensity ratio image were converted to temperature field and the general procedure is summarized as a flow diagram in figure 3.9 and an example of temperature field after this procedure is shown in figure 3.10 denoted by ‘Temperature’.

Different from gas tracers for LIF, such as a toluen or an aceton, the distribution of thermographic phosphor particles are inhomogeneous; local regions (below 5% of total

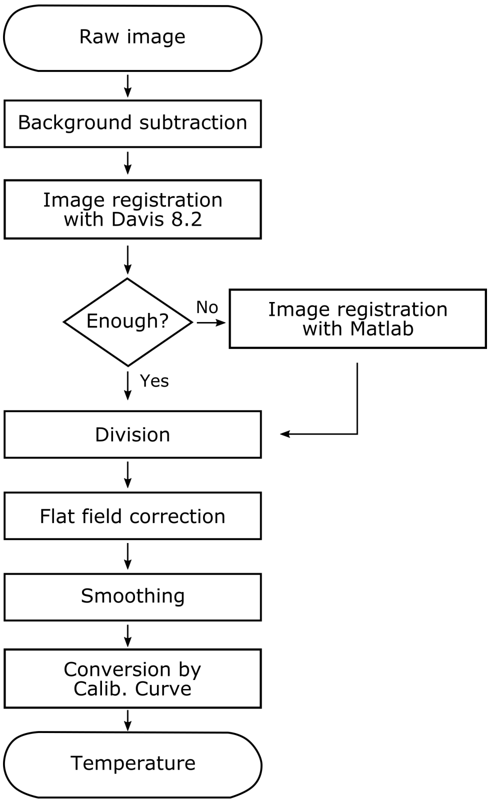

**Figure 3.9.:** Flow diagram.

area) having exceedingly high or low signal could exist. The technique, therefore, requires masking (filtering out in temperature calculation) those regions where (1) a count level was below seven: twice the read-out noise, no signal, but an error and (2) a count level was exceeding four times the average signal level: these exceedingly high phosphorescence levels (below 1% of total area) were most probably due to large particles or particle conglomerates that might show very different thermal and fluidic properties compared to small single particles. (3) no particle presented: due to multiply scattered light, the signal can exceed count level over seven counts. The reason and way of obtaining masks for (1) and (2) are straightforward, thus, only the procedure to attain a mask for (3) is explained. The mask(1) and (2) are illustrated in figure 3.10 as 'Mask(1)' and 'Mask(2)'.

Where no particle are presented, it was suspected that the multiple scattering could cause a systematic error in this region as will be shown in Section 5.2.3. An algorithm similar to [28] was used to recognize the regions with no particles. The algorithm used Mie scattering image recorded at the same time with corresponding phosphorescence image (see 'Mie image' in figure 3.10). The background in Mie image was homogenized by subtracting the filtered Mie image using 30 by 30 moving average top-hat filter (not shown in figure 3.10). Particle locations were then identified by finding local maxima from the filtered Mie image by an algorithm implemented in Matlab ('imregionalmax' in Matlab produce a binary image that identifies the local maxima. When the value in a pixel is larger than surrounding 8 pixels, 1 is returned for the position, else 0. The algorithm scan pixel by pixel). These local maxima were regarded as possible peaks by

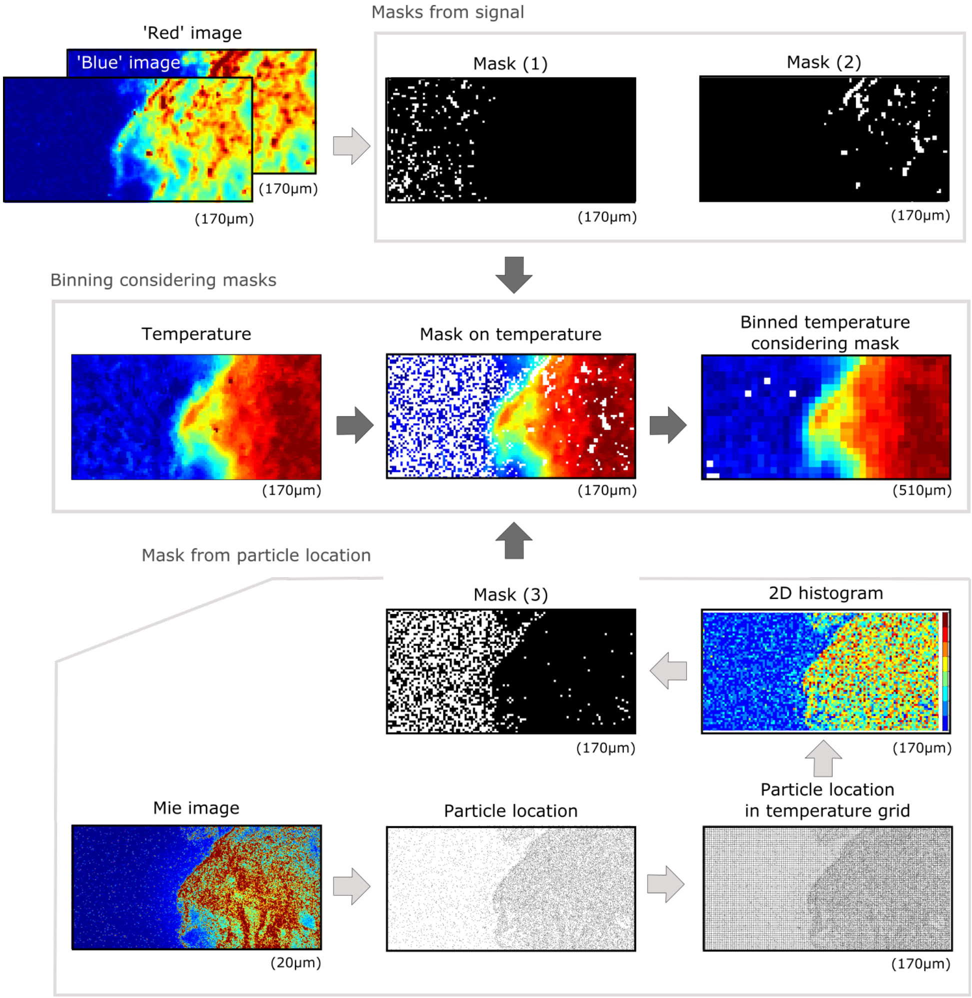

**Figure 3.10.:** Diagram of temperature calculation considering mask from particle location.

particles.

The 'true' peaks by the real particles and the 'false' peaks such as one by camera error were distinguished by applying intensity threshold. Increasing this threshold removed the peaks by the camera noise and spurious reflections, but reduced the number of identified particles at the same time. Correspondingly, for instantaneously recorded images, the phosphorescence signal integrated across the interrogation volume divided by the number of particles contained in the interrogation volume (yielding 'signal per particle') varied by varying the threshold intensity. Based on the assumption that 'signal per particle' in jet core (temperature is steady) should be constant, the suitable intensity threshold were chosen, which minimized the standard deviation of 'signal per particle'. The relative standard deviation of the 'signal per particle' decreased drastically with increasing threshold intensity and reached the minimum asymptotically around 500 counts. Therefore, 500 counts, which is less than 1% of the camera's maximum counts (65535 counts), was chosen as the intensity threshold.

An image of the identified particle location is denoted as 'Particle location' in figure 3.10. After locating the particles, the grid from the temperature field (size of 170×170

$\mu m^2$) were overlaid on the particle location image and illustrated in figure 3.10, denoted by 'Particle location in temperature grid'. The number of particles in each cell in the grid was counted (2D histogram in figure 3.10), and by applying specific number of particles as a threshold, e.g. 1, 2, a mask that recognizes the location without particle was created and illustrated as 'Mask(3)' in figure 3.10.

These masks were overlaid on the aforementioned temperature field and a 3 by 3 digital binning was applied. The values were averaged except the values from masked pixel. The final temperature field in the grid of 510 $\mu m$ size is shown in figure 3.10.

# Chapter 4.

# Investigating prospective phosphors

In this chapter, the spectra of eight prospective phosphors at various temperatures are presented. An optimized filter set was selected for each phosphor, and a resultant virtual calibration curve was calculated based on the filter set. The precision of temperature measurement considering camera error and spatial filtering were predicted for different phosphors and compared to each other. Furthermore, the effect of laser fluence on the spectra of each phosphor was investigated by adjusting the exciting laser energy. In the end, some phosphors are proposed as promising candidates for different temperature ranges.

## 4.1. Introduction

One of the attractions of phosphor thermometry is that the number of phosphors, which might be utilized as a tracer for thermographic PIV, is virtually infinite; hundreds of phosphors in various industries, such as the lamp, the X-ray, and the display, have been studied, and many of these phosphors have been applied successfully for its purpose (e.g., phosphors listed in [94]). Contrary to the vast inventory, only a few phosphors has been applied to gas thermometry, and the temperature ranges of the applied phosphors are also limited to 850 $K$ [52].

It is evident that more phosphors should be evaluated regarding required characteristics for gas thermometry purpose before an application. A similar work was done for the phosphor surface thermometry (see figure 7 of [3] and table 3,4 and figure 4 of [16]): the sensitivity of various phosphors in different temperature ranges have been assessed, and a suitable phosphor could be selected according to the temperature range of the application. However in those results, an important information for the gas thermometry application, signal intensity, is missing. In the surface temperature measurement application, the signal intensity is relatively less important than other factors (e.g., short lifetime, emission range) while in gas thermometry application, this is crucial.

As the first characteristic of ideal phosphors for gas thermometry, one can mention high emission. Different from surface measurements, in which enough number of particles are present in the measurement volume, the measurement of gas phase suffers from weak signal from low particle number densities. Therefore, high absorption coefficient and quantum efficiency are important conditions for gas temperature measurements.

Second, the lifetime of a phosphor should be short enough to resolve turbulent time scales and also to suppress the background with short gating of a camera.

Third, the spectra should shift or transform considerably according to the temperature.

As minor factors, (1) the blue emission is preferred for low black body radiation in this wavelength range, and (2) phosphor should not depend on the surrounding gas concentration, which will cause systematic errors, especially in a combustion environment. (3) Absorbing its emission is not favoured because it might lead to systematic error as shown in Section 5.2.3. (4) The spectra should not depend on laser fluence. A dependence on the laser fluence requires homogeneous beam for the measurement technique.

To evaluate phosphor according to the above mentioned criteria, an investigation from phosphor particles suspended in air is more reliable than packed powder in the oven as pointed out in [28]; a multiple scattering effect dominates optical properties in packed powder. The particles are prone to laser induced heating or even permanent damage by repetitive strong laser excitation in oven experiment. Therefore, it was proposed to characterize a phosphor from individualised particles in the air [28]. However, although all their arguments are persuasive, characterizing a phosphor from seeded particles requires considerable efforts. Obtaining a large amount of particles of each phosphor for testing might not be practical, and it is challenging to heat seeded air to high temperature with limited particle amounts. Furthermore, the expected amount of signal is questionable to measure spectra at various temperatures. By using packed powder in the oven, however, most of the issues could be overcome. Heating up stationary sample is easily realized by using an oven and the signal is strong enough to resolve the spectra at various temperatures. One can control the laser excitation and residence time at high temperature to minimize permanent change or damage. Therefore, the oven measurement is proposed to be a good approach to get a preliminary assessment from various phosphors, although they are indirect information. After screening two or three phosphors, however, a detailed analysis on individualized particles in gas as proposed in [28] should follow.

**Investigated phosphors** As promising candidates for the tracer of thermographic PIV, some of the thermographic phosphors are selected, which have already been utilized in surface measurement applications. High sensitivity was expected from these phosphors.

The list of phosphors from the lamp industry, in which the exhaustive research has been performed to develop efficient and reliable phosphors, might include some promising phosphors for gas thermometry. Among lamp phosphors, UV LED phosphors, which converts near UV emission of GaN chip (350-420 $nm$) to the desired wavelength, were investigated. If one can use 400 $nm$ excitation for both Mie-scattering and phosphorescence of UV LED phosphors, the experimental setup might be further simplified. The investigated phosphors in this study are listed in table 4.1.

## 4.2. Results and discussions

The spectra of phosphors listed in table 4.1 at various temperatures were measured with the experimental setup explained in Section 3.1. The recorded images were reduced to spectra by the algorithm described in the same Section. Among the above mentioned three major characteristics, signal intensity and temperature sensitivity of each phosphor were evaluated by the spectra in varying temperature. This study relied on the literature for the lifetime, but it should be measured directly in the near future as will be explained

**Table 4.1.:** Investigated phosphors.

| *Notation* | *Host* | *Dopant* | *Lifetime* | *Particle diameter* | *Excitation[nm]* | *Camera exposure* | *Group* | *Manufacturer Part no* |
|---|---|---|---|---|---|---|---|---|
| BAM | $BaMgAl_{10}O_{17}$ | $Eu^{2+}$ | 2 $\mu s$ [78] | 2.6 $\mu m$ | 355 | 40 $\mu s$ | TP, B | PT, KEMF63/UF-P2 |
| SRMG | $(Sr,Mg)_2SiO_4$ | $Eu^{2+}$ | 0.5 $\mu s$ [78] | 7.0 $\mu m$ | 355 | 30 $\mu s$ | LP, B | PT, HEBK63/N-D1 |
| LSP:EuTb | $LiSrPO_4$ | $Eu^{2+}$, $Tb^{3+}$ | 30 ms [17] | - | 355 | 20 $ms$ | LP, C | Chem. TUD, - |
| BAM:EuMn | $BaMg_2Al_{16}O_{27}$ | $Eu^{2+}$, $Mn^{2+}$ | 3.5 ms [59] | 3.5 $\mu m$ | 355 | 20 $ms$ | LP, C | PT, KEMF63M/F-U1 |
| YAG:Dy | $Y_3Al_5O_{12}$ | $Dy^{3+}$ | 1 ms [80] | - | 355 | 30 $ms$ | TP, L | STS, - |
| GdO | $Gd_2O_2S$ | $Eu^{3+}$ |  | 4.0 $\mu m$ | 355 | 100 $\mu s$ | LP, L | PT, UKL63/F-U1 |
| YAG:Pr | $Y_3Al_5O_{12}$ | $Pr^{3+}$ | 190 $\mu s$ [47] | 1.8 $\mu m$ | 266 | 400 $\mu s$ | TP, L | PT, QML59/FF-X |
| YAG:Tb | $Y_3Al_5O_{12}$ | $Tb^{3+}$ | 30 ms | - | 266 | 800 $\mu s$ | TP, L | Chem. TUD, - |

*Dopant*: LSP:EuTb, both 5 %; YAG:Tb, 7.2 %; doping concentrations of commercial phosphors are not disclosed to customers; *Group*: TP, thermographic phosphor; LP, LED phosphor; B, Broad emission; C, Energy transfer in co-doped phosphor; L, Line emission; *Manufacturer*: PT, Phosphor Technology; Chem. TUD, Chemistry department of TU Darmstadt; STS, Southside Thermal Sciences;

later. Among minor factors, the influence of laser fluence on spectra will be followed with spectra in varying laser fluence.

## 4.2.1. Spectra with varying temperature

### Overall signal intensity comparison

First of all, the brief comparison of the signal intensity of investigated phosphors was possible by integrating each spectrum in the whole emission wavelength range. As mentioned above, the signal intesity is one of the most important characteristics of phosphor for gas thermometry. The comparison of broadband emission and codoped phosphors is shown in figure 4.1, and the line-emission phosphors are shown in figure 4.2. Be aware that the intensity scale of figure 4.1 is an order of magnitude larger than the one in figure 4.2.

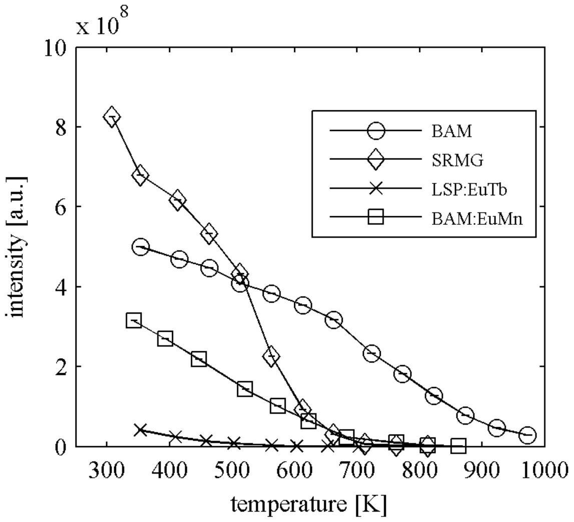

**Figure 4.1.:** Overall signal comparison of broad emission and codoped phosphors.

**Table 4.2.:** Overall comparison of intensities. $I_{350}$: relative signal at 350K to BAM:Eu. $T_{50}$: temperature at which the signal becomes half of the signal at 350 $K$.

| *Phosphor* | $I_{350K}$[a.u.] | $T_{50}$ *[K]* |
|---|---|---|
| BAM | 1.000 | 712 |
| SRMG | 1.361 | 535 |
| LSP:EuTb | 0.082 | 425 |
| BAM:EuMn | 0.612 | 512 |
| YAG:Dy | 0.159 | 877 |
| GdO | 0.015 | 440 |
| YAG:Pr | 0.015 | 612 |
| YAG:Tb | 0.179 | 481 |

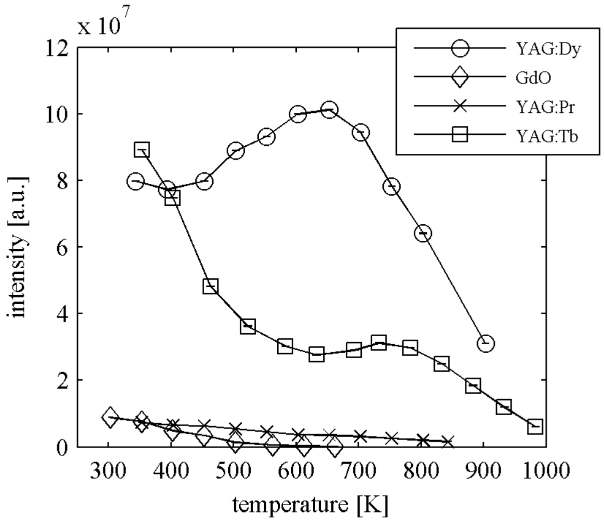

**Figure 4.2.:** Overall signal comparison of line-emission phosphors.

From these results, the $I_{350}$ signal level, that was the relative signal at temperature 350 $K$ to BAM and the $T_{50}$ temperature, in which the signal becomes half of the signal in the room temperature, were extracted and summarized in table 4.2. Among the phosphors, BAM, SRMG, BAM:EuMn and YAG:Dy and YAG:Tb have comparable intensities.

### Detail analysis on spectra and filter sets

Based on the spectra, the investigated phosphors were split into three categories according to their emission type; (1) broadband emission, (2) line-emission and (3) energy transfer in co-doped phosphors. As explained in Section 2.1.2, different mechanisms induced spectra change according to the temperature in the categories and the theory is repeated briefly here. In the following figures, the convolution of the transmissions of a selected filter set and the quantum efficiency of the CCD camera is shown together with measured spectra for each phosphor. The filter set was selected through an optimization process as the BAM (see figure 3.7). Some of plausible filter sets from inventories of filter manufacturers (Chroma Technology, Semrock) were chosen to use thermal behaviour of each phosphor according to its category. Some of the filter sets were generated by CWL and FWHM in 90 % transmission. However, it is likely to be customized without difficulty. After that, by equation 3.1 and 3.2, a filter set, which gave the best temperature precision, was chosen for the phosphor. The detail of each optimization will not be explained, but the compared filter sets will be specified for each phosphor.

**Broadband emission phosphor** Shifts of spectra and broadening were observed in broadband emitting phosphor, BAM and SRMG in this study as shown in figure 4.3 and 4.4. The emission of divalent Eu ion occurs by the transition $5d \rightarrow 4f$, which is strongly coupled to crystal field. With increasing temperature the average distance between the lattice ligands and the activator ions increases by thermal expansion and, therefore, the crystal field is weakened. The weakened crystal field increases the energy levels in the activator and results in the frequency shift to higher energy. Meanwhile, the high vibrational states are occupied in high temperature and lead to the broadening of emission spectra. For broad emission phosphors, one can use a spectral region where strong broadening occurs as one channel, and the other spectra region where relatively free from temperature change as the other channel.

For BAM shown in figure 4.3, one can observe that the 445 $nm$ peak shifts towards UV regime with broadening as also listed in table 4.3. The optimized filter set of 400-40 and 470-40 were selected as blue and red channels as discussed in Section 3.2.2.

For SRMG, the peak was around 460 $nm$, and impressive broadening, which was stronger than BAM was observed; the FWHM of SRMG was broadened 1.6 times in temperature range from 350 $K$ to 810 $K$ while the FWHM of BAM 1.2 times (see table 4.3). Furthermore, it has a higher intensity than BAM until 550 $K$ although rapidly quenched after that (see figure 4.1). Therefore, by using the both rising tails of the spectra with temperature, high temperature sensitivity could be attained, hence high precision was expected in an intermediate temperature range. A multi-band interference filter (Semrock, FF01-416/501-25) was chosen for the blue channel (415-30, 503-25), and a single-band interference filter (Semrock, FF01-460/14-25) was chosen for the red channel ranging 511-20.

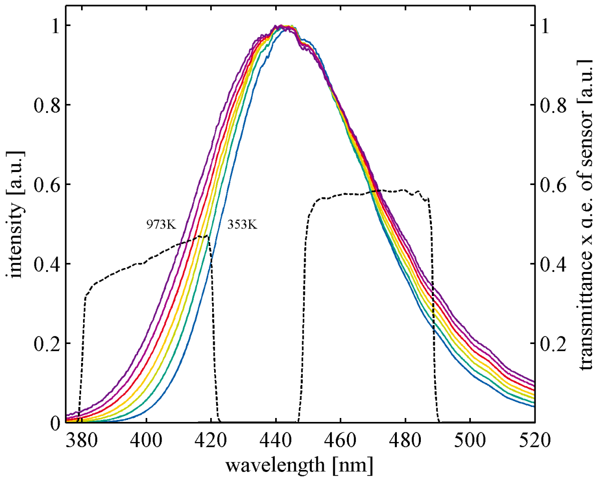

**Figure 4.3.:** Normalized spectra of BAM at different temperatures with selected filter set(400-40/470-40). See caption of figure 3.7 for compared filter sets. Temperature range 353, 463, 563, 663, 773, 873, 973 $K$ in order.

**Energy transfer in co-doped phosphor** The energy transfer from sensitizer to the activator diminishes at high temperature. By using activator peak as red channel and sensitizer peak as blue channel, the intensity ratio increased strongly with the temperature.

BAM:EuMn has been widely used for PDP panel and UV LED phosphor because it can absorb the light to around 420 $nm$ and emit green light efficiently [59, 93]. BAM:EuMn emitted strong emission at room temperature, but quenched fast at high temperature

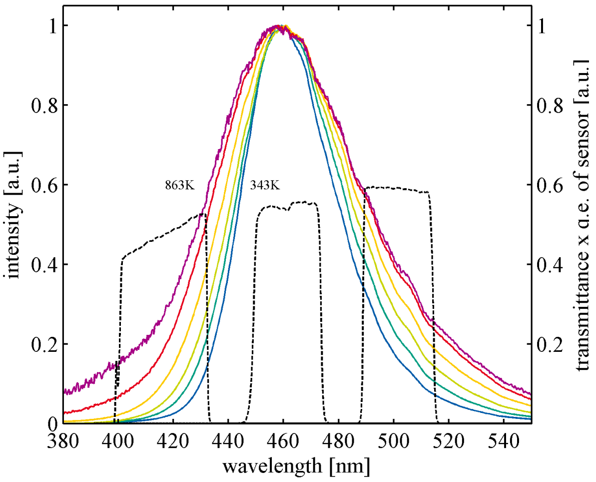

**Figure 4.4.:** Normalized spectra of SRMG at different temperatures with selected filter set(415-30, 503-25/460-14). Compared filter set 1: 400-40/470-40, filter set 2: 435-20,498-20/460-14; filter set 3: 400-50/460-14. Temperature ranges 308, 413, 513, 613, 713, 813 $K$.

(see figure 4.1). The energy transfer from $Eu^{2+}$ to $Mn^{2+}$ decreased at high temperature; therefore, the sensitizer peak increased at high temperature (see figure 4.5). This is also shown in LSP:EuTb in figure 4.6. By using 513 $nm$ $Mn^{2+}$ peak as red channel and 452 $nm$ $Eu^{2+}$ peak as blue channel, one can expect strong temperature sensitivity. For LSP, one can use the 539 $nm$ $Tb^{3+}$ peak as red channel and the broad 465 $nm$ $Eu^{2+}$ peak for blue channel.

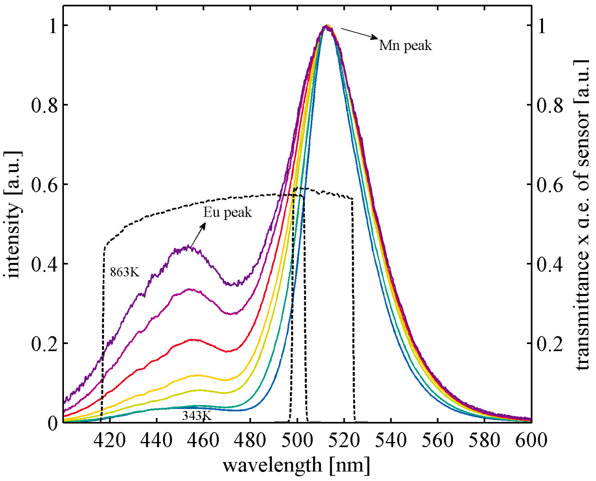

**Figure 4.5.:** Normalized spectra of BAM:Eu,Mn at different temperatures with selected filter set (460-80/511-20). Compared filter set 1: 460-80/513-7; filter set 2: 480-40/513-17; filter set 3: 480-40/511-20. Temperature ranges 343, 447, 573, 623, 684, 813, 863 $K$.

**Table 4.3.:** Peak and FWHM variation of BAM and SRMG

| $BaMgAl_{10}O_{17} : Eu^{2+}$ | | | $(Sr, Mg)_2SiO_4 : Eu^{2+}$ | | |
|---|---|---|---|---|---|
| T $[K]$ | Peak $[nm]$ | FWHM $[nm]$ | T $[K]$ | Peak $[nm]$ | FWHM $[nm]$ |
| 353 | 445.5 | 50.0 | 308 | 459.2 | 39.3 |
| 415 | 444.3 | 51.7 | 353 | 459.2 | 40.8 |
| 463 | 444.3 | 52.6 | 413 | 460.8 | 43.5 |
| 513 | 442.3 | 54.1 | 463 | 460.8 | 46.2 |
| 563 | 442.0 | 55.1 | 513 | 460.8 | 48.2 |
| 613 | 441.7 | 56.1 | 563 | 460.8 | 52.1 |
| 663 | 441.7 | 57.1 | 613 | 460.8 | 55.2 |
| 723 | 441.7 | 58.8 | 663 | 458.8 | 58.6 |
| 773 | 441.7 | 59.8 | 713 | 457.5 | 61.7 |
| 823 | 441.4 | 60.7 | 763 | 457.5 | 65.6 |
| 873 | 441.4 | 62.0 | 813 | 456.9 | 65 |
| 923 | 441.4 | 63.7 | | | |
| 973 | 440.4 | 64.9 | | | |

**Line emission phosphor** In line-emission phosphors, the intensity ratio of the peaks can vary; the portion of longer or shorter wavelength emission can increase according to the gaps between the energy levels. The emission arises from a transition between well-shielded orbitals ($4f \rightarrow 4f$), thus, relatively free from crystal field and have small Stokes shift. Most of them are a forbidden transitions, therefore, have relatively long lifetime around an order of 1-10 $ms$ at room temperature. When the effect of increasing multi-phonon emission rate at high temperature prevails, the high energy states are quenched

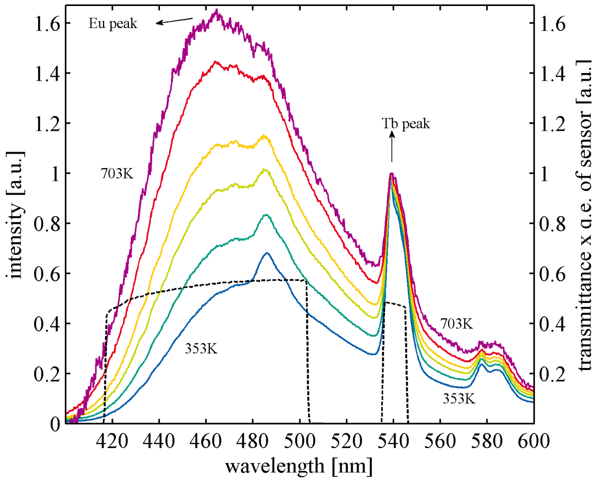

**Figure 4.6.:** Normalized spectra of LSP:Eu,Tb at different temperatures with selected filer set (460-80/540-10). Compared filter set 1: 480-40/540-10; filter set 2: 460-80/511-20; filter set 3: 480-40/511-20. Temperature ranges 353, 409, 458, 503, 563, 703 $K$.

and the emission from there decreases. As a contrary, when the energy gap is close enough, the higher energy states are populated by thermal pumping, thus, emission from there increases. By using the emissions at different wavelengths, line-emission phosphors could be used for two color ratio method.

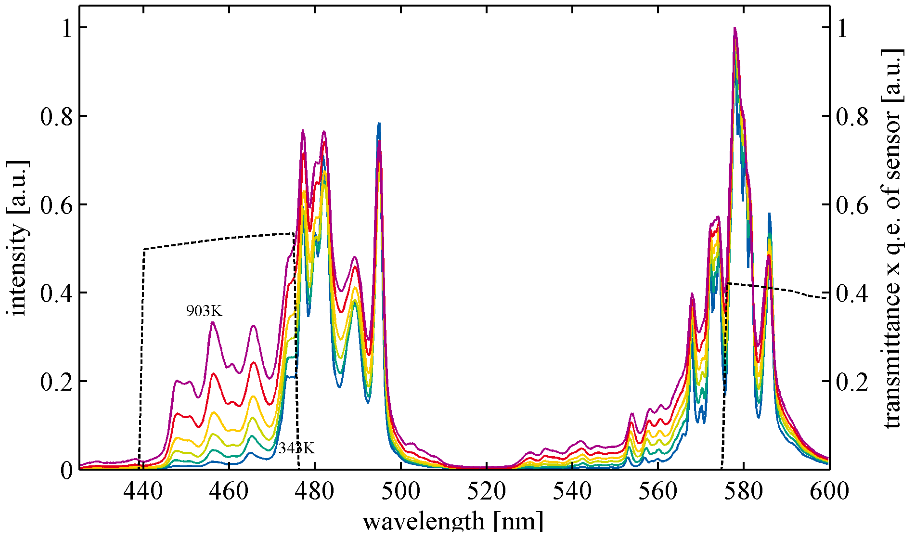

**Figure 4.7.:** Normalized spectra of YAG:Dy at 578 *nm* peak at different temperatures with selected filter set (460-30/585-30). Compared filter set 1 [35, 52]: 450-10/495-10; filter set 2 [45]: 460-30/485-30; filter set 3: 470-40/585-30. Temperature ranges 343, 453, 553, 653, 753, 903 *K*.

YAG:Dy has experienced a great interest in an application to surface temperature measurement in combustion environment in many studies [25, 42, 79, 80]. The spectra of YAG:Dy particles, which were seeded into methane flame, did not change after experiencing the flame [96]. By using the 467 *nm* and 496 *nm* peaks, the intensity ratio is sensitive from 300 *K* to 1700 *K* [34]. As shown in figure 4.7, the peaks around 467 *nm* increased at high temperature by thermal pumping, while the 496 *nm* peak was relatively stable. In gas temperature measurements, Hasegawa et al. [35] and Lawrence et al. [52] used the phosphor with the same color channels for surface temperature measurements. However, as Lawrence reported [52], the signal was too weak for the gas temperature measurement with these wavelength ranges. After that Jovicic et al. [45] used color bands 440 - 475 *nm* for blue channel and 475 - 500 *nm* for red channel to have more signal. They could measure instant temperature fields, but the measurement quality was not comparable with measurements with BAM [2, 29] or YAG:Pr particles [75]. Although most of the study did not use the wavelength range 550-600 *nm*, it showed substantial emission in this study. The range of 575 - 600 *nm* was relatively independent on the temperature and could be used for the red channel as illustrated in figure 4.7.

GdO is a famous UV LED phosphor [90]. However, in the investigated temperature range, it showed little temperature sensitivity as shown in figure 4.8. Therefore, no filter was selected and it was not considered any further.

As GdO, the normalized spectra at 545 *nm* peak of YAG:Tb presented in figure 4.9 indicated negligible sensitivity in the studied temperature range here and it was not

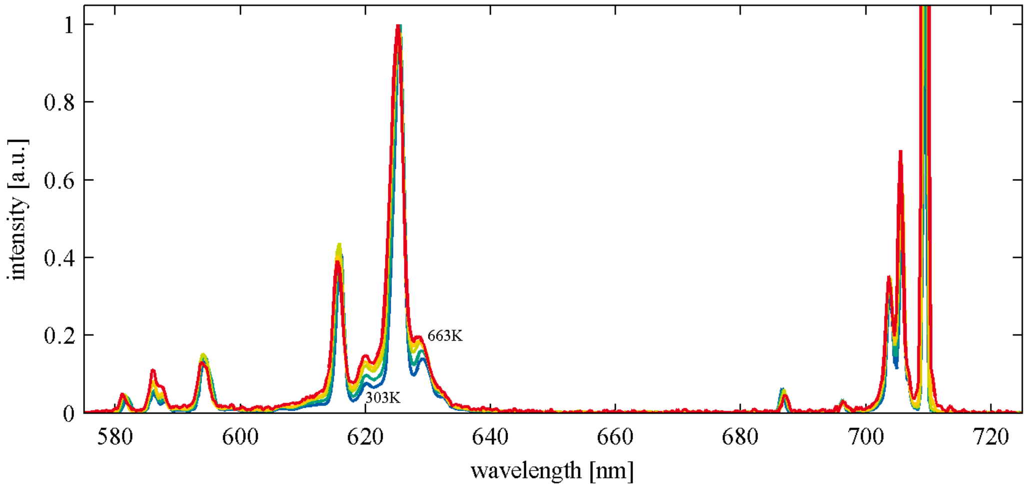

**Figure 4.8.:** Normalized spectra of GdO at 625 *nm* peak at different temperatures. Temperature ranges 303, 403, 503, 613, 663 *K*.

considered further.

The YAG:Pr phosphor has been used in [44, 64]. They used the 435 - 526 *nm* region for the blue channel and the 600 - 630 *nm* region for the red channel, as illustrated in figure 4.10. When normalized with the 615 *nm* peak, the 489 *nm* peak decreases rapidly with the temperature by increasing non-radiative emission rate. However, as well known, the 489 *nm* peak will increase again after 1100 *K* by the population of a high energy state by thermal pumping [44], although this study did not reach the temperature. Overall, the broadening of spectra was observed.

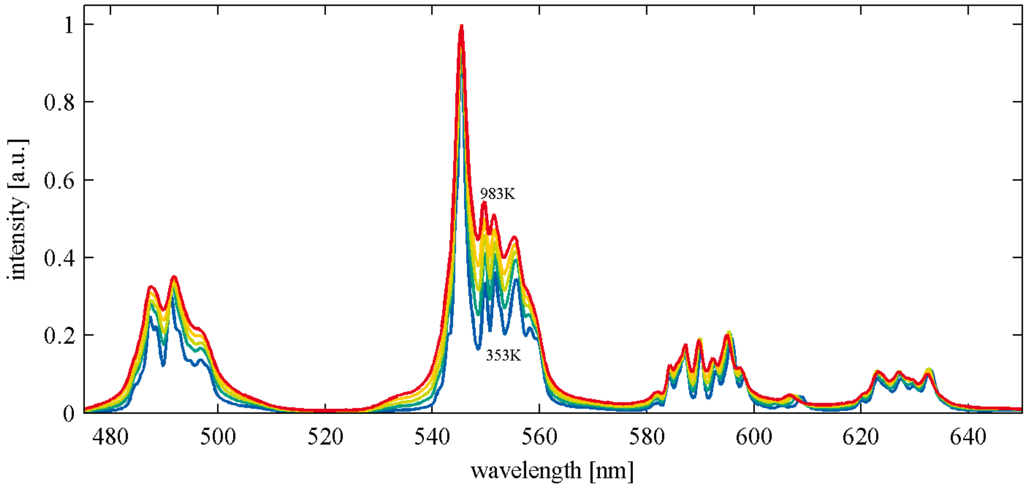

**Figure 4.9.:** Normalized spectra of YAG:Tb at different temperatures. Temperature ranges 353, 523, 693, 833, 983 *K* in order.

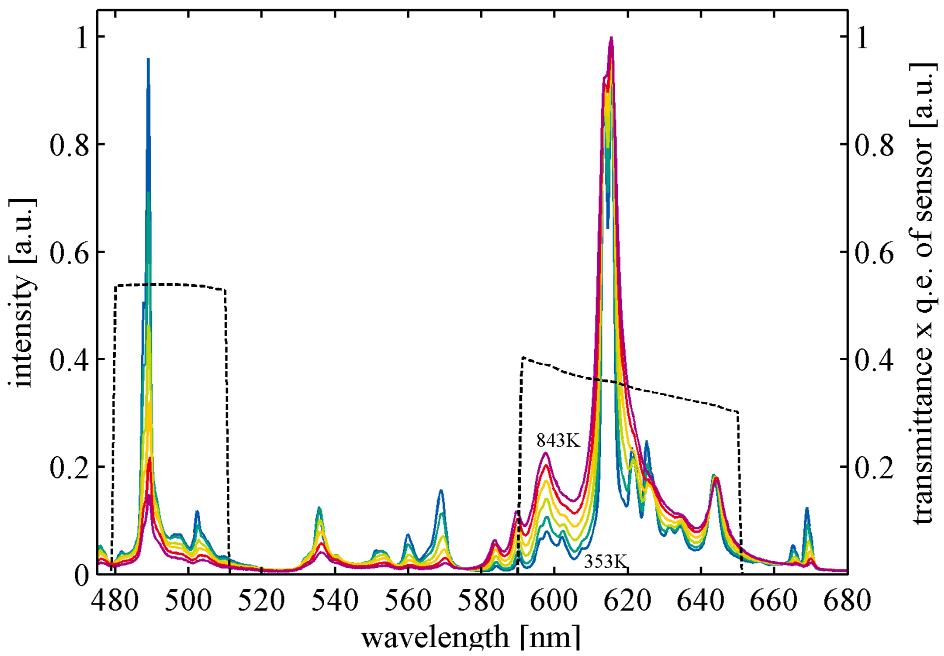

**Figure 4.10.:** Normalized spectra of YAG:Pr at different temperatures with selected filter set (620-60/495-30). No filter set was compared for this phosphor, but the filter set used in [44] was adopted. Temperature ranges 353, 453, 553, 653, 753, 843 $K$.

Although some of line-emission phosphors indicated little temperature sensitivity, by using different delay between channels, the sensitivity could be improved as shown in [64, 86, 95]; the lifetime of each peak behaves differently when increasing temperature. Therefore, they delayed one of the cameras and used different lifetime variation in the respective emission line. The temperature sensitivity of intensity ratio could be attained in the expense of the signal strength. The phosphorescence can be spectrally and temporally resolved by using a high speed spectrometer system [23] and this information could be used to simulate improved temperature precision by time delay and design phosphor thermometry.

### Virtual calibration curve

With the measured spectra and given filter set, the virtual calibration curve was attained by equation 3.2. The results are shown in figure 4.11 and from the slope of the curves of each phosphor, one can conjecture the sensitivity of intensity ratio on the temperature.

### Temperature precision

The temperature precision was selected as the primary value to evaluate a phosphor because the temperature sensitivity and the signal intensity are reflected ultimately to the temperature precision. As shown in equation 3.1, the information of $\frac{dT}{dr}$, $r$, and $\Sigma_A$ are necessary to predict the temperature precision of a phosphor when it is applied to the gas thermometry. At a certain temperature, one can obtain $\frac{dT}{dr}$ and $r$ from measured

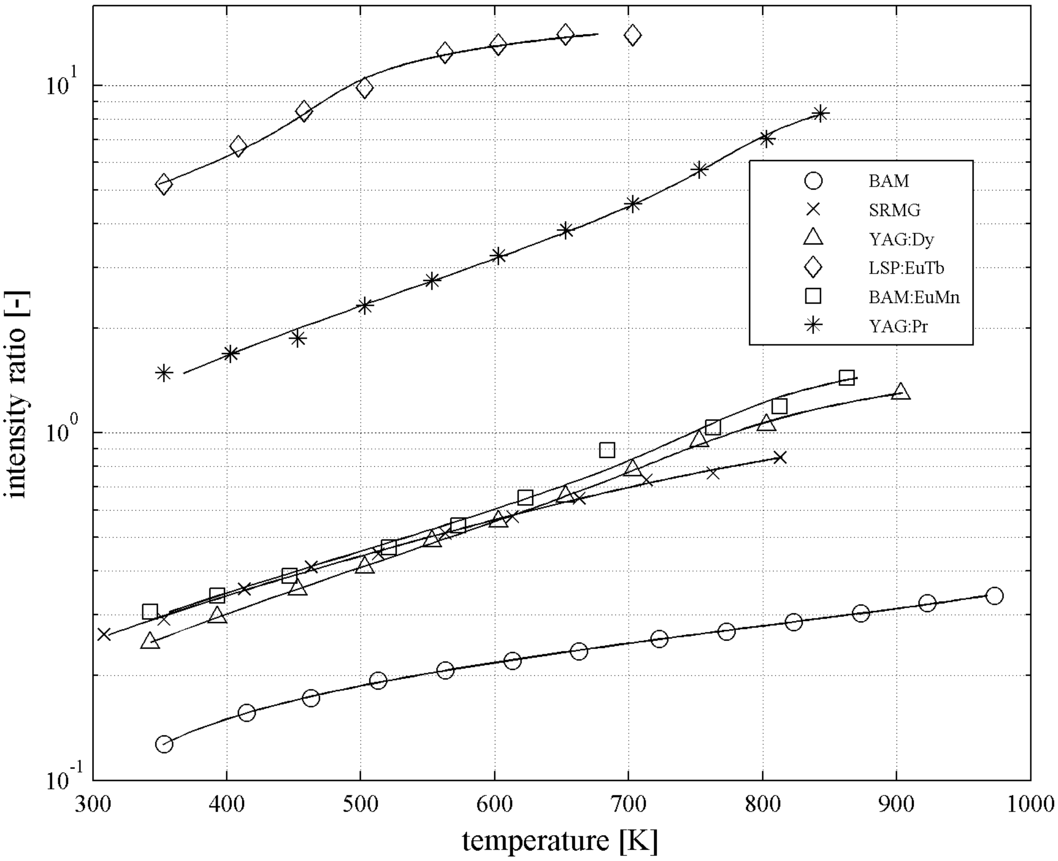

**Figure 4.11.:** Simulated calibration curves with given filter sets.

spectra as shown in figure 4.11, and the expected signal of a certain phosphor seeded in the flow at given temperature, $I_A$ was obtained by adding one more assumption to the equation 3.4.

In equation 3.4, if it is assumed that the relative intensity of a phosphor to reference phosphor BAM from seeded particles to be the same with the one from packed powder, the equation could be expanded to other phosphor particles.

$$\Sigma_A = \Sigma_{A,ref} \times \frac{\int_0^\infty \Gamma(\lambda, T, TGP)\xi_A(\lambda)d\lambda}{\int_0^\infty \Gamma(\lambda, T_{ref}, TGP_{ref})\xi_{A,ref}(\lambda)d\lambda}, \tag{4.1}$$

here, TGP means various phosphors.

By using the reference value from measurement of seeded BAM particles, the expected signal of various phosphors at various temperature were conjectured. According to the equation 3.1, the precision of temperature measurement was calculated and it is shown in figure 4.12. In the model for this prediction, only camera errors and spatial filtering such as median filter are considered. In actual measurements, additional error such as background will deteriorate the precision. In the intermediate temperature range (300 - 500 $K$), the SRMG and BAM:EuMn were very promising. However, for thermal quenching, the precision of SRMG deteriorates rapidly after 500 $K$. BAM:EuMn showed worse precision than SRMG in the temperature range lower than 500 $K$, but better after 600 $K$. However, the precision of this phosphor was deteriorated suddenly after 600 $K$. BAM demonstrated proper performance in a wide temperature range from room temperature to relatively higher temperature around 800 $K$ than other phosphors. YAG:Dy revealed poor precision at low temperature because the signal in blue channel at low temperature was very weak. However, around 700 $K$ it showed the best precision.

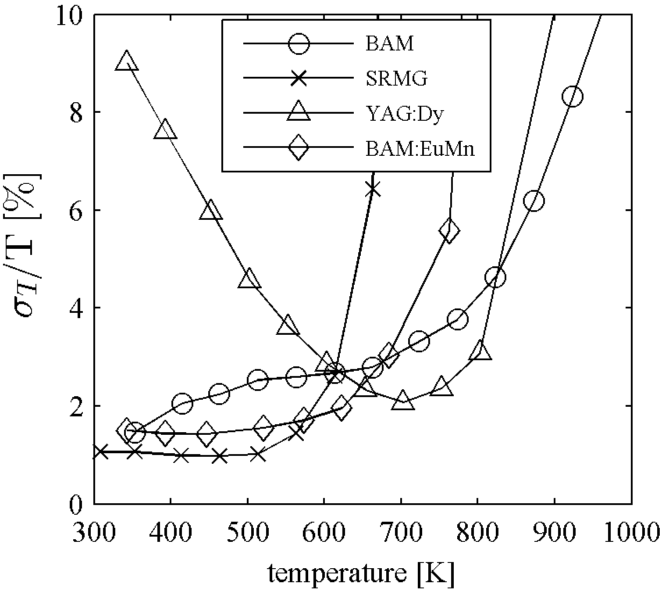

**Figure 4.12.:** Estimated temperature precision according to error propagation.

## 4.2.2. Spectra with varying laser fluence

The laser fluence effect on the spectra was investigated by adjusting exciting laser energy. As it will be explained in Section 5.2.2, the dependency on laser fluence necessitated the measurement technique to prepare a homogeneous beam. The spectra at various laser fluence of the investigated phosphors are illustrated in figure 4.13.

Generally speaking, the laser fluence dependence exhibited different aspects according to the type of emission; the broadband emission phosphors exhibited slight shift to UV regime. In co-doped phosphors, the sensitizer peak decreased with increasing laser fluence possibly for accelerated energy transfer between sensitizer and activator. The line-emission phosphors manifested little dependence on fluence. More detailed analysis on the laser fluence effect will be present in Section 5.2.2 with the spectra of BAM. Investigation of laser fluence effect on aerosolised particles is also presented there. Here in figure 4.13, one can roughly compare the degree of the dependence compared to BAM and anticipate its laser fluence dependency.

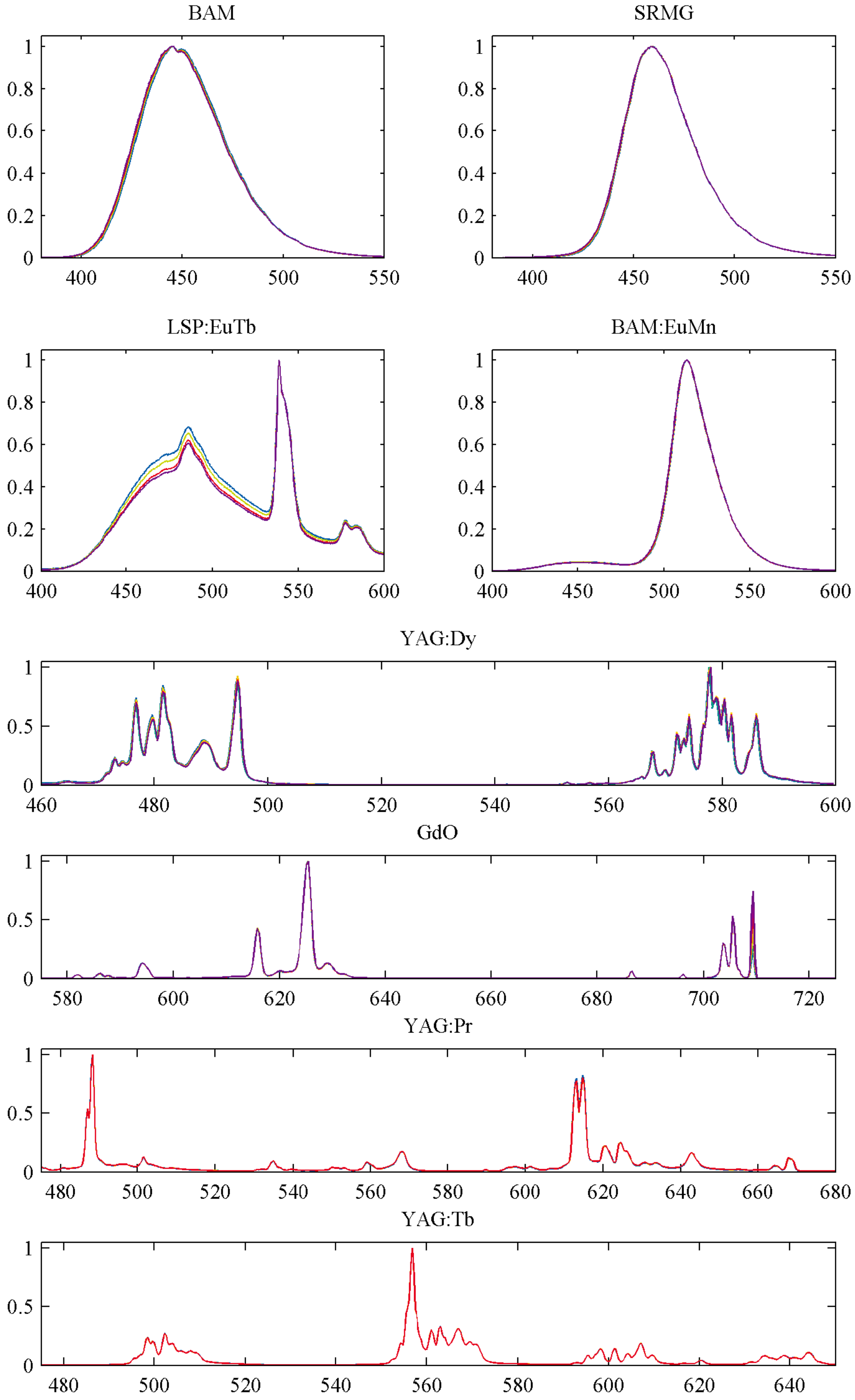

**Figure 4.13.:** Normalized spectra of phosphors at varying laser fluence.

### 4.2.3. Limitation of characterizing phosphor in oven

As outlined in the introduction to this chapter, the interpretation based on the spectra from packed powder is not sufficient for applying to the tendency of seeded particles in the air. One of the evidence was that the virtual calibration curve based on spectra measurement from packed powder in the oven was inconsistent with the measured calibration curve from seeded particles in the air as shown in figure 4.14. Although a little difference between the laser fluence used for two measurements existed, the excessive gap, especially at high temperature, could not be attributed to the laser fluence difference only. The discrepancy between the virtual and measured calibration curves was also reported by [45]. For the multiple scattering in packed powder and possible physical damage of phosphor in the oven, special care is required to transfer the information to the seeded particles.

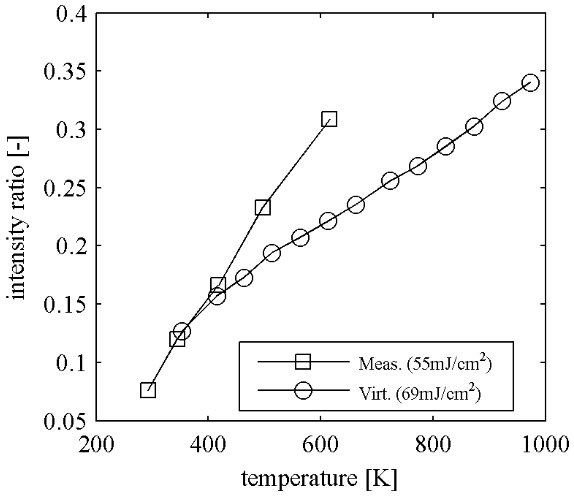

**Figure 4.14.:** Comparison of measured calibration curve from seeded particle and virtual calibration curve from spectra.

## 4.3. Conclusion

Characterization with the oven was appropriate to distinguish prospective phosphors from non-promising ones; the signal intensity and the temperature sensitivity could be reasonably estimated, although the discrepancy between packed powder and the individualized particles existed obviously. By surveying the list comprised of a virtually infinite number of phosphors and characterizing them in the oven, phosphors suitable for various temperature range shall be found. In this study, following phosphors are nominated for further investigation.

BAM:EuMn and SRMG could be suitable phosphors in the temperature range of 300 - 500 $K$ for their strong emission. Especially, if their emissions by the excitation of UV LED light source (around 400 $nm$ or longer excitation) are similar with the one by 355 $nm$ excitation (e.g., absorption cross-section, quantum efficiency, emission spectra), the experimental setup could be further simplified, e.g., using one double cavity UV LED for

Mie scattering and phosphorescence excitation or high speed LED source for simultaneous high speed PIV and temperature measurements. At present, the UV light to excite the phosphor particle, 266 *nm* or 355 *nm* lights are difficult to be used for PIV for the low transmittance of camera objective in the wavelength range and quantum efficiency of the detector. 400 *nm* or longer wavelength light is more promising for the Mie-scattering detection. YAG:Dy indicated worse capability at low temperature, but it showed highest $T_{50}$, which indicate the possibility as high temperature phosphor. Although its absolute emission intensity is relatively weak, the chance to be applied to high temperature measurements remains, if one can increase the intensity by adjusting its host [51] or using a different shape, e.g., hollow particles; in [51], they substituted the tetrahedral sites in YAG with $B^{3+}$ and $N^{3-}$ and tuned the host. Because the phosphorescence is influenced by the host, stronger signal and delayed thermal quenching around 100 $K$ of YABNG:Dy than YAG:Dy has been reported. In this study, to investigate the turbulent flux in jet with co-flow configuration, BAM was selected for its high precision in the temperature range of interest.

# Chapter 5.

# Measurement uncertainties

Due to the components of uncertainties arising from the random and the systematic effect[1], a measurement is only an approximation of the quantity to which the measurement is subject to. Therefore, a quantification on the measurement uncertainty is necessary for the result to be complete [87]. In this chapter, the effects of uncertainty components in the temperature measurement such as camera noise, spatial filtering, laser fluence, seeding density, are analysed partly theoretically, and partly statistically based on the measurement data. Through this analysis, the performance of this measurement technique can be estimated. The analysis is separated into two parts, the precision and the accuracy.

## 5.1. Precision analysis

The precision means how close the repeated measurements locate each other. Typically, the standard deviation of the measurements represents the precision and expresses itself as $q \pm \sigma_q$. Here, $q$ denotes measurement quantity and $\sigma_q$ the standard deviation. The relative standard deviation, $\sigma_q/q$ is also a widely used term. The smaller a standard deviation is, the better precision we get.

A theoretical model that includes the effect of camera error and spatial filtering was introduced in equation 3.1 and will be applied to the measured data. The impact of residual misalignment after the image registration and different smoothing schemes will be assessed. Lastly, the precision of this study will be expressed statistically.

**Comparison of theoretical model with measurement** The model, equation 3.1 was applied to the measured data. The experimental set-up was the same with the one in Section 3.2. The data were sampled from 673 shots in the jet center at the x=1.5d position (sampled area 20 by 20 pixels), when the jet reached steady state temperature of 530 $K$. The sampled temperatures were conditioned according to the signal intensity in the red channel (bin size of 50 counts), and then the standard deviations of the samples were calculated. The relative standard deviation, $\sigma_T/T$ are denoted by symbols in figure 5.1.

To calculate the $\sigma_T$ from the model, $\frac{dT}{dr}r$ at 530 $K$ was obtained from measured calibration curve and $K = 0.25$ from the specification of the camera, $N_{cam} = 1.5$ measured experimentally for 4 by 4 hardware binned camera as explained previously, $N_{ker} = 25$

---

[1] The random effect usually influences a precision of the measurement, and the systematic effect influences an accuracy, but not necessarily.

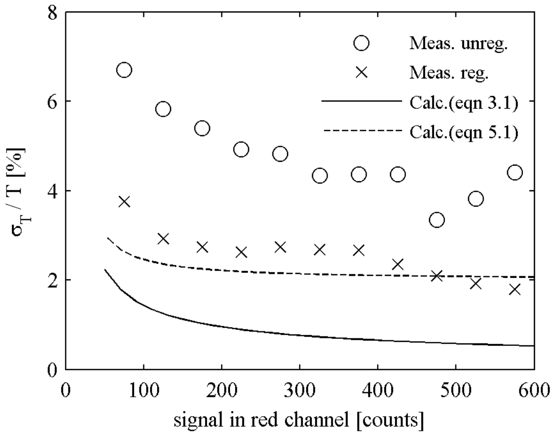

**Figure 5.1.:** The effect of camera error and the image registration on the uncertainty of temperature measurement. Calc.(eqn 3.1) denotes the calculation based on the equation 3.1, and Calc.(eqn 5.1) equation 5.1. For calculation the values $K = 0.25$, $N_{cam} = 1.5$, $N_{ker} = 25$, $T = 530K$, $r = 0.264$ have been used and a constant 2 % error has been used for Calc.(eqn 5.1). 'Meas. unreg.' denotes measurement data before image registration and 'Meas. reg.' after. Read the text for detailed explanation. The sample was acquired from 20 × 20 pixels in jet center at the x=1.5d axial position in 673 shots. The sample was binned with 50 counts and the standard deviation was calculated for each signal level.

according to used filter size, have been used, and the calculated relative error in % is shown in figure 5.1 denoted by solid line. By comparing the measurement data and the calculation in figure 5.1 (denoted by the cross and the solid line), one can observe as also found in [28] that (1) the theoretical model catch the trend well but with a constant difference and (2) the camera error was significant in temperature uncertainty (about 50%). Here, one should keep in mind that the fluctuations from the turbulence exist in the measurement because in this study a long pipe was used to generate the heated jet. Generally it has a certain degree of turbulence intensity at the jet center (see figure 6.9). By assuming no correlation between the camera error and the fluctuations by turbulence, the measured rms of the temperature, $\sigma_{m,T}$ is

$$\sigma_{m,T} = \sqrt{\sigma_T^2 + \sigma_{t,T}^2} \tag{5.1}$$

here, $\sigma_{t,T}^2$ is the variance by turbulence. Accordingly, by assuming a constant 2% error from the turbulent fluctuation, the estimation of measured rms of temperature, $\sigma_{m,T}$ was graphed as dashed line. As pointed out by [28], the remained constant difference between the theoretical model and the measurement especially in low signal range (compare dashed line and crosses) could come from unknown errors, which may include misalignment between two cameras, or different laser fluence or/and seeding density effects to be explained in the accuracy part.

Figure 5.1 also indicates the importance of image registration. Both symbols in figure 5.1 are after the image registration with the algorithm in Davis 8.2. In most of the cases, after the image registration algorithm, subpixel image registration is obtained. However, when a misalignment between calibration target and the laser sheet is presented, disparity between two images may exist. The algorithm in Matlab applied (1.21, 0.49) pixel shift and 0.035° rotation only to the measurement denoted by crosses in figure 5.1. See Section 3.2.3 regarding both image registration. The division provided the ratio and the 5 by 5 moving average filter were followed. From figure 5.1, one can clearly observe that the image registration played a considerable role in temperature uncertainty. This effect is accentuated in the low signal regime, in which the seeding density was low and matching both image became more important. Similar findings were reported in [28].

Furthermore, the effect of spatial filter was assessed. The spatial filter, such as moving average or median filter, decreases the random effect and improves the precision with the expense of the spatial resolution. The precision improvement by the different spatial filter was examined by applying each filter to the same measurement data. The filter were implemented to the whole image and then the sampling was applied to 20 by 20 pixels in the jet core. Standard deviations were calculated from each sample of different cases. As shown in figure 5.2, the temperature uncertainty decreases dramatically with increasing kernel size. However, it did not improve as much as the theoretical model, equation 3.1 (compare dashed line and symbols in figure 5.2). The moving average and the median filters did not show a significant difference in precision.

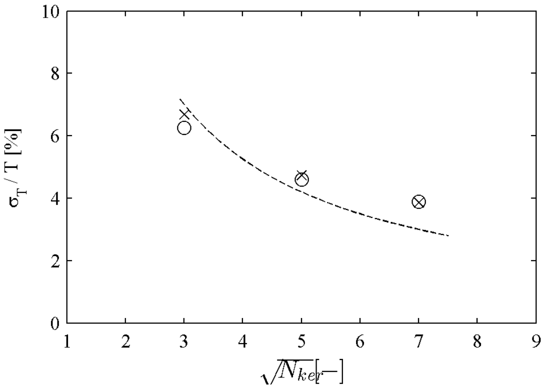

**Figure 5.2.:** Temperature precision improvement by a different spatial filter. Circles denote moving average filter and the crosses median filter. The dotted line is a fitting of equation, $c/\sqrt{N_{ker}}$. $c$ is an arbitrary constant.

**Current status of precision** The precision of the temperature measurement in Section 6.1 was assessed statistically. As explained in the above analysis, the precision depends on the camera error, signal strengths, the temperature sensitivity, and the size of the spatial filter. The range of the two color bands determined the temperature sensitivity and influenced the signal strength of each channel. The size of the spatial filter was limited by required spatial resolution according to the phenomena to be examined.

The temperature precision of this study, which is constrained by the restrictions mentioned above, is statistically evaluated. The measurements in single pixels in the jet core ($x = 0.7d$ above the jet exit, $3.06 \times 2.55 mm^2$ area, $6 \times 5$ pixels) were sampled at different temperatures. The total sample size varied at different temperature because the seeding density fluctuated and only the images with suitable seeding density were selected. The probability density function of each sample was drawn in figure 5.3. The mean, the standard deviation, the relative standard deviations, and the numbers of samples are written in the figure 5.3.

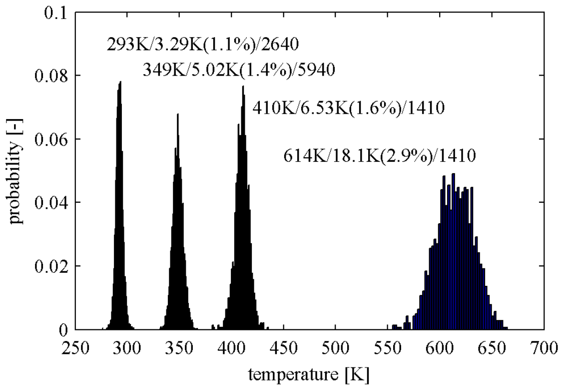

**Figure 5.3.:** Precision of the temperature measurement. The quantity in each bin is divided by total quantity to produce probability density function. Notation denotes mean/standard deviation(relative standard deviation)/number of samples

## 5.2. Accuracy analysis

The accuracy means how close the estimated value from repeated measurements to the true value is. A systematic error existing in the measurement will bias the expected value always in the same direction and amount from the true value [8]. Therefore, the systematic errors should be identified.

For an application to phosphor surface thermometry, Brübach et al.[16] have identified six categories of systematic errors that might influence the accuracy of the technique (Table 2 in [16]). Although his work is concerning surface thermometry, the basic frame of the analysis may apply to the gas thermometry since he identified possible errors in each procedure of the measurement:

- the phosphor (temperature → luminescence properties)
- the signal detection (luminescence properties → signal response)
- the algorithm for data reduction (signal response → scalar value)

For these processes, they identified possible six categories that might affect the accuracy of the measurement and their table was modified for the gas thermometry application in table 5.1.

First, the temperature difference between a particle and the gas phase should be estimated. Phosphor thermometry measures the particle temperature and assumes that it is the same with the gas temperature. Therefore, the difference between particle and gas temperature directly affect the accuracy of the thermometry. This factor will be surveyed in Section 5.2.1.

**Table 5.1.:** Classification of the six categories of systematic errors, modified from [16].

| |
|---|
| 1. Thermal interaction<br>- the phosphor particle and the ambient air are not in thermal equilibrium<br>- influence of the phosphor particle on the gas |
| 2. Photo-physical properties of the phosphor<br>- influence of the laser fluence on the phosphorescence<br>- effect of high temperature on the phosphor<br>- effect of surrounding gas on the phosphor |
| 3. Signal detection: impact of the transfer function of the detection system<br>- influence of the particles placed between object and image plane |
| 4. Data reduction algorithm from signal response to the scalar |
| 5. Discrepancy between measured intensity ratio and fitted calibration curve |
| 6. Uncertainty of the reference thermocouple |

Second, several factors might manipulate the phosphor transfer function. A phosphor transfer function means how the phosphor converts its temperature to phosphorescence. When a factor other than temperature influences this transfer function, the factor should be carefully controlled. Among these factors identified in [16], this work addressed the effect of laser fluence, and the result will be explained in Section 5.2.2. Regarding the effect of surrounding gas, Fond et al [27] showed that no difference between the intensity ratio measured from particles in pure nitrogen and in air. If one is to apply this technique to combustion studies, one should investigate the possible irreversible change of phosphorescence after a short residence time at extremely high temperature. The thermal degradation of BAM in long exposure to intermediate temperatures was reported in many studies, e.g. [9, 49], while the survivability of the YAG:Dy and BAM particles after experiencing the flame has been reported in [96] and [88], respectively.

Third, the transfer function of the detection system that images the phosphorescence from the particles to the sensor can alter. The effect of particles suspended in the optical path was classified into this category. The results are presented in the Section 5.2.3.

Fourth, the transfer function of the algorithm that ultimately converts the signal to the temperature should be investigated. The intensity ratio method is relatively free from this issue [16], but still careless flat field image can cause a systematic error. The category 5 and category 6 were not considered because applying them to the gas thermometry was trivial.

### 5.2.1. Thermal equilibrium

When a particle locates in the gas phase, there is heat transfer between the particle and the gas phase for the temperature difference. The particle has spatial and temporal temperature distribution inside. However, one can disregard the spatial distribution of temperature with the lumped capacity model and simplify the problem, if the criterion of $Bi << 0.1$ is satisfied[2].

$$Bi = \frac{k_g}{3k_p}$$

where $k$ is the thermal conductivity and subscripts $g$ and $p$ mean gas and particle, respectively. Usually, the host materials for thermographic phosphor have much greater conductivity than air, e.g., the thermal conductivity of air at $625K$ is $4.7 \times 10^{-2}[W/mK]$ and of $Al_2O_3$ is $24.2[W/mK]$. Therefore, $Bi = 6.4 \times 10^{-4} << 0.1$ . The model could usually be justified in this condition. Now, the temporal temperature evolution is dictated by the equation.

$$-h_{conv}A_p(T_p - T_g) = \rho_p V_p C_p \frac{dT_p}{dt}$$

where, $h_{conv}$ is the heat transfer coefficient, $A$ is the surface area, $T$ is a temperature, $\rho$ is the density, $V$ is the volume, $C$ is the heat capacity, and $t$ is the time. After separating variables and integrating from initial condition, $T_p = T_{p0}$ at $t = 0$,

$$\frac{T_p - T_g}{T_{p0} - T_g} = exp(-\frac{hA_p}{\rho_p V_p C_p}t).$$

Since 2 $\mu m$ BAM particles dynamically trace the gas phase well (see Appendix A.1), one can reasonably reduce the heat transfer to only the conduction, and thus, heat transfer coefficient, $h$ becomes $2k_g/d_p$. Although the shape of BAM particles are arbitrary, one can regard it as spherical for the simplicity of the analysis. Then, $A_p = \pi d^2$, $V_p = \pi d^3/6$. Accordingly the equation reads,

$$\frac{T_p - T_g}{T_{p0} - T_g} = exp(-\frac{12k_g}{\rho C_p d_p^2}t).$$

After defining variables, $\theta \equiv \dfrac{T_p - T_g}{T_{p0} - T_g}$ and the relaxation time, $\tau_T \equiv \dfrac{\rho C_p d_p^2}{12k_g}$, the equation is rewritten as

$$\theta = exp(-\frac{t}{\tau_T}).$$

herefore, if the gas temperature is constant, it will take $\tau$ for the particle to trace the gas temperature in the error of 36.8%, $2\tau$ in the error of 13.5%, and $3\tau$ with the error of 5.0%. For example, the relaxation time of 2 $\mu m$ $BAM : Eu^{2+}$ particle at 625 $K$ air is around 20 $\mu s$, which means it will take 60 $\mu s$ to follow the gas temperature in an error of 5%. Here, $\rho_p = 3700[kg/m^3]$ which is provided by manufacturer, $C_p = 777[J/kg]$ which is approximated using $Al_2O_3$ as suggested by manufacturer, and $k_g = 4.7 \times 10^{-2}$ at 625 $K$ from [89].

### 5.2.2. Effect of laser fluence

The laser fluence can affect the phosphorescence, such as its emission intensity, lifetime, or spectra. Most of previous studies in the lamp or display industries were concerning

---

[2] This classical approach to the heat transfer of a sphere submerged in a flow is explained well in page 240-243 of [39].

the luminescence saturation, the sublinear tendency of the luminescence intensity. Three mechanisms were widely proposed for the reason: (1) a depletion of ground state [58] (2) interaction of excited states [38] and (3) temperature increase by non-radiative emission. The excitation fluence and the luminescence saturation is very interesting issue in the gas thermometry as well [28]. However, the influence of varying laser fluence on the temperature measurement (lifetime or intensity ratio), which brings a bias, will be dealt here.

In phosphor surface thermometry, for which the lifetime method has been widely used, decreasing lifetime with increasing laser fluence has been reported in e.g., [15, 30]. However, in phosphor gas thermometry, the effect of laser fluence on the BAM has been regarded negligibly weak [29, 52, 54], and using a homogeneous beam has been not considered. The calibration curve has typically been measured at one spatial point and applied to all points in the field of view. This assumption will cause a systematic error if the quantum yield depends on the laser fluence; if the laser fluence differs between the calibration curve and the actual measurement, the measured temperature will be different with the real one. Furthermore, even if the same laser fluence was used for both measurements, spatially varying laser fluence with typical sheet optics can result in variant temperature even in a uniform temperature (e.g. at room temperature). Recently, the same author in [29] showed the increasing intensity ratio with the increasing laser fluence at room temperature without detailed analysis. The present study investigated the effect by measuring the spectra from packed powder in an oven first and the intensity ratio coming from particles suspended in the air later. From the spectra measured in the oven, a possible reason for the varying spectra in varying laser fluence will be proposed. In the end, the importance of using a homogeneous beam for this measurement technique will be given.

### Investigation with packed powder in oven

The experimental setup explained in Section 3.1 were used to investigate the effect of laser fluence by measuring spectra from packed powder in an oven. The laser fluence was varied from 0.3 - 119 $mJ/cm^2$ at 5 different temperatures (300, 350, 400, 450, 500 $K$). In every measurement case, 50 shots of phosphorescence were recorded and averaged. The averaged spectra at room temperature at different laser fluence are shown in figure 5.4. Apparently, when the exciting fluence increased, the spectrum shifted towards the UV without noticeable broadening. Two peaks at 446 $nm$ and 452 $nm$ were observed, and the 446 $nm$ peak became stronger than 452 $nm$ at high laser fluence. Similarly, the shift without significant broadening of spectra were observed at 500 $K$ as shown in figure 5.5, but the effect was less consequent.

First, regarding the peak change at room temperature (452 $nm \rightarrow 446nm$), the different sites, where divalent Eu ion can accommodate, may help to analyse this peak change. According to [49], more than two sites for Eu ion exist, namely Beevers-Ross (BR), anti-BR (aBR), and mid oxygen (mO) sites. The varied crystal field in different sites can split the 5d orbital and diversifies the emission wavelength. The resultant emission spectrum is a convolution of the emission from split 5d orbital in each site to 4f orbital. The measured spectra for the 0.3 and 119.0 $mJ/cm^2$ cases are fitted with convolutions of three Gaussian peaks and illustrated as a blue and a red solid line in figure 5.4. Each Gaussian peak for

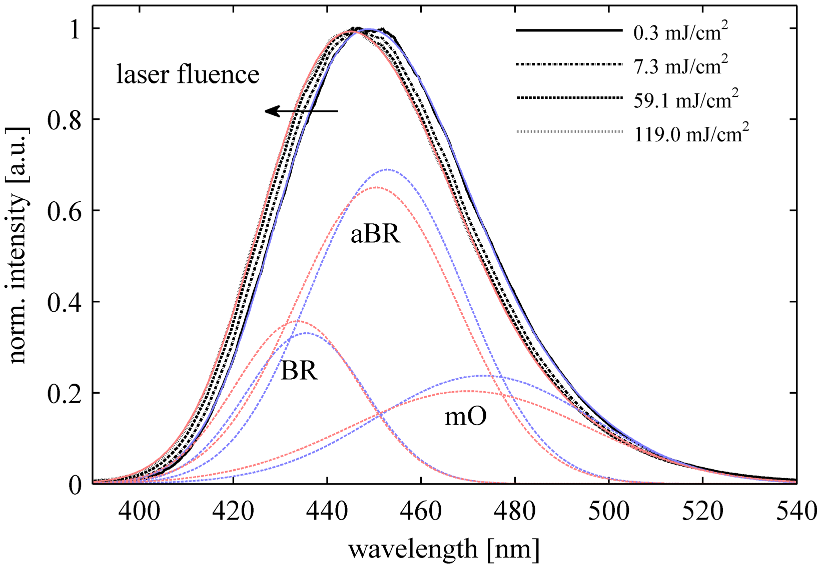

**Figure 5.4.:** Measured spectra of BAM at room temperature with varying laser fluence. The spectra were normalized with the 446 $nm$ peak. 50 shots were averaged for each case. Black solid line denotes 0.3, dash-dot line 7.3, dashed line 59.1, dotted line 119.0 $mJ/cm^2$ case. The blue and the red solid lines are fitting to the measured spectrum at 0.3 and 119.0 $mJ/cm^2$ case respectively. The fittings were composed of three Gaussian peaks (emissions from BR, aBR, mO sites). Each Gaussian peak was figured as a dashed line with the same color notation. The spectra shift towards UV without broadening with increasing laser fluence.

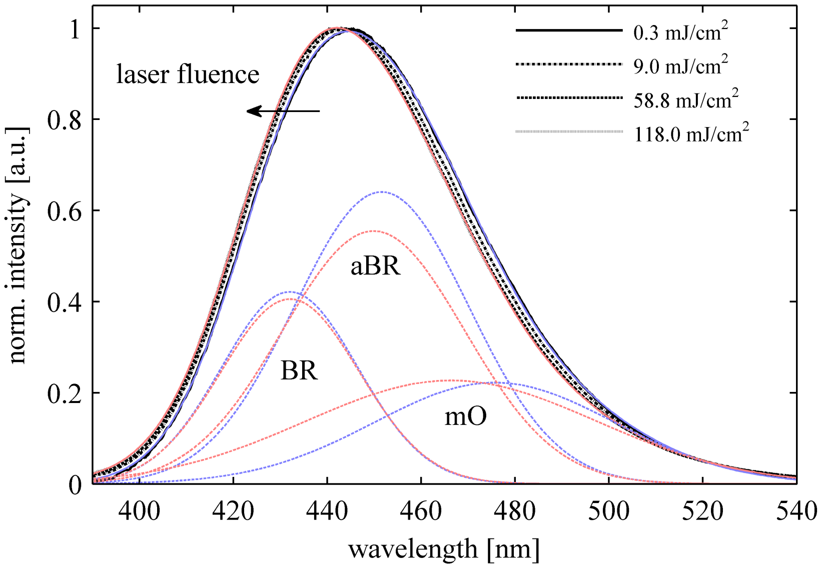

**Figure 5.5.:** Measured spectra of BAM at 500K with varying laser fluence. See figure 5.4 for the notation.

the corresponding site was figured as a dashed line with the same color with its notation. At high laser fluence, a portion of the emission at BR site increases and this can explain why the 446 *nm* peak becomes stronger than the 452 *nm* one.

The decrease of crystal field might account for the shift of spectra toward UV regime in high laser fluence. With the more intense laser fluence, the more activators are excited. The ligand interact with more activators, and thus, the crystal field is distributed wider and weakened. As a consequence, the energy level in the activator increases, and the spectra shift to UV regime universally at three Eu sites with the increase of laser fluence. It is worth to revisit the different behavior of line-emission phosphors and the broadband emission phosphors (see figure 4.13). On the contrary to BAM, varying crystal field affects little the spectra of line-emission phosphors, such as GdO, YAG:Pr, and YAG:Tb, in which the emission arises from the $(4f \rightarrow 4f)$ transition shielded by outer occupied orbitals and receive less effect by the crystal field. This complement that the varying crystal field played a role in spectra change of BAM, when the laser fluence varies. Moreover, at high temperature the spectra shift by increased laser fluence was less severe than at room temperature as shown in figure 5.5. This can be also explained in the context of the crystal field. At high temperature, by thermal expansion, the distance between the activator and the ligand is elongated, and thus, the effect of the crystal field on the energy level of activator will be weakened. Therefore, when the crystal field is weakened by increased number of interacting activators, the effect on the energy level of the activator will be also weakened. These evidences imply a possibility of laser fluence being a significant source of systematic error.

Another thing to pay attention to is the insignificant broadening. This trend contrasted with the one with temperature increase, in which the spectra not only shift but also broaden (see figure 4.3). At high temperature, the weakened crystal field by thermal expansion shift the spectra to UV regime. At the same time, the population of higher vibrational states of the activator and the increased lattice vibration cause the broadening of the spectra. Based on the spectra shift without significant broadening, it could be concluded that the tendency of spectra according to the laser fluence can not be attributed only to the temperature increase, but more related to the crystal field variation.

The expected relations of the intensity ratio to the laser fluence at different temperatures are drawn in figure 5.6. The spectra at varying laser fluence were multiplied by the each transmission curve of the filter set in figure 4.3. The integrations of the multiplications were regarded as expected signal in blue and red channels and the division of them was assumed as the intensity ratio. Normalization was performed by dividing with the intensity ratio at the smallest laser fluence. As expected from the shift of the spectra, the laser fluence affected the simulated intensity ratio significantly, and this trend was weakened at high temperature.

Although the laser fluence effect on the intensity ratio appears clear from the spectra of packed powder in the oven, one may not conclude the significance of this effect. It is for the different behaviour of packed powder and individualized particles as pointed by [28]: 1) a multiple scattering effect prevails in packed powder [94] and 2) repetitive excitation and long residence time at high temperature can degrade the material. Therefore, an investigation with particles suspended in the air were followed to confirm the effect.

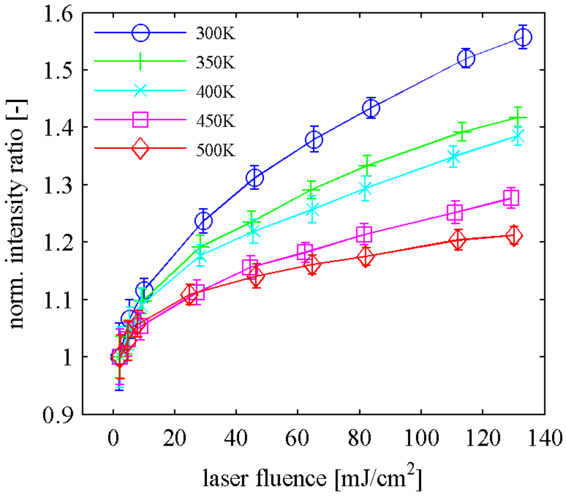

**Figure 5.6.:** Simulated intensity ratio trend of BAM with increasing laser fluence. The intensity ratio was calculated by using measured spectra of packed powder in oven and filter set in figure 4.3. The intensity ratio was normalized to the value at the lowest laser fluence at each temperature. The sample number was 50, and the error bars denote one standard deviation.

### Investigation with aerosolized particles in air

With the experimental setup explained in section 3.2, the trend of intensity ratio with laser fluence at two different temperatures was investigated by adjusting the laser energy with lambda half plate. The intensity ratios from the region ($1.7mm \times 1.7\ mm$) inside the jet core were sampled and the ensemble average and one standard deviation were graphed in figure 5.7.

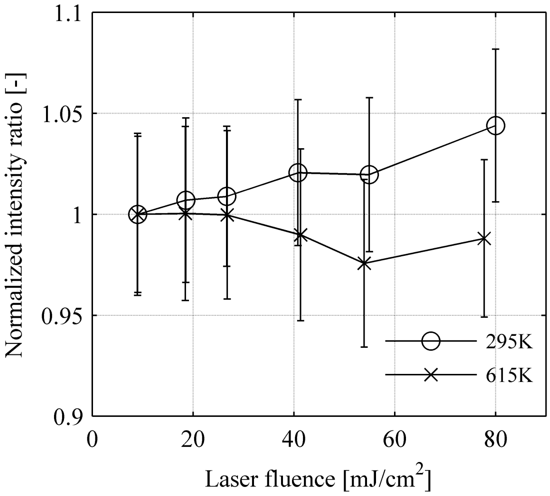

**Figure 5.7.:** The normalized intensity ratio over the laser fluence varying $9 - 80\ mJ/cm^2$ in two different temperatures. Symbols denotes ensemble average and the bars one standard deviations. The data was sampled from in jet core region spanning $1.7mm \times 1.7\ mm$.

As seen in figure 5.7, the intensity ratio increased around 5% in the room temperature as if the temperature increased. However, at 615 $K$, the intensity ratio almost did not increase. The result is consistent with the oven experiment: (1) strong excitation increased the intensity ratio and (2) this influence appeared severer at room temperature than at high temperature. At the same time a discrepancy between the investigation on packed powder and individualized particles existed; around 27% increase in packed powder and 5 % in aerosolized particles in the range from 10 to 80 mJ/cm$^2$. As mentioned previously, the multiple scattering inside the packed powder played a role in the difference. However, it is worth to mention the different homogeneity of the excitations in the both experiments. In the oven experiment, a homogenizer has been used that the phosphorescence from packed powder was assumed to stem from homogeneous laser excitation. By contrast, although a 'top hat' profile excitation was applied by using only part of the beam for the measurement in figure 5.7, the beam profile in the out-of-plane direction is not uniform, but resembles a Gaussian profile. The aerosolized particles in the air, therefore, are exposed to various laser fluence according to the position in the out-of-plane direction. Considering that 15 particles exist in 0.5 $mm^3$ volume in typical seeding density for PIV, the intensity ratio in one interrogation window size is not resulted from one particle, but many, as also pointed in [1]; therefore, in figure 5.7, the effect of the laser fluence was averaged and smoothed out. A similar investigation was performed in [28], and a temperature increase of 25 $K$ in laser fluence increase to 80 mJ/cm$^2$ was observed at room temperature, while around 5 $K$ in this study. It is supposed that the influence of laser fluence will be accentuated in thinner laser sheet. They used only one cylindrical lens for focusing in [28], thus the thickness could be estimated roughly around 300 $\mu m$ in typical divergence of the laser.

The 5% error seems negligible at the first glance, but one should keep in mind that the laser sheet profile varies vertically as a Gaussian function with typical sheet optics. In the separate measurement with the sheet optics comprised of -50, $+150$, and $+400$ $mm$ cylindrical lenses, $\pm 10K$ and $\pm 7.5K$ error were observed in a horizontal and a vertical direction in the room temperature. At 540K, $\pm 10K$ error in vertical direction were present. This error was believed to stem from inhomogeneous laser fluence in the in-plane direction and overcome with a homogeneous beam. By applying beam with the spatial inhomogeneity of 7% (one standard deviation), the bias was below $\pm 2K$ at 295 $K$.

### 5.2.3. Effect of seeding density

#### Multiple scattering of phosphorescence

The existence and its significance of multiply scattered light could be conjectured by seeding the co-flow only and evaluate the signal in the jet region. The tubing of the jet was carefully cleaned to prevent stuck particles on surfaces from being entrained into the jet flow. An axially averaged signal profile of single shot with seeding density in co-flow of $3.96 \times 10^{10}/m^3$ is presented in figure 5.8. Around 8 % of co-flow signal exist in the jet region for both channels, which was believed to be multiply scattered light from co-flow region.

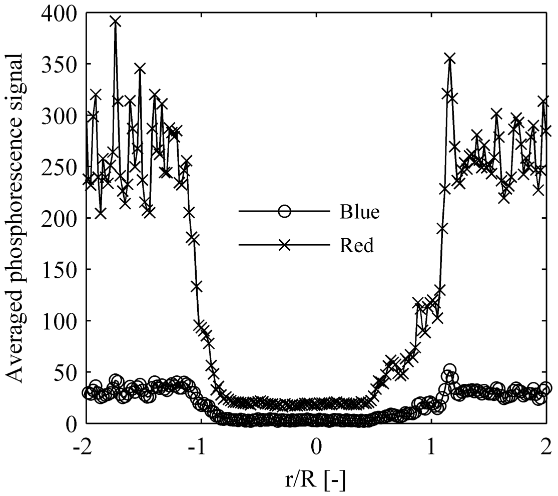

**Figure 5.8.:** The existence of multiple scattering: an axially averaged 1d profile of signal in the blue and the red channel. In this single shot, the co-flow seeding density was $3.96 \times 10^{10}/m^3$ and the jet seeding was turned off. Around 8 % of co-flow signal exist in the jet region.

To evaluate how strong this effect is, the equation of intensity ratio was revised to account for the effect as below.

$$r_j = \frac{S_{pp}^{blue} n_j + S_{ms}^{blue} n_c}{S_{pp}^{red} n_j + S_{ms}^{red} n_c} = \frac{S_{pp}^{blue} + S_{ms}^{blue}/R_{sd}}{S_{pp}^{red} + S_{ms}^{red}/R_{sd}} \tag{5.2}$$

here, $S_{pp}$ denotes signal per particle, $n$ seeding density, subscript $j$ and $c$ denotes jet and co-flow respectively. The superscript *blue* and *red* denote the blue and red channels. It was assumed that the multiple scattering increases linearly with $n_c$ and its coefficient was denoted by $S_{ms}$. The ratio of $n_j$ to $n_c$ is denoted as $R_{sd} = n_j/n_c$. Measured data were used to sample the intensity ratio from $2.4mm \times 2.4mm$ region in the jet core. By using particle locating algorithm (Section 3.2.3), the seeding densities were drawn. The jet seeding density was obtained considering the same region with the intensity ratio sampling. The seeding density for the co-flow was extracted from the area with the same size, but different positions with the jet seeding density sampling. The jet temperature was 615 $K$ and the co-flow temperature was 310 $K$. The relation between $R_{sd}$ and $r_j$ extracted from the measurement is presented in figure 5.9.

The result shown in figure 5.9 compelled the measurement technique to control the seeding density ratio to be larger than two. Including instant measurements with the seeding density ratio smaller than two shall accompany a systematic error from the multiple scattering effect.

On the other view, the multiple scattering may imply the possible temperature bias in a local region. According to the degree of multiple scattering, not only lights from particles in a position contribute the signal but also lights from particles in the surrounding. If the temperature in the position and the surrounding differs significantly, a bias will occur especially in the region of fewer particles. Basically, no information should be exploited, where no particle is.

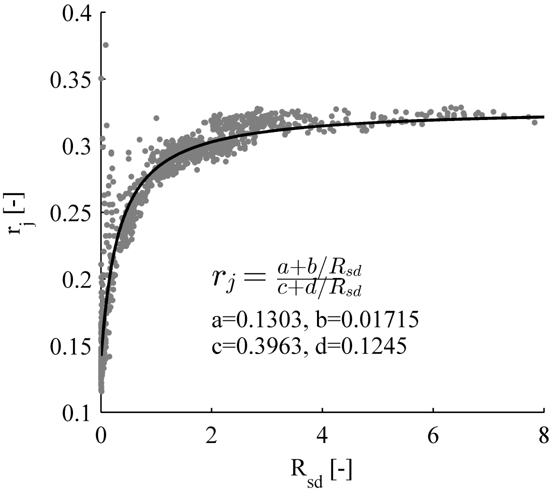

**Figure 5.9.:** The trend of intensity ratio according to the ratio of seeding densities in jet and co-flow. Data are sampled from $2.4mm \times 2.4mm$ region in the jet core. The jet temperature was 615 $K$ and a co-flow temperature was 310 $K$. The fitted curve of the equation is also drawn. Seeding densities were extracted from the particle location algorithm discussed in Section 3.2.3.

To investigate this effect, the location of each particle in every single shots from a measurement were identified based on the particle locating algorithm (Section 3.2.3). Based on this information, the number of particles in each pixel (corresponding to $170\mu m \times 170\mu m$ in measurement volume) could be counted by applying two dimensional histogram. One can mask pixels by applying minimum number of particles. Then, ensemble average were obtained applying the mask. The one dimensional radial profiles of average temperatures at the axial position of x=1d with different masks are shown in figure 5.10.

As shown in figure 5.10, little difference was observed among the profiles with different masks except in the shear layer. In the shear layer, there were mixing between the hot jet and the cold co-flow that we intentionally controlled as dense in jet and thin in co-flow. By increasing the particle number for masking, it was more likely to select the temperature from hot jet than cold co-flow and it has resulted in bias to a high temperature in this region. Therefore, the bias in shear layer is more likely for the reason stated above rather than the multiple scattering effect.

Based on this investigation, it can be concluded that (1) the relative seeding density $R_{sd}$ should be larger than two in this specific configuration; and (2) the seeding density should satisfy the compromise between an acceptable level of multiple scattering and sufficient signal-to-noise ratio. In the measurement in Section 6.1, seeding densities of jet and co-flow were in the range of $6.3 \times 10^{10}$ to $1.9 \times 10^{11}/m^3$ and $3.2 \times 10^{10}$ to $4.7 \times 10^{10}/m^3$, respectively, fulfilling this demand.

### Attenuation of phosphorescence

The phosphorescence could be attenuated either by scattering or absorption by the particles in the optical path from the object plane (laser plane) to the image plane (imaging sensor plane). If the attenuation occurs differently for the blue and red channels, the

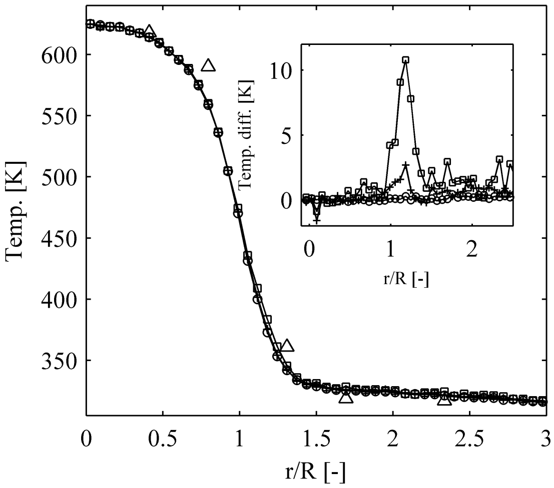

**Figure 5.10.:** Mean radial temperature profiles at x/d=1 obtained using 170 x 170 $\mu m$ wide interrogation volumes that contained at least 1, 2, or 3 particles, denoted by symbols ○: 1, +: 2, □: 3. Thermocouple measurements are denoted by triangles (△). Relative temperature differences are shown in comparison to a mean temperature profile where the threshold has been set to zero.

intensity ratio will also be affected.

However, scattering is not expected to be significantly different in the two channels because the central wavelengths of blue and red channels are separated approximately 70 $nm$. Assuming the shape of the particles spherical and the validity of Lorenz-Mie theory, the scattering efficiencies in both channels will be similar based on the size parameter. Therefore, scattering was not considered any further.

Meanwhile, absorption could attenuate light of the two channels differently. According to the excitation spectrum provided by the manufacturer, the absorption spectrum has the highest peak wavelength around 390 $nm$ and rapidly decreases to 10 % of the peak at 425 $nm$ as shown in figure 5.11. Therefore, it is likely for the excitation and emission spectra to

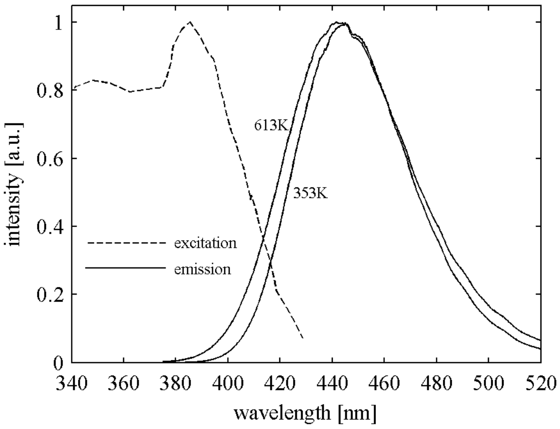

**Figure 5.11.:** Excitation and emission spectra of BAM. The excitation spectra were provided by manufacturer.

intersect each other especially at high temperature because the emission spectra of BAM shift towards UV regime with increasing temperature. Accordingly, one can reasonably suspect that a preferential absorption in the blue channel might happen.

To evaluate the significance of preferential absorption, two different seeding materials were seeded in two separate measurements. The jet was seeded with BAM in both cases to emit phosphorescence in the object plane. At one case, the BAM was seeded in the co-flow, which was suspected to absorb part of the phosphorescence. At the other case, MgO was seeded, which does not absorb the phosphorescence. By comparing two cases, one could estimate the significance of preferential absorption. The spatially averaged intensity ratio in $2.4mm \times 2.4mm$ region in the jet core (at x=0.7d) from each single shot was sampled. The seeding density in the co-flow was measured from simultaneously measured Mie-scattering images. The jet was heated to 610 $K$ whereas the co-flow remained at 310 $K$. The seeding density ratio, $R_{sd}$ was larger than two. The results are shown in figure 5.12.

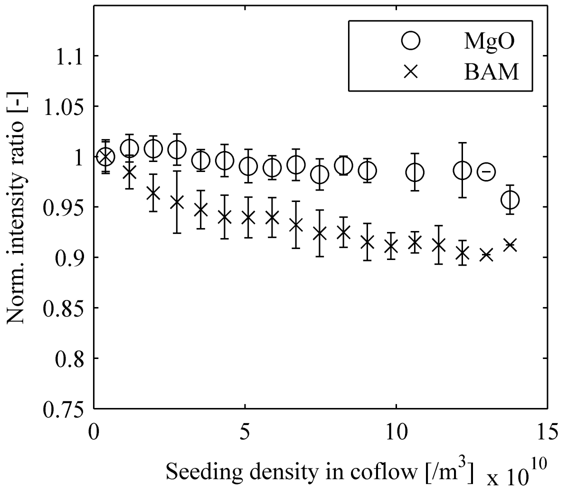

**Figure 5.12.:** The trend of normalized intensity ratio against the seeding density in the co-flow with different seeding materials. The jet temperature was 610 $K$ and the co-flow temperature was 295 $K$. The averaged ratio from $2.4mm \times 2.4mm$ region in the jet core and the number of particles in the same size in the co-flow from each single image were sampled. The data were binned in the size of 7.9e$^9$ and the mean (denoted by symbols) and standard deviation (denoted by bars) are graphed. The samples are conditioned with $R_{sd} > 2$.

As shown in figure 5.12, in MgO case (denoted by circles), the normalized intensity ratio was almost independent of the seeding density of the co-flow. As a contrast to MgO case, the normalized intensity ratio decreased apparently around 10 % at seeding density of $1.2 \times 10^{11}/m^3$ in BAM case. This difference may imply the presence of preferential absorption by BAM particles. However, it should be mentioned that the trend shown in figure 5.12 could be explained not only by preferential absorption but also by multiple scattering. In the case of BAM, emission from BAM particles presented in cold co-flow region is multiply scattered to the jet region to lower the intensity ratio. This would not happen in MgO case since no luminous particle were present in the cold co-flow region.

# Chapter 6.

# Validation of measurement technique

In this chapter, the reliability of the thermographic PIV is demonstrated by comparing the present result with the previous studies on an axisymmetric jet. The results of studies concerning the near-fields of the jet were directly compared or the tendencies extracted from the results were compared with the present results. The limitation of the measurement technique or different measurement conditions, such as Re, the density ratio of the jet and the ambient, were suggested to account for the discrepancies between the previous studies and the present one. Furthermore, by contrasting the studies concerning far-field of the jet, which are regarded as references widely, and the present study, the trend to the self-preservation could be clearly seen.

## 6.1. Background of axisymmetric jet

The round jet has been a canonical configuration that played an important role to understand fundamentals of fluid dynamics. Theorists were attracted by its mathematical simplicity from axisymmetry and the applicability of the boundary layer approximation. Furthermore, after assuming self-preservation, the partial differential equation reduces to the ordinary differential equation. Not only having the mathematical reasons, it also has a broad range of practical applications, such as burners, chimneys and stacks. Therefore, it has been thoroughly investigated during the last decades, and thus, an extensive volume of experimental, numerical, and analytical studies exist, e.g. [12, 21, 32, 40, 41, 71, 92] to name just a few. By the former studies on the round jet, abundant and reliable data to compare with the result of the present study were assured. Additionally, an absence of confining walls, which usually cause spurious background signals in optical measurement technique, were another reason for applying the developed measurement technique, minimizing experimental complexity.

**Far-field** Applying the self-preservation (or similarity) to a phenomenon, which means assuming the presence of one profile of a quantity and applying it to the whole region after suitable normalization with local quantity, makes the phenomenon immensely tractable as applied to laminar boundary layer theory by Blasius. An example of more physical insight of self-preservation could be found in [32] as follow:

*"Self-preservation implies that the flow has reached a kind of equilibrium where all of its dynamical influences evolve together, and no further relative dynamical readjustment is necessary."*(39 page of [32])

Applicability of self-preservation to the round jet has been an interest of the fluid dynamics society and investigated by many researchers. The classical approach to the self-preservation of round jet is assuming (1) the presence of one profile of a flow quantity e.g., velocity, turbulence intensity, in the far-field, (2) that the jet is issuing from one point source of momentum and thus (3), the jet spreads and decays in the same rate. As a consequence, the characteristic scales, such as centerline velocity and turbulence intensity, should converge asymptotically to a universal value for all jets, independent on initial states [32]. Early experimental work in 1940-50s succeeded to show the self-preserving axial mean velocity profiles some few diameters downstream but failed for the turbulence intensity. This failure motivated the work of Wygnanski & Fiedler [92], and they demonstrated self-preserving mean velocity, turbulence stresses, integral length scales, and the triple velocity correlations etc. However, it was found that the results of Wygnanski & Fiedler do not satisfy the momentum conservation, maybe because of the recirculation of the flow from the confinement. Hussein et al. [40] and Panchapakesan & Lumley [71] performed similar experiments with Wygnanski & Fiedler, but in a large confinement and demonstrated the results that satisfied the momentum conservation equation. Now their results are regarded reliable for the turbulent round jet in the far-field.

The self-preservation in the jet is well summarized in §5 of [69], and the round jet with a high Reynolds number ($10^4$, roughly) is regarded as being self-preserving beyond the developing region (x/d>30, roughly) according to the same reference. Interestingly, beyond the developing region, not only the mean and rms fluctuation of the velocity and the scalars, but also the Reynolds stresses, turbulent kinetic energy, turbulent diffusivity, integral length scales and etc. are self-preserving.

Mathematical formulations, which are largely based on [69], are provided to give general concept of self-preservation. Regarding a quantity, $Q(x,r)$, suitable characteristic scales $Q_0(x)$ and $\delta(x)$ exist that the independent variable $r$ and dependent variable $Q$ are scaled as

$$\gamma \equiv \frac{r}{\delta(x)},$$

$$\widetilde{Q}(\gamma, x) \equiv \frac{Q(x,r)}{Q_0(x)}$$

when the function $\widetilde{Q}$ is independent on $x$, or a function $\widehat{Q}$ exists that satisfies,

$$\widetilde{Q}(\gamma, x) = \widehat{Q}(\gamma),$$

then, the function $Q(x,r)$ is said to be self-preserving. Furthermore, the local characteristic scales, $Q_0(x)$ and $\delta(x)$ usually exhibit the power-law dependence on $x$.

The centerline axial velocity, $\langle U\rangle_0(x)$ and the jet's half width, $r_{\frac{1}{2}}(x)$ are used for the scaling of the mean axial velocity $\langle U(x,r)\rangle$. Here, $\langle U\rangle_0(x) = \langle U(x,0)\rangle$ and $\langle U(x, r_{\frac{1}{2}}(x))\rangle = \frac{1}{2}\langle U\rangle_0(x)$. The profile of scaled axial velocity is self-preserving, that is,

$$\langle U(x,r)\rangle = \langle U\rangle_0(x)\widehat{U}(\frac{r}{r_{\frac{1}{2}}(x)})$$

For the passive scalar, the normalized temperature $\Theta$ was used in this study.

$$\Theta = \frac{T - T_c}{T_h - T_c}$$

, $T_h$ is the centerline temperature at jet exit and $T_c$ is the temperature of co-flow. $T_h$ and $T_c$ in different $Re$ are summarized in table 3.1. As characteristic scales of $\Theta$, the centerline scalar, $\langle\Theta\rangle_0(x)$ and the jet's half width based on average scalar profile, $r_{\frac{1}{2},\theta}(x)$ were used. Here, $\langle\Theta(x, r_{1/2,\theta}(x))\rangle = \frac{1}{2}\langle\theta\rangle_0(x)$. The profile of the scaled temperature is self-preserving, that is,

$$\langle\Theta(x,r)\rangle = \langle\Theta\rangle_0(x)\widehat{\Theta}(\frac{r}{r_{\frac{1}{2},\theta}(x)})$$

The characteristic scales should follow the power-law, more specifically,

$$\frac{\langle U\rangle_0(x)}{U_0} = \frac{B}{(x-x_0)/d}$$

here, $U_0 = \langle U(0,0)\rangle$ is the jet bulk velocity, $B$ is an experimental constant, and $x_0$ is a virtual origin, which is also determined experimentally.

$$\frac{\langle\Theta\rangle_0(x)}{\Theta_0} = \frac{B_\theta}{(x-x_{0,\theta})/d}$$

here, $\Theta_0 = \langle\Theta(0,0)\rangle$. $B_\theta$ is an experimental constant, and $x_{0,\theta}$ is a virtual origin based on the scalar field. While the $\langle U\rangle_0$ and $\langle\Theta\rangle_0$ depend on $1/x$, the jet's half widths linearly depend on $x$,

$$r_{1/2}(x) = S(x-x_o)$$

$$r_{1/2,\theta}(x) = S_\theta(x-x_{o,\theta})$$

here, $S$ and $S_\theta$ are experimental constants.

While the classical approach assumed a single self-preserving state in the far-field for all different jets, George [32] proposed in his theoretical analysis the possible multiplicity of a self-preserving state dependent on the initial state. He argued that the shape of profiles should match each other for all self-preserving jets, but the scale factors may differ from each other. He attributed the scatter of asymptotic value of scale factors in various experiments to this multiplicity. Therefore, the studies in the developing region were attempted to investigate the effect of the initial state on the self-preservation on one hand, and to understand the dynamics of transition to the self-preservation in each condition on the other hand.

**Near-field** Some of the previous studies investigated the influence of various initial conditions, such as, Re, density ratio, jet outlet profile, on the development of the round jet. Russ & Strykowski [76] adjusted the boundary layer thickness in the jet outlet issuing from a smoothed nozzle by using different length of the extension ring. They observed the delayed momentum mixing with the increasing boundary layer thickness. Similarly, they also increased the turbulence intensity by positioning a turbulence grid after the extension ring and showed the delay of mixing with increasing turbulence. In addition, they adjusted the density by heating the flow and observed fast mixing in low density ratio. They argue that the increase of the boundary layer thickness and the turbulence suppressed the instability to form a vortex, hence the mixing in the near-field was degraded, while a low density ratio increased the instability and raised the mixing rate.

Amielh et al. [5] investigated the effect of density ratio and Re by using different gases of Helium, air and $CO_2$. The enhanced mixing rate was also observed in low density and increased Re, but the effect of the density was stronger than the Re. Papadopoulos & Pitts [66] investigated the effect of Re by mixing different ratios of propane and methane and observed rapid mixing in low Re. Boersma et al. [12] performed a DNS in a jet of Re 2400, issuing from a smoothed nozzle, and justified their result by comparing far-field results with the ones of the experimental references. They compared self-preservations of jets issuing from the top-hat profile (from smoothed nozzle) with the profile of a second polynomial and concluded the dependence of self-preservation on initial state, which is as well supporting the argument of [32]. After that, Mi et al. [41] measured the passive scalar fields (temperature) of the jets from the smoothed nozzle and the long pipe and demonstrated the dependence of self-preserving state on the initial state. Some of the previous studies are summarised in table 6.1.

**Governing equation** Turbulent flows are solved statistically. The nature of the turbulence is random, thus predicting the instantaneous velocity and scalar is not realizable. The instantaneous variables are decomposed to mean and fluctuation, which is called as Reynolds decomposition.

$$\begin{aligned} U &= \langle U \rangle + u, \\ V &= \langle V \rangle + v, \\ \Theta &= \langle \Theta \rangle + \theta, \end{aligned}$$

here, upper letters denote instantaneous values, lower letters fluctuations, and $\langle\rangle$ means ensemble averaging. In the following analysis, an ensemble average is regarded as the mean. Substituting instant variables in Navier-Stokes equation results in Reynolds equation, and in addition, for a round jet flowing into a quiescent ambient, the Reynolds equation might be more simplified by applying the boundary layer approximation as[1],

$$\langle U \rangle \frac{\partial \rho \langle U \rangle}{\partial x} + \langle V \rangle \frac{\partial \rho \langle U \rangle}{\partial r} = \frac{\nu}{r} \frac{\partial}{\partial r} \left( r \frac{\partial \rho \langle U \rangle}{\partial r} \right) - \frac{1}{r} \frac{\partial}{\partial r} \left( r \rho \langle uv \rangle \right). \tag{6.1}$$

The corresponding continuity equation is,

$$\frac{\partial \rho \langle U \rangle}{\partial x} + \frac{1}{r} \frac{\partial}{\partial r} \left( r \rho \langle V \rangle \right) = 0. \tag{6.2}$$

Lastly, the equation for conserved scalar is,

$$\langle U \rangle \frac{\partial \rho C_p \langle \Theta \rangle}{\partial x} + \langle V \rangle \frac{\partial \rho C_p \langle \Theta \rangle}{\partial r} = \frac{k}{r} \frac{\partial}{\partial r} \left( r \frac{\partial \rho C_p \langle \Theta \rangle}{\partial r} \right) - \frac{1}{r} \frac{\partial}{\partial r} \left( r \rho C_p \langle v\theta \rangle \right). \tag{6.3}$$

## 6.2. Results and discussion

This study measured the velocity and the temperature quasi-simultaneously in the developing region of a heated round jet, which covers axial distance from 1 to 15 jet diameter.

---

[1] Detail derivation is found in page 111- 114, 161 of [69]. The equation of conserved scalar is transformed to cylindrical coordinate.

**Table 6.1.:** Overview of previous studies on the effect of initial state on the jet development

| | *Range [d]* | *Nozzle* | *Re* | *Density ratio* | *Meas.* | *Method* |
|---|---|---|---|---|---|---|
| Boguslawski 1976 [13] | 0 - 12 | P | U=20,30,49 | 1 | V | HWA |
| Birch 1978 [20] | 0 - 70 | P | 16000 | $CH_4$(0.55) | C | RS |
| Lockwood 1980 [55] | 0 - 50 | P | 50000 | 0.54 (heating) | T | Th |
| Pitts 1991 [68] | 10 - 30 | P | 3950<br>7890 | 0.14,0.55<br>1.02,1.55<br>3.01,5.11 | C | RLS |
| Russ 1993 [76] | 0 - 10 | N | 10000 | 0.5-1.0 (heating) | V<br>T | HWA<br>Th |
| Amielh 1995 [5] | 0 - 25 | P | 7000<br>21000<br>32000 | He (0.14)<br>air(1)<br>$CO_2$(1.4) | V | LDA |
| Papadopoulos 1998 [66] | 0 - 30 | P | 3300 - 23000 | propane + methane | V<br>C | HWA<br>RLS |
| Weisgraber 1998 [91] | 15 - 30 | N | 5500<br>160 00 | 1 | V | DPIV |
| Boersma 1998 [12] | 0 - 42.5 | N,P | 2400 | 1 | V | DNS |
| Mi 2001 [41] | 0 - 70 | N,P | 16000 | 0.85 | T | CWT |
| Fellouah 2009 [26] | 0 - 28 | N | 6000<br>10000<br>30000 | 1 | V | HWA |

Nozzle: P, Pipe; N, smoothed nozzle; *Meas*: V, velocity; C, concentration; T, temperature; *Method*: HWA, hot wire anemometry; RS, Raman scattering; Th, thermocouple; RLS, Rayleigh light scattering; LDA, laser doppler anemometry; DPIV, digital particle image velocimetry; DNS, direct numerical simulation; CWT, cold wire thermometry.

Here, the self-preservation is not yet achieved, but the readjustment of the flow to the ambient is ongoing. A comparison with the values in self-preserving region, however, will provide some clues to understand the development of the jet in this region.

### 6.2.1. Inlet condition

As shown in figure 3.5, a long straight pipe (>30d) was used in this study, such that the fully developed pipe flow was expected at the jet exit. The radial profile of $\langle U\rangle/\langle U\rangle_0$ and $u'/\langle U\rangle_0$ at $x = 0.5d$ are shown in figure 6.1. As shown in the left of figure 6.1, the radial profile of $\langle U\rangle/\langle U\rangle_0$ matched fairly well with the one of fully developed pipe flow,

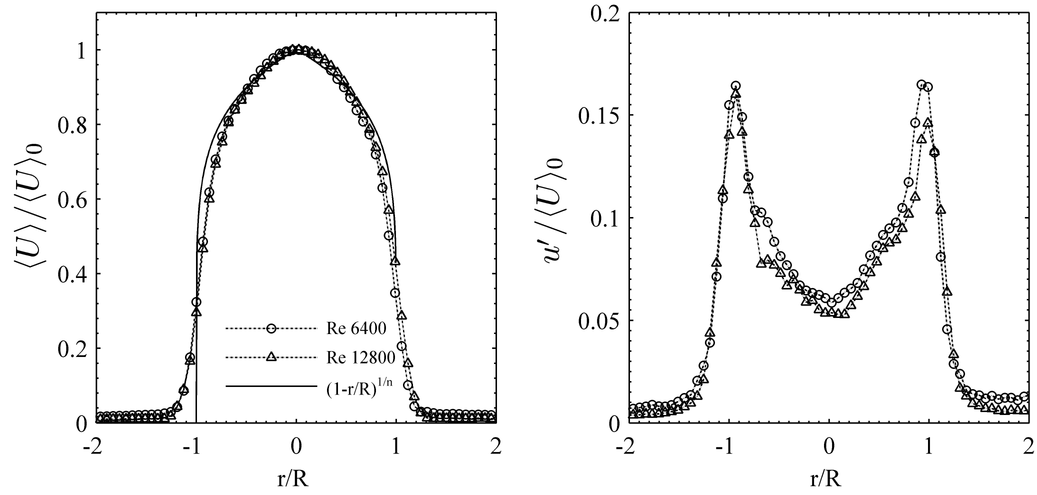

**Figure 6.1.:** The profile of $\langle U\rangle/\langle U\rangle_0$ and $u'/\langle U\rangle_0$ at $x = 0.5d$.Here, $\langle U\rangle_0 = 36.4m/s$ at Re 6400 case, 73.4 at Re 12800 case. See also table 6.2.

$(1-r/R)^{1/n}$, here, $n$ was 6.5. The profiles of many studies, e.g. [41], that used a long pipe matches well with the profile, as they measured close enough to the jet exit. In this study, however, the nearest measured position was x=0.5d, therefore the profile was smoothed slightly due to the mixing with the co-flow. As shown in the right of the figure 6.1, the turbulent intensity at the centerline was around 5-6 % close to the result from [41] and [66], which was 3-4 %. The mean scalar profile, as illustrated in the right of figure 6.2,

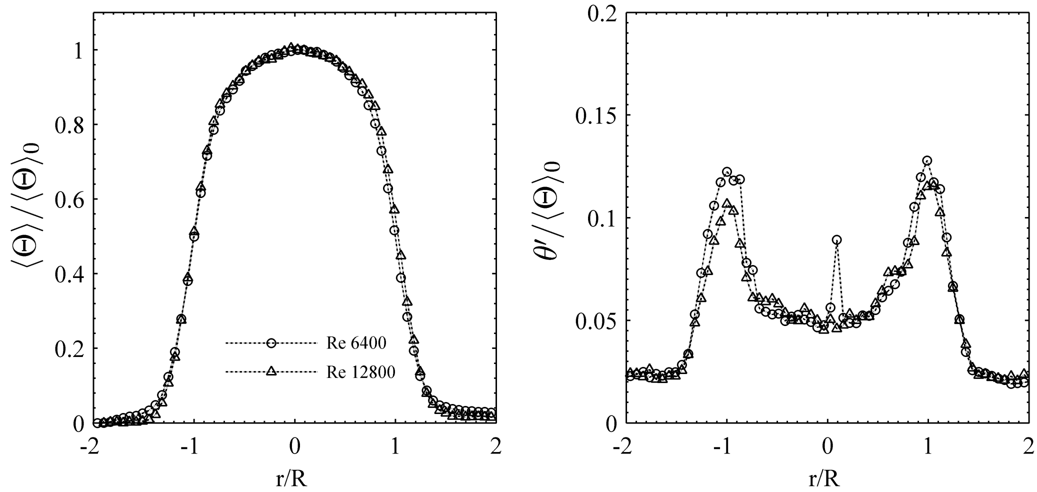

**Figure 6.2.:** The profile of $\langle\Theta\rangle/\langle\Theta\rangle_0$ and $\theta'/\langle\Theta\rangle_0$ at $x = 0.7d$.Here, $\langle T\rangle_0 = 616K, T_h = 616K, T_c = 315K$ at Re 6400 case, 623, 622, 310 at Re 12800 case. See also table 6.2.

was flatter than the mean axial velocity profile, as heat is transported faster than the momentum. The $\theta'$ displayed similar shape with $u'$, but slightly smaller value. From the profiles of $\langle U\rangle$, $u'$ at x=0.5d and $\langle\Theta\rangle$, $\theta'$ at x=0.7d, the fully developed pipe flow at jet exit can be reasonably assumed.

### 6.2.2. Mean

When the jet develops absorbing the ambient air (entrainment) and being mixed with the ambient, various factors, such as Re and density ratio, affect this process, especially in the near-fields. In figure 6.3, the effect of the Re on the jet decay is illustrated first based on mean axial velocity at jet center. It clearly indicated that the jet decays faster in the case of low Re of 6400 than the case of high Re of 12800. The same tendency has been found in the study of Papadopoulos [66]. He attributed the effect of Re on the decay to the amount of initial turbulence. In the jet issuing from the smoothed nozzle, the large eddies generated by the instability are the main source of turbulent mixing in the near-field. However, in the jet issuing from a long pipe as in this study, various scales of the turbulence exist in the jet exit and therefore the initiation of the large coherent structure is suppressed further downstream [41, 66, 76]. As a consequence, the high turbulence intensity in the low Re accelerated the turbulent mixing in the near-field. At x=15d downstream, the two cases were superimposed, which implies an approach of the mean axial velocity in the centerline to the self-preservation. However, compared to the results of Papadopoulos [66], the decay of the jet in this study seems to be slowed downstream, especially at x=15d. In this position, the axial velocity is low and the effect of the uncontrollable flow in the laboratory is suspected to affect the result. Furthermore, a ventilation duct was used to suck in the air with phosphor particles to prevent them from floating in the laboratory. This effect may explain the relatively high velocity at the downstream position.

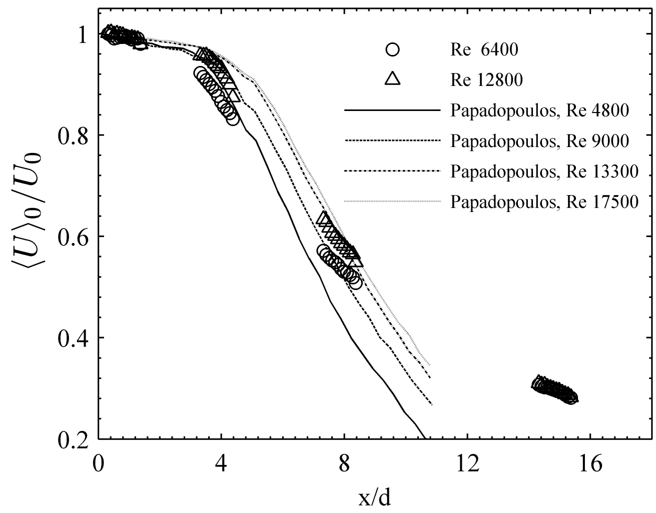

**Figure 6.3.:** Decay of axial mean velocity at the jet centerline, $\langle U\rangle_0/U_0$.

In figure 6.4, the effect of the density on the jet decay is displayed. In the work of Amielh [5], they used He, air and $CO_2$ jets to the co-flowing air (density ratio of 0.14, 1, 1.2 repectively) to investigate the density ratio effect. As observed in figure 6.4, low

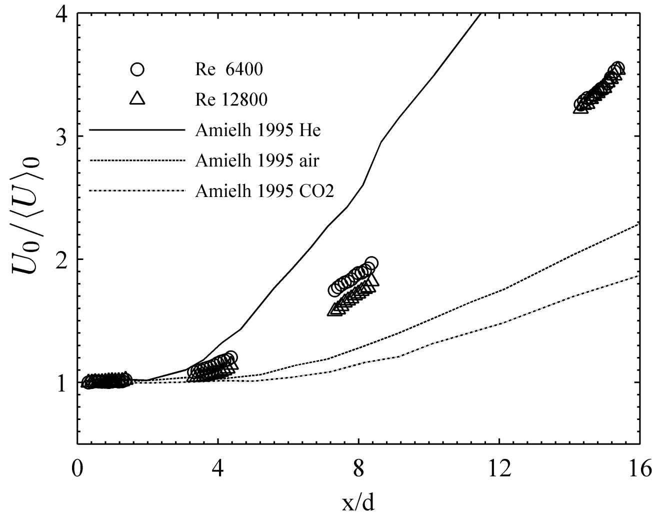

**Figure 6.4.:** Decay of axial mean velocity at the jet centerline, $U_0/\langle U\rangle_0$.

density jets decay faster. In this study, the jet was heated to about 615K, and the density ratio was around 0.5. It is evident that the result of this study presented is within the range of the previous study.

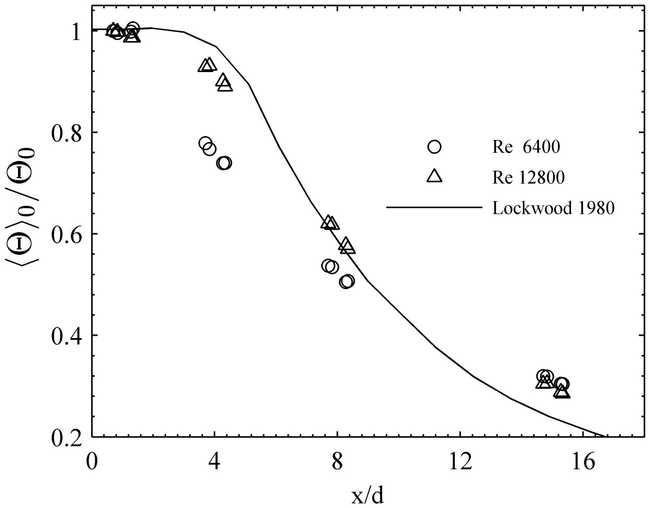

**Figure 6.5.:** Decay of axial mean scalar at the jet centerline, $\langle\Theta\rangle_0/\Theta_0$.

The decay of the mean scalar at the jet centerline is shown in figure 6.5. Similar to the decay of axial mean velocity, the mean scalar in the low Re case decays faster than the high Re case. However, the mean scalar decays much faster in x=4d downstream than the momentum (see figure 6.3), as also reported in Pietri et al. [67]. They observed the similar tendency by comparing centerline rms values and proposed that the different boundary conditions between velocity and temperature might cause the behaviour. While the boundary condition of the velocity (no-slip condition at wall in the tube and virtually stationary co-flowing air) does not change significantly after exciting the tube, but the one of the temperature changes significantly; wall temperature in the tube is generally much higher than the co-flow temperature. Additionally, a faster energy transfer than momentum transfer could account for the tendency partly. Compared to the results of Lockwood [55], the result of this study appears to decay earlier in the upstream. In [55], the Re was higher than in this study (Re 50,000) and delayed the decay of the jet in [55]. Furthermore, they heated the pipe such that the mean temperature profile at jet exit was more uniform than this study, and it took a longer time for the ambient air to penetrate into the jet center. The tube was not heated nor insulated in this study. At further downstream, $\langle\Theta\rangle_0/\Theta_0$ and $\langle U\rangle_0/U_0$ matched each other very well (compare figure 6.3 and 6.5 and see table 6.2).

**Table 6.2.:** Streamwise evolution of mean axial velocity and scalar at jet center and jet half widths.

| | $x$ | $\frac{\langle U\rangle_0}{U_0}$ | $\frac{\langle\Theta\rangle_0}{\Theta_0}$ | $\mathrm{r}_{\frac{1}{2}}$ [mm] | $\mathrm{r}_{\frac{1}{2},\theta}$ [mm] | $\mathrm{Re}_l = \frac{\langle U\rangle_0 r_{1/2}}{\nu(T(x))}$ | $\langle U\rangle_0$ $[m/s]$ | $\langle T\rangle_0$ $[K]$ | $T_h$ $[K]$ | $T_c$ $[K]$ |
|---|---|---|---|---|---|---|---|---|---|---|
| Re 6400 | 1d | 1.00 | 1.00 | 7.35 | 8.02 | 9670 | 36.7 | 615.5 | 615.5 | 315 |
| | 4d | 0.89 | 0.77 | 7.09 | 8.79 | 10500 | 33.4 | 545.6 | 615.5 | 300 |
| | 8d | 0.54 | 0.53 | 10.66 | 13.48 | 12680 | 20.6 | 467.3 | 615.5 | 295 |
| | 15d | 0.30 | 0.32 | 19.13 | 23.19 | 16270 | 11.1 | 397.5 | 615.5 | 295 |
| Re 12800 | 1d | 1.00 | 1.00 | 7.46 | 8.15 | 19390 | 73.4 | 622.9 | 621.5 | 310 |
| | 4d | 0.94 | 0.93 | 7.02 | 8.41 | 18580 | 70.2 | 599.9 | 621.5 | 300 |
| | 8d | 0.59 | 0.62 | 9.76 | 12.19 | 23088 | 45.8 | 498.6 | 621.5 | 295 |
| | 15d | 0.30 | 0.31 | 18.86 | 23.00 | 32810 | 22.5 | 394.9 | 621.5 | 295 |

$T_c$: co-flow was heated unintentionally by the heat transfer from the pipe for the jet. Entrainment of unheated laboratory ambient was observed from x=4d position. Therefore, the co-flow temperature to calculate normalized temperature, $\Theta$ was varied as shown in the table.

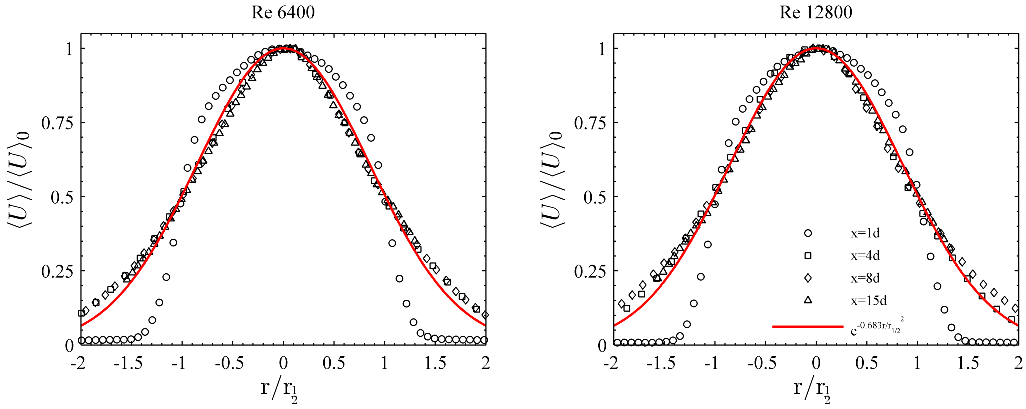

**Figure 6.6.:** Mean profiles of axial velocity, $\langle U\rangle/\langle U\rangle_0$. See table 6.2 for absolute values.

In figure 6.6, the radial profiles of mean axial velocities in different downstream positions are shown. The profiles show a reasonable symmetry. Furthermore, except the position at x=1d, all profiles are in good accordance with the profile of self-preservation, $e^{-0.683\frac{r}{r_{1/2}}^{2}}$. It could be assumed that the radial profile of the mean axial velocity reaches the self-preservation early upstream compared to other variables, such as turbulence intensity and Reynolds stresses, which will be shown in the following. The similar tendency with the mean axial profile of the scalar is indicated in figure 6.7. Here, the co-flow temperature to calculate normalized temperature, $\Theta$ was varied as shown in the table 6.2. Co-flow was heated unintentionally by the heat transfer from the pipe for the jet and entrainment of unheated laboratory ambient was observed from x=4d position.

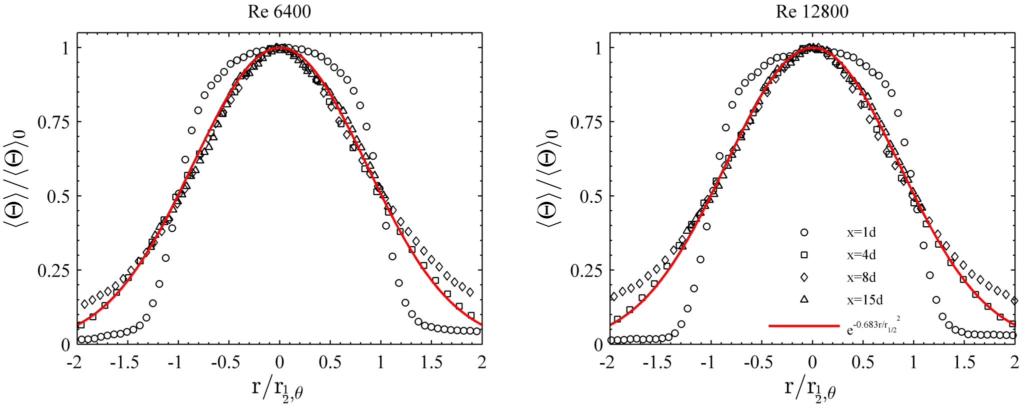

**Figure 6.7.:** Mean profiles of scalar, $\langle\Theta\rangle/\langle\Theta\rangle_0$. See table 6.2 for absolute values.

From these profiles, the jet half width from the mean axial velocity, $r_{\frac{1}{2}}$ and from the mean scalar, $r_{\frac{1}{2},\theta}$ were calculated and summarised in figure 6.8. The jet of the low Re case spreads faster than within the high Re case and it was clearly observed for the both $r_{\frac{1}{2}}$ and $r_{\frac{1}{2},\theta}$ in x=8d position. However, at the x=15d position, the difference between low and high Re case was invisible. Both scales based on $\langle U\rangle$ and $\langle\Theta\rangle$ were laid in good agreement with the previous studies.

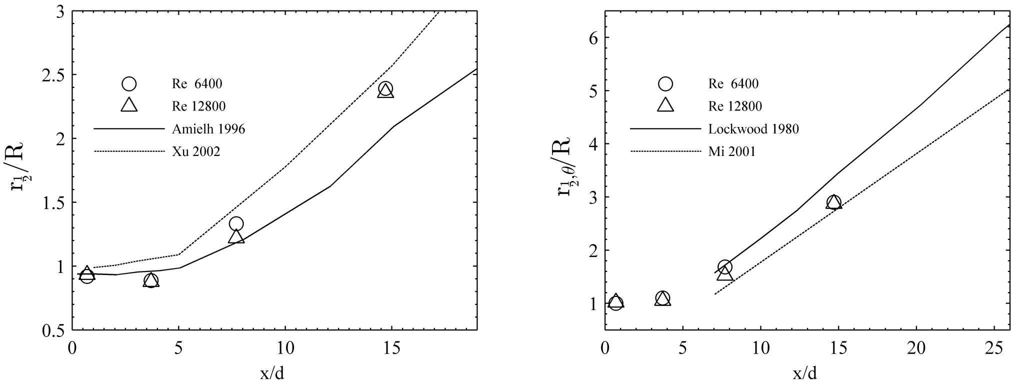

**Figure 6.8.:** Jet half width based on $\langle U\rangle$ and $\langle\Theta\rangle$.

### 6.2.3. Root mean square

Some of the effects on jet development were observable with mean profiles in the previous section, and a similar investigation through rms values is presented in this section. In figure 6.9, the rms of the normalized scalar at jet centerline, $\theta'/\langle\Theta\rangle_0$ depending on the axial position are shown. Generally speaking, it is apparent that the jet was approaching to the asymptotic value of 0.22 ([41]) or 0.21([55]) in the self-preserving state, but did not reach it yet. Compared to the previous studies, the rms of the present study at x=1d were larger than the result from Lockwood & Moneib [55] and Mi et al. [41]. Because the tube was heated in both studies, the scalar profiles were more homogeneous than within this study, and thus, the rms of the scalar was also very low (less than 5e-3) in their studies. However, in this study, there was a heat transfer between the heated jet and the tube, and thus, the rms value were relatively large. Furthermore, the higher Re of [55] (50,000) and higher density ratio of [41] (0.85) than within this study delayed the decay and hence the mixing in the centerline further downstream. In the contrary, the jet in the study of Pitts [68] appears to decay much faster than this study and reached the self-preservation upstream. This effect could be attributed to the low Re of 3950 in his work. The result of this study showed a good agreement with the work of Birch et al. [20] who used a methane jet into air co-flow (density ratio 0.5) and Re of 16,000, which are quite similar with this study.

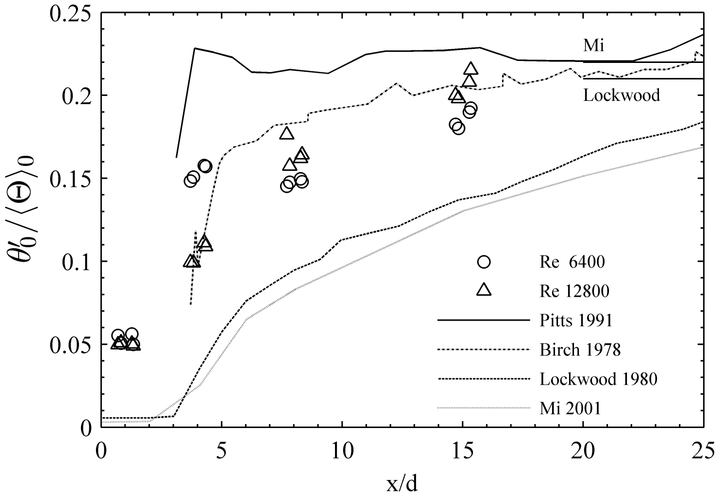

**Figure 6.9.:** Streamwise evolution of rms of normalized scalar at jet center.

An interesting point was found in figure 6.9 when observing x=4d and 8d positions particularly. In low Re case, a local maxima ('hump') existed at x=4d, while no hump was observed in the high Re case. This is inconsistent with [41]. They investigated the effect of different jet exit velocity profiles (top-hat from smoothed nozzle and one from long pipe) on the jet development. First, they reviewed previous studies, separated the works with smoothed nozzle and long pipe and compared them. They found a 'hump' of normalized rms of scalar only in the jet issuing from the smoothed nozzle, but not in the jet issuing from the pipe. Furthermore, they confirmed this with their own experiment.

Thus, a jet issuing from the long pipe is not expected to have a hump in the normalized rms of the scalar, which was the case in low Re of this study. The low Re might be a plausible explanation for the 'hump' in our observation, because all Re in the work reviewed in [41] (including their own experiment) were larger than 16,000, with the exception of one case. However, the specific mechanism invoking the 'hump' in the low Re were out of the scope in this study. Additionally, the normalized rms of scalar increased more rapidly in the high Re case than the low Re case downstream, x>4d. The transition of turbulence proposed by Dimotakis [22] might explain this. According to him, fully developed turbulence can not sustain below Re of 1-2e$^4$, which might separate the different Re cases investigated in this study (see local Re in table 6.2). In low Re, although fast mixing for the low Re upstream (x<4d) was achieved, but it could not be sustained, thus the mixing in the high Re case became faster that the one in low Re.

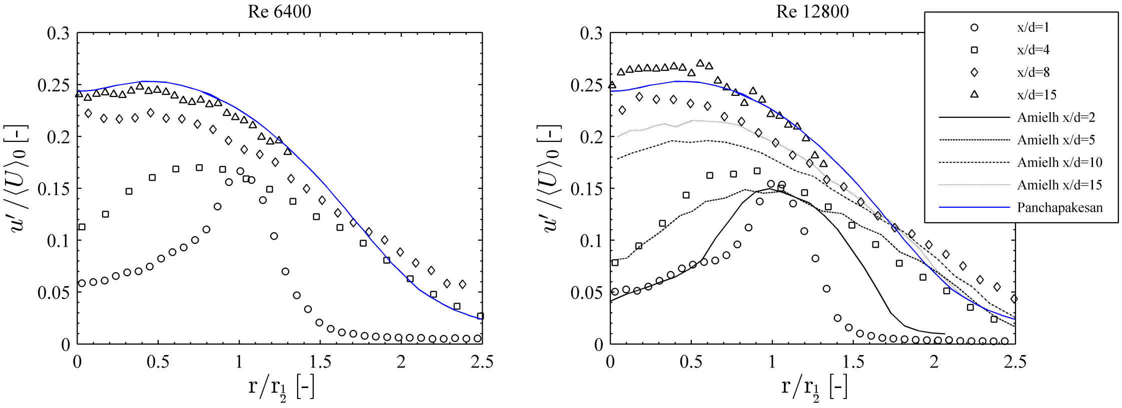

**Figure 6.10.:** Radial profiles of normalized rms of axial velocity, $u'/\langle U \rangle_0$.

In figure 6.10 and 6.11, radial profiles of normalized rms of axial and radial velocities at different axial positions are shown. The overall evolution of radial profiles downstream was in good agreement with Amielh et al. [5], who measured velocity fields of un unheated air jet (density ratio, 1) using Laser Doppler Anemometry. In [5] and this study, an intense peak at x=1d or 2d position existed for the high shear between jet and co-flow. The flow in these positions is close to the fully developed pipe flow and keep on adapting itself to the changed boundary condition, therefore the shape is much different to the self-preservation one. This intense peak was gradually weakened downstream, and the position of the peak moved closer to the jet center. The radial profiles of normalized rms of the velocities appear to have almost approached the self-preservation at x=15d, but not yet completely, especially in Re 6400 case. Unfortunately, in the high Re case, an effect of an uncontrolled experimental boundary condition is suspected to cause higher intensity than expected self-preserving state. However, its effect on the general findings of the present context is minimal. The development of the jet in [5] is expected to be slower than this study for the higher density ratio, thus at x=15d, the jet appears to be less developed than within the present study. The similar findings were applied to the rms of radial velocity in figure 6.11.

In the left of figure 6.12, the radial profiles of the normalized rms of scalar at different downstream are shown with the results of Lockwood & Moneib [55] and the profile of

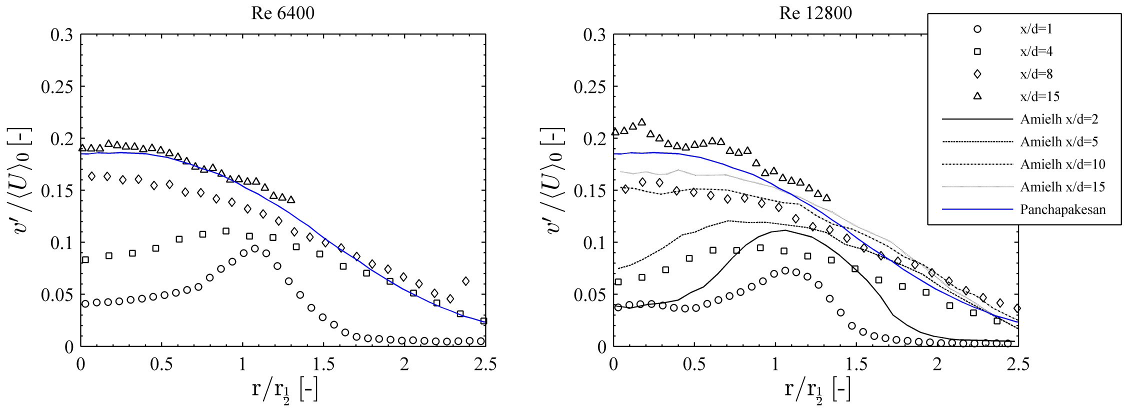

**Figure 6.11.:** Radial profiles of normalized rms of radial velocity, $v'/\langle U\rangle_0$.

self-preservation from Panchapakesan [72]. Similar with the tendency of the rms of the velocity components, the normalized rms of the scalar showed an intense peak at x=1d, which were gradually smoothed. The similar observation was found in [55], although they did not show the result early upstream. Thus, no distinct peak was observed. The profile approached to the self-preservation as another variables, but has not reached it yet. The shape of the profile at x=15d, however, is different with the one of velocity component. While the scalar rms profile has a rather outstanding peak around r/r$_{\frac{1}{2}}$=0.8, the velocity rms profile has vague peak close to the jet center.

It has been common in a measurement of rms value to separate the fluctuation from the turbulence and the one from a measurement uncertainty, e.g., [53]. In the present study the camera error was regarded as a main source of error, and the error estimation based on the error propagation was given in equation 3.1. By using average signal and measured calibration curve, expected camera error, $\sigma_T$ was calculated, and a corresponding rms of scalar, $\sigma_\theta$ was calculated by dividing $\sigma_T$ with $(T_h - T_c)$. Assuming no correlation between the camera error and fluctuations by turbulence, the measured rms of scalar $\sigma_m$ is

$$\sigma_m^2 = \sigma_\theta^2 + \sigma_t^2, \tag{6.4}$$

similar to equation 5.1. Here, $\sigma_t^2$ is the variance by the turbulence. One can reasonably argue that the rms of 2 % in co-flow region at x=1d in figure 6.12 is mainly coming from camera error in a first glance. In low temperature, the signal in the blue channel is relatively week and a strong camera error is likely to occur. However, as evident in the right of figure 6.12, the contribution of the camera error based on our estimation was not significant. Therefore, it is more reasonable to accept the measured fluctuations were coming from the turbulence. Unintentional heating of the co-flow to around 315 $K$ by the hot tube can account for the scalar fluctuations. The heated air induced the natural convection in the nozzle of the co-flow and hence the amount of fluctuation there.

### 6.2.4. Two point spatial correlation and integral length scales

Based on the assumption of stationary, homogeneous, and isotropic turbulence, meaningful scales of turbulence could be extracted by two-point spatial correlation [69]. The

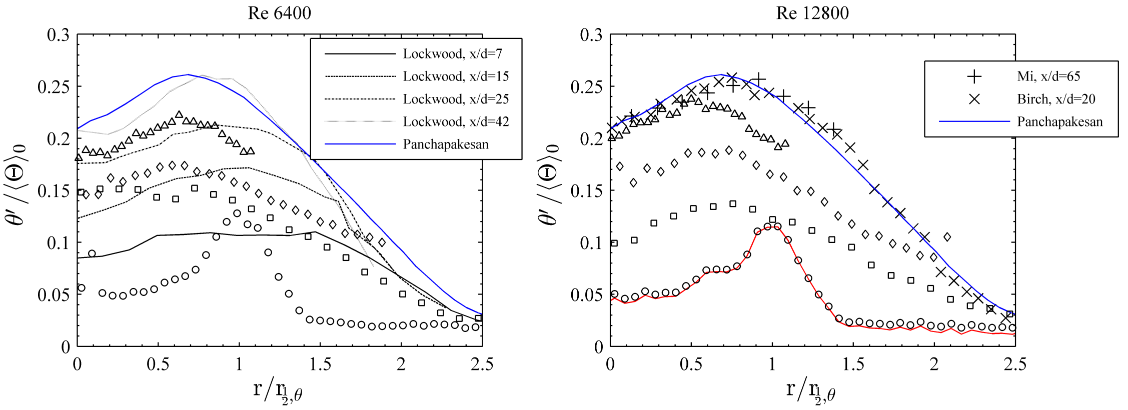

**Figure 6.12.:** Radial profiles of normalized rms of scalar, $\theta'/\langle\Theta\rangle_0$. The red solid line denotes normalized scalar fluctuation considering the camera error, $\sigma_t$ in equation 6.4.

measurement of the spatial correlation, however, is limited to the field of view of the measurement. The longitudinal distance of the field of view in this study was shorter than the lateral one, although the longitudinal correlation in a jet is typically around two times longer than the lateral one. Therefore, only the lateral correlation is considered in the following. The lateral correlation of axial velocity is defined as,

$$R_{uu,2}(x,r,s) = \frac{\langle u(x,r)u(x+s,r)\rangle}{u'(x,r)u'(x+s,r)}. \tag{6.5}$$

The correlations calculated by equation 6.5 are shown in figure 6.13. It was apparent

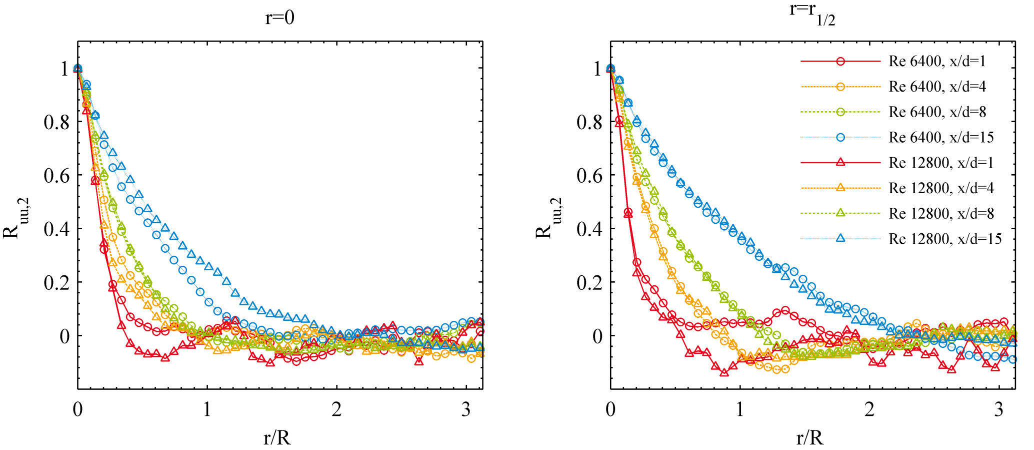

**Figure 6.13.:** Lateral two-point spatial correlations of axial velocity, $R_{uu,2}$.

from figure 6.13, that in most cases the different Re has little affected on the correlation. This was predicted because the correlations are linked to the size of most energetic or largest eddies. The size of the largest eddies are more linked to the jet half width [92], which are very similar between different Re (See table 6.2). By integrating the correlation, the lateral integral length scale, $L_2$ is obtained. The correlation was integrated until the correlation value became 0.05.

$$L_2(x,r) = \int_0^{s_1} R_{uu,2}(x,r,s)\mathrm{d}s$$

here, $R_{uu,2}(x,r,s_1) = 0.05$. The integral length scales extracted from the correlations are summarized in figure 6.14 and table 6.3. Wygnanski & Fielder [92] reviewed former studies on the integral length scales in the near-fields and also measured the scale in the self-preserving region. According to them, in the near-fields, the integral length scale normalized with $r_{\frac{1}{2}}$ increases rapidly in the mixing layer, but the increase is decelerated and even decreased in the far-fields and approaches to the self-preserving state. These findings are also evident from the result of this study. In figure 6.14, the integral length at $r=r_{\frac{1}{2}}$ was rapidly increased from x=1d to 4d position, which indicated that the integral scale grow rapidly in mixing layer of near-fields. ($r_{\frac{1}{2}}$ did not increase much in this range, see table 6.2). In further downstream, the shape was being adjusted towards the one of the self-preservation, however, did not reach it. The ratio of the size of the largest eddy to the jet half width, $L_2/r_{\frac{1}{2}}$ was bigger than the asymptotic value. These are illustrated in figure 6.15. Values are normalized with the one from the self-preservation (0.16 at r=0 and 0.3 at $r=r_{\frac{1}{2}}$) from [92]. This might be interpreted as the jet was not spread enough, considering size of largest eddy. Another observation, that the integral length scale was developing to self-preservation, is the ratio of the scale at center to the scale at mixing length. From [92], the value is 0.53 and it could be observed that the measurement in this study was approaching to the value as shown in figure 6.16.

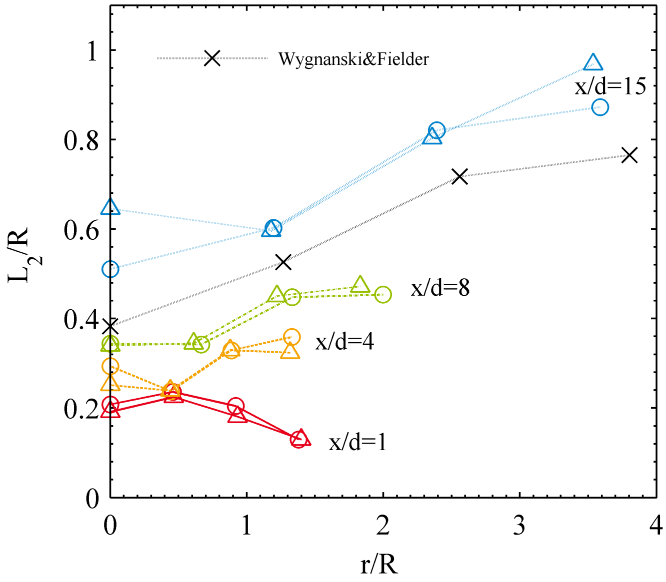

**Figure 6.14.:** Lateral integral length scales at different radial positions, r=0, 0.5, 1, 1.5$r_{\frac{1}{2}}$. See figure 6.13 for the notation.

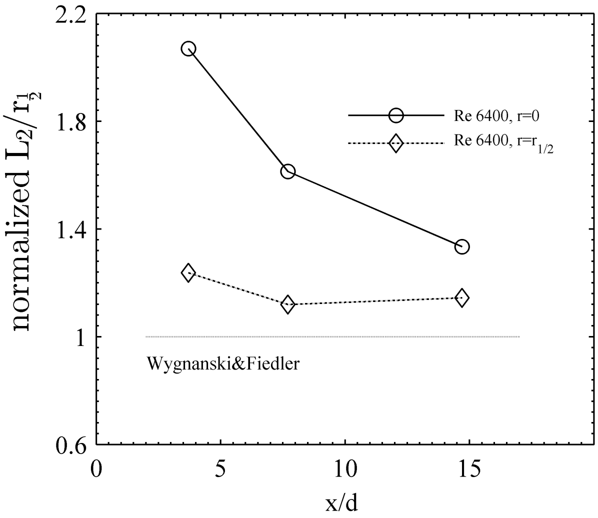

**Figure 6.15.:** Streamwise evolution of scaled lateral integral length scales,$L_2/r_{\frac{1}{2}}$ at jet center (r=0) and mixing layer($r=r_{\frac{1}{2}}$). Normalized with asymptotic value from Wygnanski, 0.16 at r=0 and 0.3 at $r=r_{\frac{1}{2}}$

### Second order moments

In the momentum and energy equation, the terms $\langle uv\rangle$, $\langle v\theta\rangle$ represent the transport of momentum and energy by turbulence and are denoted by Reynolds shear stress and turbulent scalar flux. The measured Reynolds shear stress in this study is shown in figure 6.17. A similar observation from $u'$,$v'$,and $\theta'$ were found. The eddies generated by strong shear force in upstream were represented by the intense peak at x=1d position, and the peak were moderated with smoothed radial gradient of axial mean velocity in downstream. The shift of the peak to the center stems from the interaction of generation of the eddies by

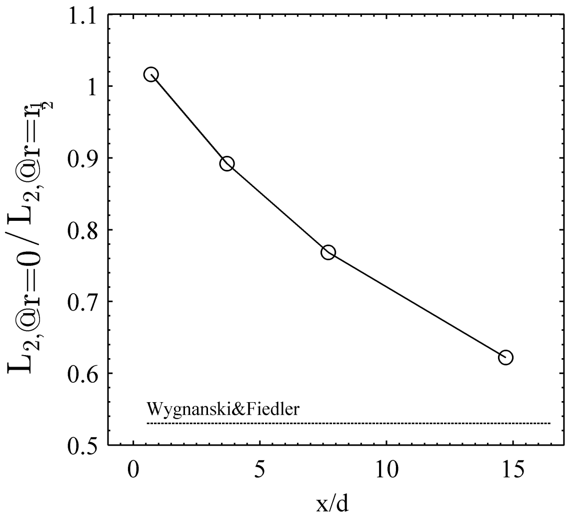

**Figure 6.16.:** Integral length scale ratio at jet center (r=0) and mixing layer($r=r_{\frac{1}{2}}$).

**Table 6.3.:** Summary of lateral integral length scales

| | | $L_2$ *[mm]* | | | |
|---|---|---|---|---|---|
| | $x$ | $r$=0 | $r$=0.5$r_{\frac{1}{2}}$ | $r$=$r_{\frac{1}{2}}$ | $r$=1.5$r_{\frac{1}{2}}$ |
| Re 6400 | 1d | 1.66 | 1.87 | 1.64 | 1.04 |
| | 4d | 2.35 | 1.90 | 2.63 | 2.87 |
| | 8d | 2.75 | 2.74 | 3.58 | 3.63 |
| | 15d | 4.08 | 4.82 | 6.57 | 6.98 |
| Re 12800 | 1d | 1.53 | 1.80 | 1.45 | 1.04 |
| | 4d | 2.01 | 1.91 | 2.63 | 2.59 |
| | 8d | 2.72 | 2.75 | 3.60 | 3.78 |
| | 15d | 5.16 | 4.77 | 6.43 | 7.75 |

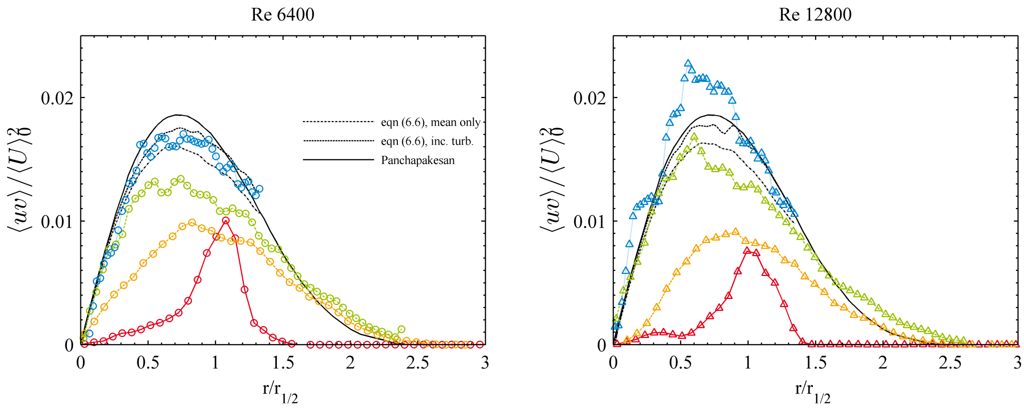

**Figure 6.17.:** Radial profiles of normalized Reynolds stress. See figure 6.13 for the notation.

shear force, transport, and the dissipation by viscosity. While adjusting to the boundary condition of quiescent ambient, the profiles approaches to the self-preserving one, but not reached it yet.

To demonstrate the goodness of the measurement, one can use mean and Reynolds normal stresses to calculate Reynolds shear stress with following equation, assuming that the flow has reached the self-preservation. Several studies e.g., [40], [71], also used this method.

$$\frac{\langle uv\rangle}{\langle U\rangle_0^2} = \frac{1}{\eta}\frac{\langle U\rangle}{\langle U\rangle_0}\int_0^{\eta}\frac{\langle U\rangle}{\langle U\rangle_0}\eta' \mathrm{d}\eta' + \eta\left(\frac{\langle u^2\rangle - \langle v^2\rangle}{\langle U\rangle_0^2}\right) \tag{6.6}$$

here, $\eta = r/x$. In figure 6.17, calculation of $\langle uv\rangle$ in x=15d position considering only the mean velocity and mean and normal stresses are shown. In low Re case, the calculation with turbulence showed good agreement with the measurement. In high Re case, however, the measurement showed large discrepancy with the profile of self-preservation and also with the calculations. It is suspected that the uncontrolled boundary condition affected the high Re case, therefore, the data in the low Re case was regarded as more reliable.

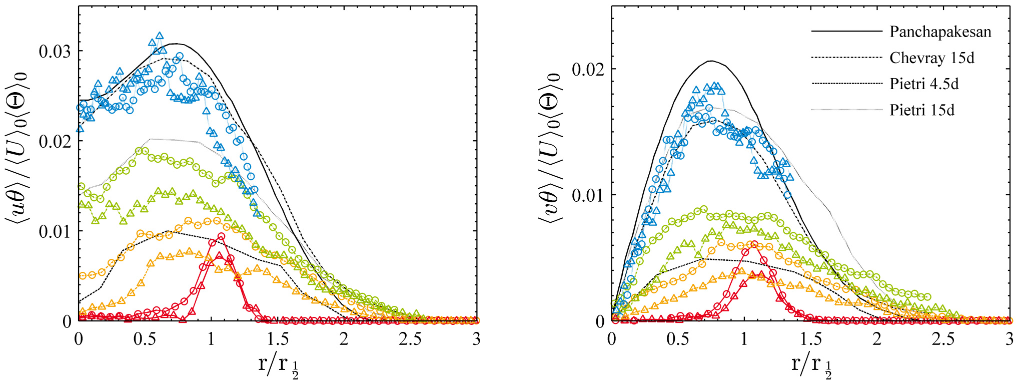

**Figure 6.18.:** Radial profiles of normalized scalar fluxes. See figure 6.13 for the notation.

The scalar fluxes are shown in figure 6.18. Similar development to the Reynolds shear stress were observed. The axial flux was larger than the radial one, and the peak of the axial flux were closer to the center than the radial one. Pietri et al. [67] measured the scalar flux in a heated round jet by cold wire and laser Doppler anemometry and the results are shown together in figure 6.18. When compared to their results, a very similar tendency was indicated, but the jet in their work appears to develop slower. This might be attributed to their higher density ratio (0.95) compared with this study. Chevray and Tutu [70] measured the scalar flux at x=15d position and show good agreement with the case of low Re in this study. Again, however, high Re case show a slightly lager scatter. Comparing to the profile of self-preservation from [72], it could be accepted that the scalar fluxes did not reach the self-preservation. In this study, the mean profile reached the self-preservation first, and the second momentum appeared to reach in the last.

## 6.2.5. Turbulence models

A closure problem exists in solving the equations 6.1 - 6.3. Four unknowns, $\langle U\rangle$, $\langle V\rangle$, $\langle uv\rangle$, and $\langle v\theta\rangle$ present in given three equations. To close $\langle uv\rangle$, and $\langle v\theta\rangle$, various models of turbulence have been developed, and the turbulent-viscosity and the gradient-diffusion models among them are here introduced.

By the turbulent-viscosity model, the Reynolds shear stress in a shear flow is expressed as,

$$\langle uv\rangle = -\nu_t \frac{\partial\langle U\rangle}{\partial r}, \tag{6.7}$$

here $\nu_t$ is called turbulent viscosity or eddy viscosity. Similarly, the scalar flux is expressed as gradient of mean scalar,

$$\langle v\theta\rangle = -\alpha_t \frac{\partial\langle\Theta\rangle}{\partial r} \tag{6.8}$$

These simple models would have been implemented in various flows, if they could predict the turbulent transports accurately in applied flows. Unfortunately, however, their predictions generally deviate from the correct solutions in the most of the cases. The inaccuracy of the models stems from the assumption that the models have. Basically, the turbulent-viscosity model is an analogy to the molecular diffusion in Newtonian fluid, and the gradient-diffusion to the Fick's law of molecular diffusion (or Fourier's law of thermal diffusion). If the eddies behave similarly to molecules, the analogy would success. However, while the molecules adapt fast to the imposed straining, the eddies persist and need time to adapt to it. This is the reason why the performance of the model is poor in the most of the flows.

The model, nevertheless, is justified in simple shear flow e.g., jet flowing into quiescent ambient because the flow does not experience the rapidly changing boundary conditions. In this condition, local generation and dissipation are comparable and non-local transports is negligible. Therefore, the local gradient of the mean could be related with the Reynolds stress or scalar flux [69].

After calculating the radial gradient of mean axial velocity, $\frac{\partial \langle U \rangle}{\partial r}$, the turbulent viscosity, $\nu_t$ could be extracted by dividing the $\langle uv \rangle$ with the gradient (equation 6.7). The radial gradients of axial mean velocities are shown in figure 6.19. The same property measured by Pietri et al. [67] at x=4d and 15d positions are shown together. The measurements show general agreement with the present results. The central difference scheme was applied

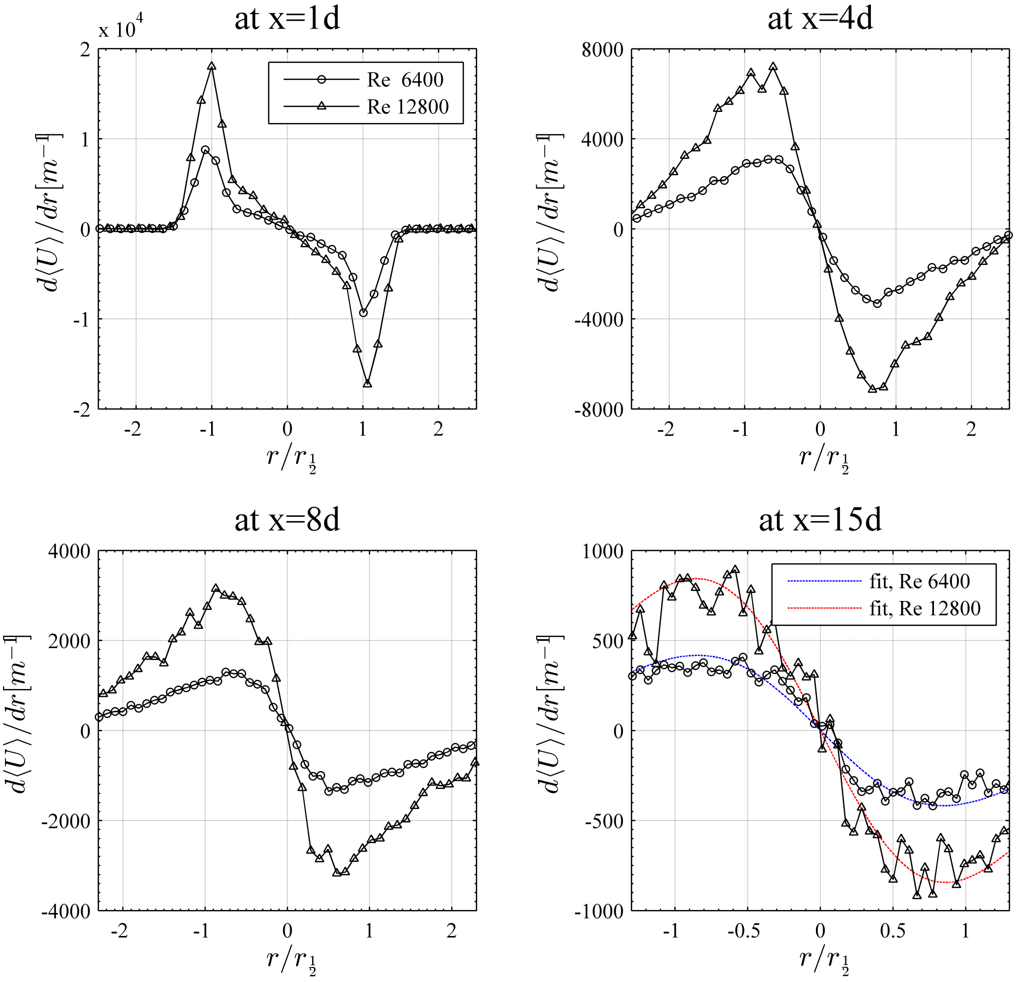

Figure 6.19.: Radial gradients of mean axial velocities.

directly to the measured mean profile except x=15d position. At the position, the mean profiles were first fitted with the one of self-preservation, and then the mathematical differentiation was applied. The numerical differentiation generated too large error to deduce meaningful interpretation in the position. The normalized turbulent diffusivity with center velocity and jet half width, $\nu_t/\langle U\rangle_0 r_{1/2}$ are shown in figure 6.20. In equation 6.7, both $\langle U\rangle$ and $\langle uv\rangle$ are self-preserving in far-field, thus $\nu_t$ is evidently self-preserving in far-field. The profile of self-preservation from Hussein et al.[2] [40] is also shown in figure 6.20. At x=15d, the turbulent diffusivity was close to the self-preserving case, but not reached it yet. The normalized turbulent diffusivity is quasi-homogeneous (15 % of 0.028 [69]) in the range of $0.1 < r/r_{\frac{1}{2}} < 1.5$ in self-preserving state, however, as shown in this study, it is function of the position in the developing region.

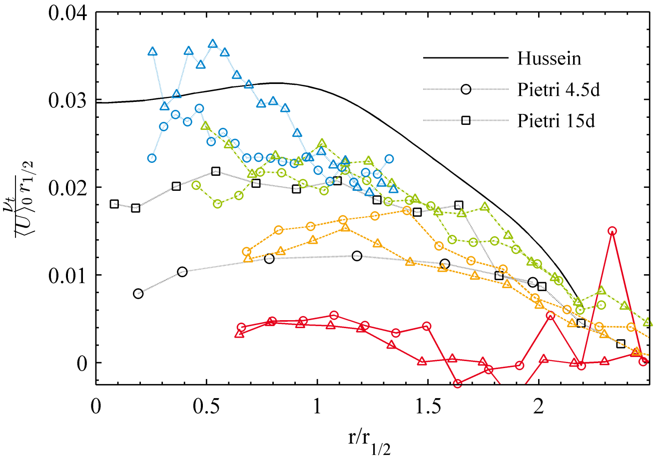

**Figure 6.20.:** Normalized turbulent viscosity, $\nu_t/\langle U\rangle_0 r_{1/2}$. See figure 6.13 for the notation.

Similar to the turbulent viscosity, turbulent diffusivity could be extracted after calculating the radial gradient of the mean scalar. As applied to the gradient of the mean velocity, the central difference scheme was applied directly to the measured mean scalar profile to obtain the gradient except at the x=15d position, where the gradient was calculated mathematically from the fitting of the self-preserving one. The gradients are shown in figure 6.21. Based on the gradient, the normalized turbulent diffusivity was calculated as shown in figure 6.22. The tendency of turbulent diffusivity was very similar with turbulent viscosity. The results from Pietri et al. [67] are shown together and showed general agreement. From the measurement of this study, the applicability of the models in the jet flow was confirmed one more time. The turbulent transports of momentum and scalar were correlated with the gradient of the mean, and the correlation was represented as turbulent viscosity or diffusivity, respectively. If the models were invalid, arbitrary values would be extracted for the turbulent diffusivity and viscosity.

The gradient diffusion model, however, can not predict the direction of the scalar flux vector. Generally, the scalar flux is a vector in two dimensional flows and expressed as

$$(\langle u\theta\rangle, \langle v\theta\rangle) = -\alpha_t \left(\frac{\partial\langle U\rangle}{\partial x}, \frac{\partial\langle U\rangle}{\partial r}\right) \tag{6.9}$$

---

[2] The self-preserving profile of $\nu_t$ was extracted from Pope [69]. He calculated the profile from self-preserving profile of $\langle U\rangle$ and $\langle uv\rangle$ in [40].

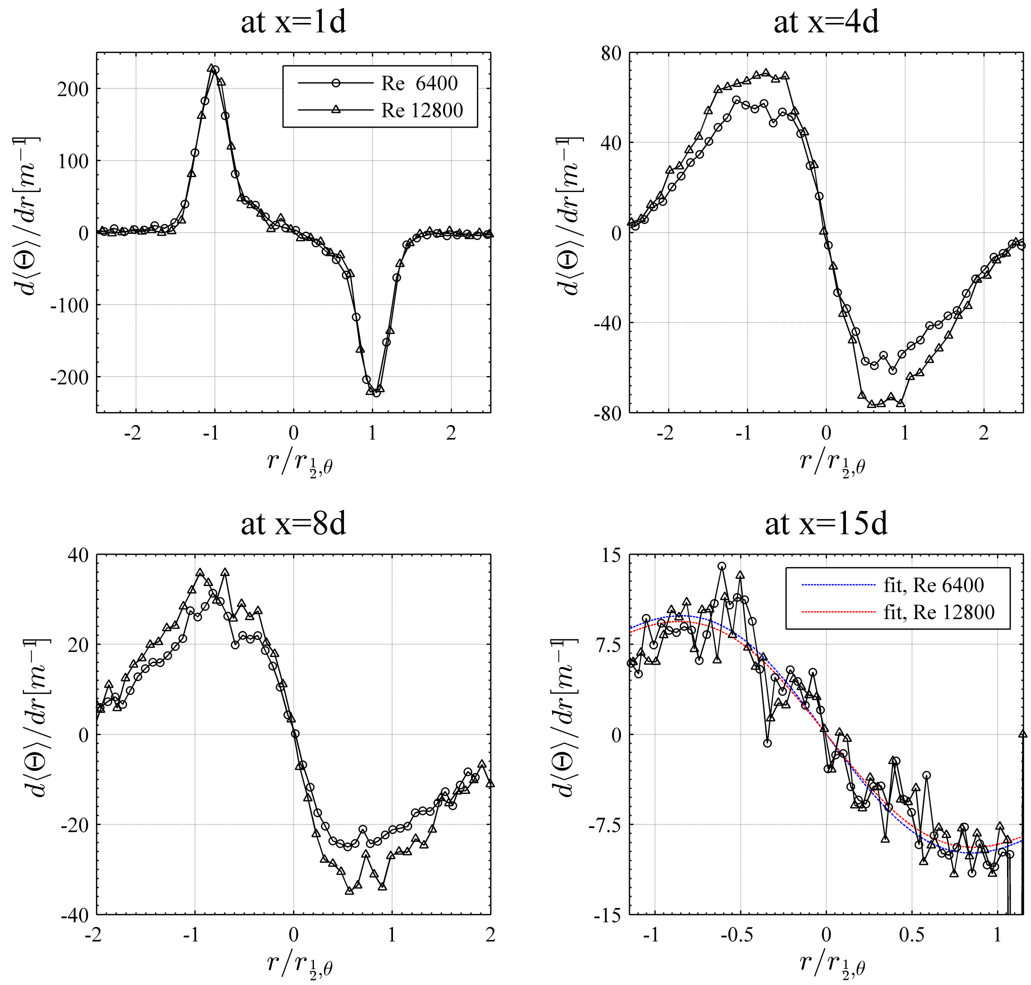

**Figure 6.21.:** Radial gradients of mean scalar.

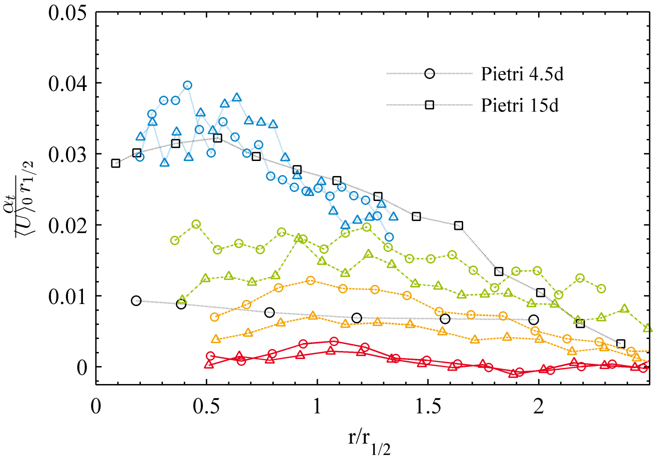

**Figure 6.22.:** Normalized turbulent diffusivity, $\alpha_t/\langle U\rangle_0 r_{1/2}$. See figure 6.13 for the notation.

by the gradient-diffusion model. In equation 6.3, $\langle u\theta \rangle$ was disappeared by boundary layer approximation because axial difference of the term was negligible. Although the contribution of the axial scalar flux, $\langle u\theta \rangle$ to the mean scalar is negligible, the magnitude of $\langle u\theta \rangle$ is larger than $\langle v\theta \rangle$ in the jet (see figure 6.18). The limitation of the gradient-diffusion model in predicting the direction of the scalar flux is expressed in figure 6.23.

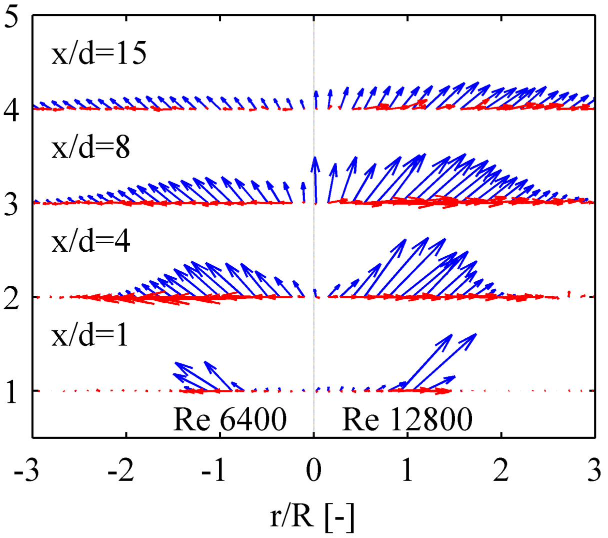

**Figure 6.23.:** Measured scalar flux vector and the one from the gradient-diffusion model. The blue arrows denote the directly measured scalar flux and the red one denote the one from the gradient-diffusion model.

In all positions, the model could not predict the direction correctly. This was also reported by [84] for homogeneous shear flow as referred in [69]. He found an angle of 65° between the scalar fluxes by the measurement and the model.

The ratio of turbulent viscosity and diffusivity, turbulent Prandtl number is defined as

$$Pr_t = \frac{\nu_t}{\alpha_t}. \tag{6.10}$$

The turbulent Prandtl number at x=15d position in this study is shown in figure 6.24 with the one from Chevray & Tutu [70] and from Pietri et al. [67]. The turbulent Prandtl number increased slightly in the outer region of the jet. Again, the result in the present study showed a general agreement with the previous ones.

### 6.2.6. Conclusion

Thermographic PIV was applied to the developing region of heated round jet, and the results were compared with the previous results validating the measurement technique. The

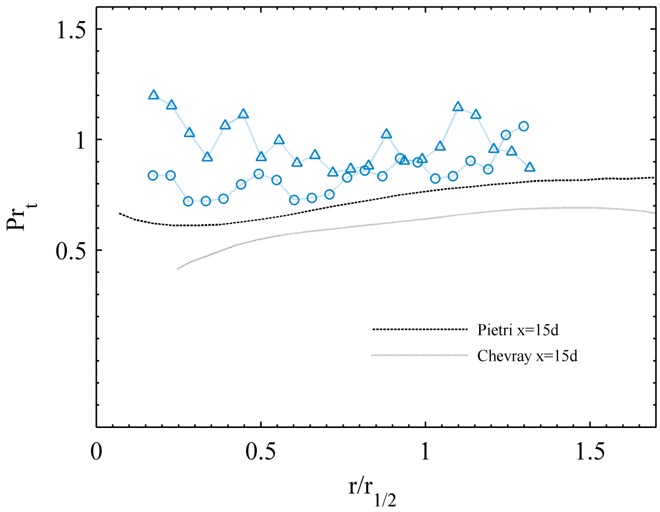

**Figure 6.24.:** Turbulent prandtl number. See figure 6.13 for the notation.

measurements of velocity by PIV, and the information extracted from the results, showed agreement with the one by the pointwise measurement (e.g., LDV, hot wire anemometry), which is regarded accurate. The mean and rms of velocity and the spatial correlation and the Reynolds stress indicated reasonable results. Through those result of velocity, the general structure of the flow in this study could be assured. The scalar field showed a good agreement with the velocity field and the previous results. Moreover, the measurement of scalar flux was successful and an assessment of the gradient-diffusion model could be applied. The extracted turbulent viscosity, diffusivity and the Prandtl number showed the agreement with the previous studies. All of the above demonstrated the feasibility of the technique in the simultaneous velocity and temperature measurement. The measurement technique is already applicable to similar configurations, such as the wake after heated cylinder [2], impinging jet to the wall [43].

The free jet, however, is relatively simple configuration for the measurement; there is neither confinement, which will cause the particles to be stuck and emit strong background etc., nor the flame, the strong chemiluminescence. The measurement in jet in crossflow configuration has been attempted in this study. The preliminary result will be present as an outlook in chapter 7.

# Chapter 7.

# Conclusion and outlook

The present work is summarised as (1) investigating prospective phosphors in oven, (2) error analysis on gas temperature measurement, (3) and the scalar flux measurement in the developing region of heated round jet.

**Investigating phosphors** The way to evaluate a phosphor for gas thermometry application has been proposed in terms of the temperature sensitivity and the signal intensity. This method can produce relatively reliable prediction considering the required effort of the experiment. On the contrary, the method proposed by [27] can produce a more accurate assessment, but require a relatively consequent experimental effort. In author's opinion, the method might be quite demanding that the exploration of the vast inventory of prospective phosphors might not be practically possible. Therefore, using the method proposed in the present study can facilitate to find the potential candidates and detail characterization of selected phosphor could be followed later. Finding new phosphor will extend the application to the desired temperature range. Eight phosphors were evaluated in the oven and using LED phosphors, SRMG, BAM:EuMn can simplify the measurement setup by using the same excitation source for the Mie-scattering and the phosphorescence. The phosphors from the various applications, such as the LED phosphors, the display phosphors, etc. are required to be assessed further. Furthermore, the developed filter optimization scheme could serve to guide the design of other phosphors in the future.

As the future works regarding the characterization process in the oven, understanding on the discrepancy between packed powder and individualized particles ought to be deepened. The study will include the multiple scattering effect in packed powder and help interpretation of the spectra measured in the oven in the context of gas thermometry application. As another improvement, the automation of the spectra measurement will facilitate the experiment and accelerate the increase rate of the number of investigated phosphors. For example, when the oven is either heated or cooled, the phosphor sample is posed inside the oven. The thermocouple temperature is monitored continuously and also the spectra at the temperature. To minimize the damage by the excitation, a mechanical shutter can be used being controlled by the software. The reflected light of Glan polariser can be continuously monitored to assure the laser energy used. By comparing the spectra of heating and cooling phase of the oven, it is expected to partly evaluate the effect of thermal exposure. Nada et al. showed similar approach to characterize lifetime of phosphor in the oven in [62].

**Systematic analysis on possible sources of errors** Two types of error sources were analysed in the present study: the effect of laser fluence, which could be generally applied, and the effect of seeding density, which was specific to the experimental setup in this study.

A shift without significant broadening to UV regime has been observed from the spectra of packed BAM powder according to increasing laser fluence, and increasing intensity ratio from individualized particles. The influence was weakened in high temperature in both cases. The tendency has been conjectured to stem from the influence of varying crystal fields with increasing number of excited activators based on the spectra measurement in the oven. The crystal field might be weakened for increased number of the activators in interaction. It was suggested to use a homogeneous beam for the thermometry to avoid an unnecessary systematic error.

As the next investigated error source, the effect of seeding density has been analysed. The significance of multiply scattered light from the co-flow region has been evaluated, and it was suggested to sort out the images with seeding density ratio smaller than two. In the present study, a relatively large volume has been seeded than the previous ones, thus, the effect of seeding density has been accentuated. However, it is worth to mention that seeding this amount of volume shall be confronted when the technique is applied to gas turbine combustor or internal combustion engine. This kind of consideration would be required in the future applications. The preferential absorption has been also suggested, but confirming its effect was out of the scope of the present study. Using e.g., SLIPI might prove the presence of the preferential absorption.

At the moment, the measurement technique requires the in-situ calibration measurement. This limitation causes difficulties of the measurement technique for some applications. A profound and systematic understanding of factors affecting the intensity ratio might free the measurement technique from this limitation. At the moment, the influence of laser fluence, seeding density have been at least vaguely understood. Further investigation on the angle of incidence, the effect of background and etc. is on demand.

**Scalar flux measurement in axisymmetric jet development** By measuring velocity and temperature simultaneously in the developing region of heated round jet, the measurement technique has been firmly validated. Comparison of the mean, the fluctuation, and the correlation of the variables with previous results complemented the feasibility of the measurement technique, which has been demonstrated for last half decades. Not only proving the technique, but the results indicated also the characteristic of the canonical configuration; the evolution of jet to the self-preservation.

**Jet in crossflow configuration** The measurement technique is validated in a jet with co-flow configuration to produce a reliable measurement of velocity and temperature, thus the application of the technique to the complex systems should be followed. The jet in crossflow configuration is relevant to various engineering systems such as fuel mixing or film cooling of the gas turbine. Consequently, this configuration has been subjected plenty of studies. The measurement of scalar flux in the jet in crossflow configuration has been attempted in the study, but could not be completed. Here, the general concept of the measurement setup, preliminary results and revealed issues in the specific setup are introduced briefly.

The crossflow was generated by a square-shaped contraction nozzle (contraction ratio: 9, nozzle length: 150 $mm$, nozzle outlet area: $40 \times 40$ $mm^2$) and the flow direction was upright. A channel, of which three walls include optically accessible quartz window (for excitation and imaging), was connected to the outlet of the nozzle. One wall was connected with a narrow pipe for the generation of a jet. Each wall of the channel is detachable that the complete channel could be removed except the wall with the pipe for the jet. Closed configuration (with four walls) resembles the real applications e.g., gas combustor, but suffers from particle sticking, and the stray light. The influence of background, such as reflection, elastic scattering of excitation, phosphorescence emitting from the stuck particle, was strongly expected inside the confinement. By contrast, the open configuration is relatively free from the background, but the flow will be influenced by the entrained air from the ambient. In the present study, all the measurement was performed in the open configuration first to facilitate the measurement.

The diameter of the jet is 2 $mm$ and the length of the pipe is around 20 $mm$. The jet was heated to 500 $K$ by an electric heater and the Re was around 3000 based on the bulk velocity. The effective velocity ratio, which considers the effect of the density, was 5.7. The whole system stand on a translation stage (LINOS, XY 200-50) so that the system can translate 50 $mm$ with 10 $\mu m$ precision in the horizontal directions and also 140 $mm$ in the vertical direction by using additional translation stage.

The optical setup was the same as the one for the jet with co-flow configuration, but a dichroic beamsplitter was used instead of 50:50 beam splitter to collect more signal. In the ahead of the beamsplitter, an achromatic lens ($\phi$=50 $mm$, $f$=200 $mm$, 450 - 700 $nm$ AR coated in the backside) was placed in its focal length from the object plane (laser sheet) to collect and collimate the emission. 85 $mm$ f# 1.4 lenses, which were stopped at f#=2, were mounted to the camera securing the full aperture of the achromatic lens. The magnification was 0.425.

Exemplary images of a blue and a red channel are shown in figure 7.1. The origin of the coordinate placed in the outlet of the jet. The field of view starts at 3 $mm$ away from the jet outlet. In this case, enough particles were seeded into the jet, but very rare particles were seeded into the crossflow. Accordingly, the effect of the multiple scattering from the cold crossflow to the jet was expected to be negligible.

However, when there were densely seeded particles in the crossflow, the effect of multiple scattering was severe. The estimation of the effect of multiple scattering in this configuration could be indicated by the evolution of intensity ratio at jet outlet according to the seeding density in crossflow. The intensity ratio at the jet outlet was graphed according to the seeding density ratio of the jet and crossflow in figure 7.2. In the present analysis, no particle locating algorithm (Section 3.2.3) has been used, but the signal intensity at the region of the jet and the crossflow were divided by signal per particle obtained previously. The intensity ratio drastically decreased with decreasing seeding density ratio, which means more consequent multiple scattering effect than the jet with co-flow configuration (compare with figure 5.9). A very quick assumption is that the effect is related to the volume ratio of the jet and co-flow or crossflow. In the jet with co-flow configuration, the diameter ratio of jet and co-flow is $140/16 = 8.75$ and the one for the jet in crossflow is $40/2 = 20$. The ratio of cold and hot fluid in length is two times larger in the jet in crossflow case. Therefore, the volume ratio will be $2^3$ larger, and thus, the

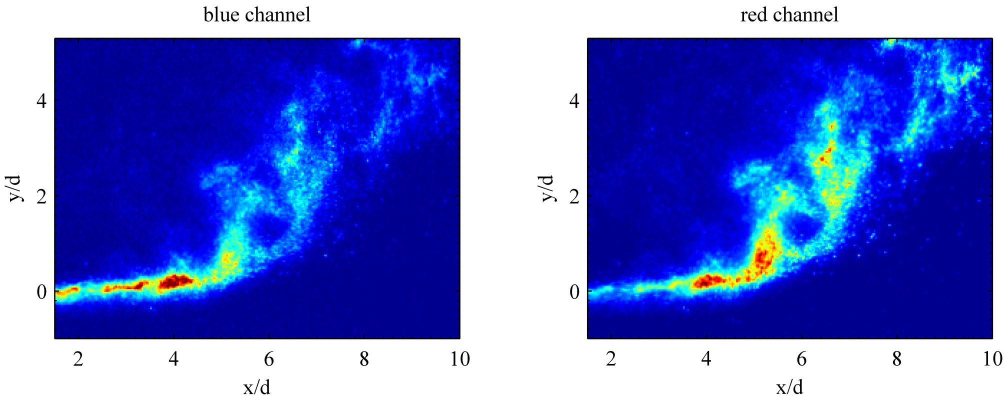

**Figure 7.1.:** Instant phosphorescence image of blue and red channel demonstrated in false color.

multiple scattering effect of the cold flow is expected to be severer in the jet in crossflow configuration. This was a rough estimation and a detailed analysis should be followed with particle locating scheme later.

As the case of the jet with co-flow, to overcome the multple scattering without additional optical change, e.g., SLIPI, changing filter set, a compromised seeding density in crossflow, which is dense enough to produce a minimum signal, but dilute enough to minimize the multiple scattering effect, should be found. After that, the calibration curve ought to be attained by the images satisfying the seeding density conditions. However, for the time being, the calibration curve was obtained without seeding the crossflow. The measured intensity ratio at the jet outlet was related to the temperature measured by thermocouple for calibration curve in the steady states. After that, among the acquired images in the actual measurement, only the images with minimal crossflow seeding has been chosen and

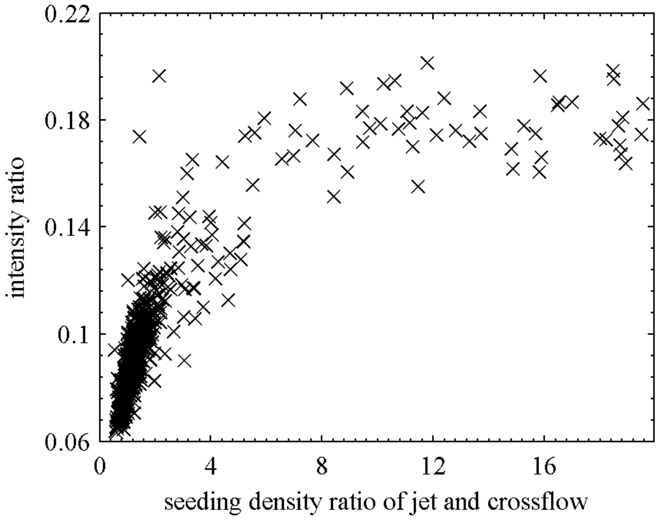

**Figure 7.2.:** The trend of intensity ratio according to seeding ratio of jet and crossflow.

processed further. The instant temperature from the images in figure 7.1 are shown on the left of figure 7.3 and the average temperature from 50 images satisfying the seeding density conditions are on the right. In the calculation of the temperature, the region with the signal smaller than 7 (two times of camera readout error) has been masked and no temperature was calculated.

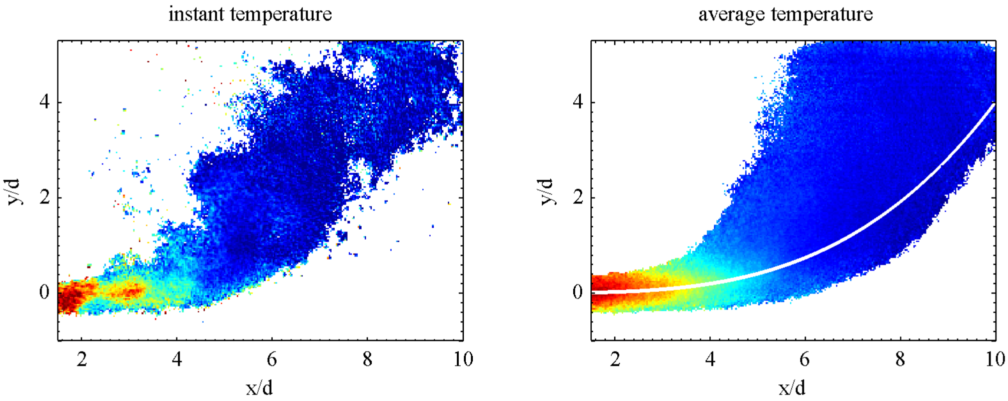

**Figure 7.3.:** Instant and mean temperature. The white solid line the right of figure denotes the least squre fit of [46]

In the instant temperature image, it could be qualitatively mentioned that the most of the structures that were seen in the phosphorescence image (figure 7.1) became unclear. The weak signal intensity is suspected to have induced a noise and make the structures not recognizable. As a matter of fact, there were mistake in the synchronizing the optic system in the measurement. The camera was exposed around 1 $\mu s$ later than the excitation, and possibly 40-50 % of signal has been lost. By replicating the experiment with right synchronization, the signal is expected to be larger and the structure to be discerned clearly. The mean temperature indicate agreement with previous findings qualitatively. The jet impinged further to the crossflow some jet diameter downstream and was bended by the crossflow. The scalar centreline from [46], which was defined as maximum mean scalar concentration, was drawn together in the figure 7.3 as solid white line, $x/r_{eff}d = 1.95(y/r_{eff}d)^{0.302}$, here $r_{eff} = 5.7$.

The preliminary results have shown promising performance of temperature measurement in the one hand, but also issues to be resolved in the other hand. The multiple scattering effect coming from large volume of cold crossflow need to be solved. The phosphorescence from cold flow lowered the intensity ratio of high temperature flow, hence the sensitivity on the temperature of the intensity ratio. The cause and the effect of multiple scattering should be scrutinized to obtain reliable results.

The phosphor particles stuck on the surface very quickly and could generate non-negligible effect on the intensity ratio. The particles on the surface emitted strong phosphorescence, especially when they were excited by the beam directly. The effect of this strong phosphorescence from wall on the intensity ratio of the near flow ought to be investigated. This influence can prevent the measurement near the wall, where the lack of particles already induce low signal to noise ratio. Furthermore, the effect of stuck particle is expected to become severer for the measurement in a confinement than an open configuration. The stray excitation light reflected inside of the confinement can excite the stuck particles on the wall and will produce the phosphorescence. The amount of the effect will vary according to the amount of stuck particles which will vary continuously during the measurement. These issues, stray light, stuck particles, and multiple scattering, are highly expected to be confronted in the application to the internal combustion engine or gas turbine combustor. In the present setup, which is simpler than those applications, the issues are to be resolved.

# Appendix A.

# Appendix

## A.1. Dynamic response of particle to the gas

An assessment on the traceability of a particle is essential in PIV because it stands on the fundamental assumption that the particle velocity is the same with the gas.

For this purpose, there have been two approaches: calculating relaxation time[73] and largest particle size to follow certain turbulent fluctuaion[57]. Here, the first approach is introduced.

For the small particles suspended in the gas phase, if the $Re << 1$ condition is satisfied, one can reasonably assume Stokes' flow. Based on this presumption, the Basset–Boussinesq–Oseen equation describes the unsteady motion of a particle suspended in the gas. Furthermore, when the density of the particle is much greater than the gas, the equation is more simplified[57].

$$\frac{\pi d_p^3}{6}\rho_p\frac{dU_p}{dt} = -3\pi\mu d_p(U_p - U_g)$$

here, no external force is considered. This equation is more simplified.

$$\frac{dU_p}{dt} = -\frac{18\mu}{\rho_p d_p^2}(U_p - U_g)$$

After separating variables and integrating from initial state $U_p = U_{p0}$ with the assumption of constant gas velocity, the particle velocity $U_p$ is rewritten.

$$\frac{U_p - U_g}{U_{p0} - U_g} = exp(-\frac{18\mu}{\rho_p d_p^2}t)$$

here we define relaxation time, $\tau_D \equiv \dfrac{\rho_p d_p^2}{18\mu}$.

# Bibliography

[1] Christopher Abram, Benoit Fond, and Frank Beyrau. High-precision flow temperature imaging using zno thermographic phosphor tracer particles. *Optics Express*, 23(15):19453, 2015.

[2] Christopher Abram, Benoit Fond, Andrew L. Heyes, and Frank Beyrau. High-speed planar thermometry and velocimetry using thermographic phosphor particles. *Applied Physics B*, 111(2):155–160, 2013.

[3] Marcus Aldén, Alaa Omrane, Mattias Richter, and Gustaf Särner. Thermographic phosphors for thermometry: A survey of combustion applications. *Progress in Energy and Combustion Science*, 37(4):422–461, 2011.

[4] S. W. Allison and G. T. Gillies. Remote thermometry with thermographic phosphors: Instrumentation and applications. *Review of Scientific Instruments*, 68(7):2615–2650, 1997.

[5] M. Amielh, T. Djeridane, F. Anselmet, and L. Fulachier. Velocity near-field of variable density turbulent jets. *International Journal of Heat and Mass Transfer*, 39(10):2149–2164, 1996.

[6] Peter W. Atkins and Julio de Paula. *Atkins' physical chemistry.* Oxford University Press, Oxford, 2014.

[7] Jerzy Bałdyga and John R. Bourne. *Turbulent mixing and chemical reactions.* Wiley, Chichester, 1999.

[8] Julius S. Bendat and Allan G. Piersol. *Random data: Analysis and measurement procedures.* Wiley series in probability and statistics. Wiley, Hoboken, N.J., N.J. : Wiley, 2010.

[9] G. Bizarri and B. Moine. On phosphor degradation mechanism: Thermal treatment effects. *Journal of Luminescence*, 113(3-4):199–213, 2005.

[10] D. J. Bizzak and M. K. Chyu. Rare–earth phosphor laser–induced fluorescence thermal imaging system. *Review of Scientific Instruments*, 65(1):102–107, 1994.

[11] George Blasse and B. C. Grabmaier. *Luminescent materials: With 31 tables.* Springer, Berlin [u.a.], 1994.

[12] B. J. Boersma, G. Brethouwer, and F. T. M. Nieuwstadt. A numerical investigation on the effect of the inflow conditions on the self-similar region of a round jet. *Physics of Fluids(1994-present)*, 10(4):899–909, 1998.

[13] L. Boguslawski and Cz. O. Popiel. Flow structure of the free round turbulent jet in the initial region. *Journal of Fluid Mechanics*, 90(03):531–539, 1979.

[14] Craig F. Bohren and Donald R. Huffman. *Absorption and scattering of light by small particles.* Wiley science paperback series. Wiley, New York [u.a.], 2004.

[15] J. Brübach, J. P. Feist, and A. Dreizler. Characterization of manganese-activated magnesium fluorogermanate with regards to thermographic phosphor thermometry. *Measurement Science and Technology*, 19(2):25602, 2008.

[16] Jan Brübach, Christian Pflitsch, Andreas Dreizler, and Burak Atakan. On surface temperature measurements with thermographic phosphors: A review. *Progress in Energy and Combustion Science*, 39(1):37–60, 2013.

[17] Yan Chen, Jing Wang, Xinguo Zhang, Gongguo Zhang, Menglian Gong, and Qiang Su. An intense green emitting lisrpo4:eu2+, tb3+ for phosphor-converted led. *Sensors and Actuators B: Chemical*, 148(1):259–263, 2010.

[18] Noel T. Clemens. Flow imaging. *Encyclopedia of imaging science and technology*, 2002.

[19] John Collins. Luminescence spectroscopy of solids: localized systems. In Baldassare Bartolo and Ottavio Forte, editors, *Advances in Spectroscopy for Lasers and Sensing edited by Baldassare Bartolo, Ottavio Forte*, pages 129–155. Springer Netherlands, Dordrecht, 2006.

[20] A. D. Birch, D. R. Brown, M. G. Dodson, and J. R. Thomas. The turbulent concentration field of a methane jet. *Journal of Fluid Mechanics*, 88(03):431–449, 1978.

[21] Dorian Liepmann and Morteza Gharib. The role of streamwise vorticity in the near-field entrainment of round jets. *Journal of Fluid Mechanics*, 245:643–668, 1992.

[22] Paul E. Dimotakis. The mixing transition in turbulent flows. *Journal of Fluid Mechanics*, 409:69–98, 2000.

[23] M. Euler, T. Kissel, A. Dreizler, and J. Brübach. The spectrally resolved luminescence decay of thermographic phosphors. *Measurement Science and Technology*, 22(8):83001, 2011.

[24] J. P. Feist and A. L. Heyes. The characterization of y2o2s:sm powder as a thermographic phosphor for high temperature applications. *Measurement Science and Technology*, 11(7):942, 2000.

[25] J. P. Feist, A. L. Heyes, K. L. Choy, and B. Su, editors. *Phosphor thermometry for high temperature gas turbine applications*, 1999.

[26] H. Fellouah, C. G. Ball, and A. Pollard. Reynolds number effects within the development region of a turbulent round free jet. *International Journal of Heat and Mass Transfer*, 52(17–18):3943–3954, 2009.

[27] Benoit Fond, Christopher Abram, and Frank Beyrau. Characterisation of the luminescence properties of bam:eu2+ particles as a tracer for thermographic particle image velocimetry. *Applied Physics B*, 121(4):495–509, 2015.

[28] Benoit Fond, Christopher Abram, and Frank Beyrau. On the characterisation of tracer particles for thermographic particle image velocimetry. *Applied Physics B*, 118(3):393–399, 2015.

[29] Benoit Fond, Christopher Abram, Andrew L. Heyes, Andreas M. Kempf, and Frank Beyrau. Simultaneous temperature, mixture fraction and velocity imaging in turbulent flows using thermographic phosphor tracer particles. *Optics express*, 20(20):22118–22133, 2012.

[30] N. Fuhrmann, E. Baum, J. Brübach, and A. Dreizler. High-speed phosphor thermometry. *Review of Scientific Instruments*, 82(10):104903, 2011.

[31] N. Fuhrmann, J. Brübach, and A. Dreizler. Phosphor thermometry: A comparison of the luminescence lifetime and the intensity ratio approach. *Proceedings of the Combustion Institute*, 34(2):3611–3618, 2013.

[32] William K. George. The self-preservation of turbulent flows and its relation to initial conditions and coherent structures. *Advances in turbulence*, pages 39–73, 1989.

[33] Joseph W. Goodman. *Introduction to Fourier optics*. McGraw-Hill physical and quantum electronics series. McGraw-Hill, San Francisco [u.a.], 1968.

[34] L. P. Goss, A. A. Smith, and M. E. Post. Surface thermometry by laser–induced fluorescence. *Review of Scientific Instruments*, 60(12):3702–3706, 1989.

[35] R. Hasegawa, I. Sakata, H. Yanagihara, B. Johansson, A. Omrane, and M. Aldén. Two-dimensional gas-phase temperature measurements using phosphor thermometry. *Applied Physics B*, 88(2):291–296, 2007.

[36] Ryo Hasegawa, Ichiro Sakata, Hiromichi Yanagihara, Gustaf Särner, Mattias Richter, Marcus Aldén, and Bengt Johansson. Two-dimensional temperature measurements in engine combustion using phosphor thermometry. In *JSAE/SAE International Fuels & Lubricants Meeting*, SAE Technical Paper Series. SAE International400 Commonwealth Drive, Warrendale, PA, United States, 2007.

[37] Eugene Hecht. *Optics*. Addison Wesley World Student Series Edition. Addison Wesley, Reading, 2. ed. edition, 1987.

[38] Syunji Imanaga, Shigeru Yokono, and Teruhiko Hoshina. Luminescence saturation effects in y2o2s: Eu phosphor. *Japanese Journal of Applied Physics*, 19(1):41–50, 1980.

[39] Frank P. Incropera and David P. DeWitt. *Fundamentals of heat and mass transfer*. Wiley, New York [u.a.], 2002.

[40] Hussein J. Hussein, Steven P. Capp, and William K. George. Velocity measurements in a high-reynolds-number, momentum-conserving, axisymmetric, turbulent jet. *Journal of Fluid Mechanics*, 258:31–75, 1994.

[41] J. Mi, D. S. Nobes, and G. J. Nathan. Influence of jet exit conditions on the passive scalar field of an axisymmetric free jet. *Journal of Fluid Mechanics*, 432:91–125, 2001.

[42] A. Jaber, L. Zigan, A. Sakhrieh, and A. Leipertz. Surface temperature measurements in a porous media burner using a new laser-induced phosphorescence intensity ratio technique. *Measurement Science and Technology*, 24(7):75202, 2013.

[43] C. Jainski, L. Lu, V. Sick, and A. Dreizler. Laser imaging investigation of transient heat transfer processes in turbulent nitrogen jets impinging on a heated wall. *International Journal of Heat and Mass Transfer*, 74:101–112, 2014.

[44] Jonathan Jordan and David A. Rothamer. Pr: Yag temperature imaging in gas-phase flows. *Applied Physics B*, 110(3):285–291, 2013.

[45] Gordana Jovicic, Lars Zigan, Stefan Will, and Alfred Leipertz. Phosphor thermometry in turbulent hot gas flows applying dy:yag and dy:er:yag particles. *Measurement Science and Technology*, 26(1):15204, 2015.

[46] L. K. Su and M. G. Mungal. Simultaneous measurements of scalar and velocity field evolution in turbulent crossflowing jets. *Journal of Fluid Mechanics*, 513:1–45, 2004.

[47] Indumathi Kamma, Praveena Kommidi, and B. Rami Reddy. High temperature measurement using luminescence of pr3+ doped yag and ho3+ doped caf2. *physica status solidi (c)*, 6(S1):S187–S190, 2009.

[48] G. Kemeny and C. H. Haake. Activator center in magnesium fluorogermanate phosphors. *The Journal of Chemical Physics*, 33(3):783–789, 1960.

[49] Y. Kim and S. Kang. Investigation of the degradation mechanisms in bamgal10o17:eu2+ phosphor: on the influence of thermal process on operational durability. *Appl. Phys. B*, 98(2-3):429–434, 2010.

[50] Christoph Knappe. *Phosphor Thermometry on Surfaces - A Study of its Methodology and its Practical Applications*. PhD thesis, Lund University, 2013.

[51] Wing Yin Kwong, Adam Steinberg, and Ya Huei Chin. Effect of bˆ3+-nˆ3- on yag:dy thermographic phosphor luminescence. *Optics Letters*, 39(21):6166–6169, 2014.

[52] Martin Lawrence, Hua Zhao, and Lionel Ganippa. Gas phase thermometry of hot turbulent jets using laser induced phosphorescence. *Optics express*, 21(10):12260–12281, 2013.

[53] F. Lemoine, Y. Antoine, M. Wolff, and M. Lebouche. Simultaneous temperature and 2d velocity measurements in a turbulent heated jet using combined laser-induced fluorescence and lda. *Experiments in Fluids*, 26(4):315–323, 1998.

[54] J. Lindén, N. Takada, B. Johansson, M. Richter, and M. Aldén. Investigation of potential laser-induced heating effects when using thermographic phosphors for gas-phase thermometry. *Applied Physics B*, 96(2-3):237–240, 2009.

[55] F. C. Lockwood and H. A. Moneib. Fluctuating temperature measurements in a heated round free jet. *Combustion Science and Technology*, 22(1-2):63–81, 1980.

[56] MathWorks. imregtform: http://de.mathworks.com/help/images/ref/imregtform.html.

[57] A. Melling. Tracer particles and seeding for particle image velocimetry. *Measurement Science and Technology*, 8(12):1406, 1997.

[58] Shigeo Mikoshiba, Shoji Shirai, Shinichi Shinada, and Masakazu Fukushima. Saturation of zn2sio4:mn luminescence under intense vuv excitation. *Journal of Applied Physics*, 50(2):1088–1090, 1979.

[59] Taeho Moon, Gun Young Hong, Hong-Cheol Lee, Eun-A Moon, Byung Woo Jeoung, Sun-Tae Hwang, Je Seok Kim, and Byung-Gil Ryu. Effects of eu2+ co-doping on vuv photoluminescence properties of bamgal10o17:mn2+ phosphors for plasma display panels. *Electrochemical and Solid-State Letters*, 12(7):J61–J63, 2009.

[60] T. Morel. Comprehensive design of axisymmetric wind tunnel contractions. *Journal of Fluids Engineering*, 97(2):225–233, 1975.

[61] Dieter Most, Friedrich Dinkelacker, and Alfred Leipertz. Direct determination of the turbulent flux by simultaneous application of filtered rayleigh scattering thermometry and particle image velocimetry. *Proceedings of the Combustion Institute*, 29(2):2669–2677, 2002.

[62] F. Abou Nada, C. Knappe, X. Xu, M. Richter, and M. Aldén. Development of an automatic routine for calibration of thermographic phosphors. *Measurement Science and Technology*, 25(2):25201, 2014.

[63] A. Nauert and A. Dreizler. Conditional velocity measurements by simultaneously applied laser doppler velocimetry and planar laser-induced fluorescence in a swirling natural gas/air flame. *Zeitschrift für Physikalische Chemie*, 219(5):635–648, 2005.

[64] Nicholas James Neal, Jonny Jordan, and David Rothamer. Simultaneous measurements of in-cylinder temperature and velocity distribution in a small-bore diesel engine using thermographic phosphors. *SAE International Journal of Engines*, 6(1):300–318, 2013.

[65] A. Omrane, P. Petersson, M. Aldén, and M. A. Linne. Simultaneous 2d flow velocity and gas temperature measurements using thermographic phosphors. *Applied Physics B*, 92(1):99–102, 2008.

[66] George Papadopoulos and William M. Pitts. Scaling the near-field centerline mixing behavior of axisymmetric turbulent jets. *AIAA Journal*, 36(9):1635–1642, 1998.

[67] Laurence Pietri, Muriel Amielh, and Fabien Anselmet. Simultaneous measurements of temperature and velocity fluctuations in a slightly heated jet combining a cold wire and laser doppler anemometry. *International Journal of Heat and Fluid Flow*, 21(1):22–36, 2000.

[68] W. M. Pitts. Effects of global density ratio on the centerline mixing behavior of axisymmetric turbulent jets. *Experiments in Fluids*, 11(2-3):125–134, 1991.

[69] Stephen B. Pope. *Turbulent flows.* Cambridge Univ. Press, Cambridge [u.a.], 2008.

[70] R. Chevray and N. K. Tutu. Intermittency and preferential transport of heat in a round jet. *Journal of Fluid Mechanics*, 88(01):133–160, 1978.

[71] N. R. Panchapakesan and J. L. Lumley. Turbulence measurements in axisymmetric jets of air and helium. part 1. air jet. *Journal of Fluid Mechanics*, 246:197–223, 1993.

[72] N. R. Panchapakesan and J. L. Lumley. Turbulence measurements in axisymmetric jets of air and helium. part 2. helium jet. *Journal of Fluid Mechanics*, 246:225–247, 1993.

[73] Markus Raffel, Christian E. Willert, and Jürgen Kompenhans. *Particle image velocimetry: A practical guide.* Springer, Berlin [u.a.], 1998.

[74] P. A. Rodnyi and I. V. Khodyuk. Optical and luminescence properties of zinc oxide (review): Optics and spectroscopy. *Opt. Spectrosc.*, 111(5):776–785, 2011.

[75] D. A. Rothamer and J. Jordan. Planar imaging thermometry in gaseous flows using upconversion excitation of thermographic phosphors. *Applied Physics B*, 106(2):435–444, 2012.

[76] S. Russ and P. J. Strykowski. Turbulent structure and entrainment in heated jets: The effect of initial conditions. *Physics of Fluids A: Fluid Dynamics (1989-1993)*, 5(12):3216–3225, 1993.

[77] Jun Sakakibara, Koichi Hishida, and Masanobu Maeda. Vortex structure and heat transfer in the stagnation region of an impinging plane jet (simultaneous measurements of velocity and temperature fields by digital particle image velocimetry and laser-induced fluorescence). *International Journal of Heat and Mass Transfer*, 40(13):3163–3176, 1997.

[78] Gustaf Särner, Mattias Richter, and Marcus Aldén. Investigations of blue emitting phosphors for thermometry. *Measurement Science and Technology*, 19(12):125304, 2008.

[79] H. Seyfried, G. Särner, A. Omrane, M. Richter, H. Schmidt, and M. Aldén. Optical diagnostics for characterization of a full-size fighter-jet afterburner. In *ASME Turbo Expo 2005: Power for Land, Sea, and Air.*

[80] S. J. Skinner, J. P. Feist, I.J.E. Brooks, S. Seefeldt, and A. L. Heyes. Yag:ysz composites as potential thermographic phosphors for high temperature sensor applications. *Sensors and Actuators B: Chemical*, 136(1):52–59, 2009.

[81] S. Someya, D. Ochi, Y. Li, K. Tominaga, K. Ishii, and K. Okamoto. Combined two-dimensional velocity and temperature measurements using a high-speed camera and luminescent particles. *Applied Physics B*, 99(1-2):325–332, 2010.

[82] Satoshi Someya, Yanrong Li, Keiko Ishii, and Koji Okamoto. Combined two-dimensional velocity and temperature measurements of natural convection using a high-speed camera and temperature-sensitive particles. *Experiments in Fluids*, 50(1):65–73, 2011.

[83] Satoshi Someya, Yasuhiro Okura, Mitsunori Uchida, Yoshihisa Sato, and Koji Okamoto. Combined velocity and temperature imaging of gas flow in an engine cylinder. *Optics letters*, 37(23):4964–4966, 2012.

[84] Stavros Tavoularis and Stanley Corrsin. Experiments in nearly homogenous turbulent shear flow with a uniform mean temperature gradient. part 1. *Journal of Fluid Mechanics*, 104:311–347, 1981.

[85] Noriyuki Takada, Ichiro Sakata, Hiromichi Yanagihara, Johannes Lindén, Mattias Richter, Marcus Aldén, and Bengt Johansson. Two-dimensional temperature measurements in diesel piston bowl using phosphor thermometry. In *9th International Conference on Engines and Vehicles*, SAE Technical Paper Series. SAE International400 Commonwealth Drive, Warrendale, PA, United States, 2009.

[86] Zu Puayen Tan, Eugene Lubarsky, Oleksandr Bibik, Dmitriy Shcherbik, and Ben T. Zinn. Application of planar laser-induced phosphorescence to investigate jet-a injection into a cross-flow of hot air. In *ASME Turbo Expo 2014: Turbine Technical Conference and Exposition*, page V006T06A005, 2014.

[87] Barry N. Taylor and Chris E. Kuyatt. Guidelines for evaluating and expressing the uncertainty of nist measurement results: Nist technical note 1297, 1994 edition.

[88] van Lipzig, J. P. J., M. Yu, N. J. Dam, C. C. M. Luijten, and de Goey, L. P. H. Gas-phase thermometry in a high-pressure cell using bamgal10o17: Eu as a thermographic phosphor. *Applied Physics B*, 111(3):469–481, 2013.

[89] VDI e. V., editor. *VDI Heat Atlas.* Springer Berlin Heidelberg, Berlin, Heidelberg, 2010.

[90] Fei Wang, Xiumin Chen, Dachun Liu, Bin Yang, and Yongnian Dai. Experimental and theoretical study of pure and doped crystals: Gd2o2s, gd2o2s:eu3+ and gd2o2s:tb3+. *Journal of Molecular Structure*, 1020:153–159, 2012.

[91] T. H. Weisgraber and D. Liepmann. Turbulent structure during transition to self-similarity in a round jet. *Experiments in Fluids*, 24(3):210–224, 1998.

[92] I. Wygnanski and H. Fiedler. Some measurements in the self-preserving jet. *Journal of Fluid Mechanics*, 38(03):577–612, 1969.

[93] Ping Yang, Guang-Qing Yao, and Jian-Hua Lin. Energy transfer and photoluminescence of bamgal10o17 co-doped with eu2+ and mn2+. *Optical Materials*, 26(3):327–331, 2004.

[94] William M. Yen, Shigeo Shionoya, and Hajime Yamamoto, editors. *Phosphor handbook*, volume 21 of *CRC Press laser and optical science and technology series*. CRC Press, Boca Raton, Fla., 2. ed. edition, 2007.

[95] Takeshi Yokomori, Haruko Nagai, Hiroshi Shiratori, Naoki Shino, Naoki Fujisawa, and Taro Hirasawa. Simultaneous measurements of phosphor thermometry and piv for high-temperature gas flows. In *JSAE/SAE 2015 International Powertrains, Fuels & Lubricants Meeting*, SAE Technical Paper Series. SAE International400 Commonwealth Drive, Warrendale, PA, United States, 2015.

[96] M. Yu, G. Särner, C. C. M. Luijten, M. Richter, M. Aldén, R. S. G. Baert, and de Goey, L P H. Survivability of thermographic phosphors (yag: Dy) in a combustion environment. *Measurement Science and Technology*, 21(3):37002, 2010.

# Curriculum Vitae

## Personal

- Name: Hyunchang Lee
- Date of birth: 3.5.1980
- Place of birth: Kwangju, Korea

## Education

- 3.1996 - 2.1999: Yushin High Scholl, Suwon, Korea
- 3.1999 - 2.2006: Sogang Univ., Seoul, Korea, BE in Mechanical Engineering
- 3.2006 - 8.2008: KAIST, Daejeon, Korea, MS in Aerospace Engineering
- 9.2012 - 6.2016: TU Darmstadt, Darmstadt, Germany, Dr.-Ing. in Mechanical Engineering